DEVELOPMENT AND CHARACTERISATION OF A HIGH PERFORMANCE DISTRIBUTED FEEDBACK FIBRE LASER HYDROPHONE

UNNIKRISHNAN KUTTAN CHANDRIKA

(B. Tech., NITC, India, M.S., University of Cincinnati, USA)

A THESIS SUBMITTED

FOR THE DEGREE OF DOCTOR OF PHILOSOPHY

DEPARTMENT OF MECHANICAL ENGINEERING

NATIONAL UNIVERSITY OF SINGAPORE

2014

DECLARATION

I hereby declare that this thesis is my original work and it has been written by me in its entirety. I have duly acknowledged all the sources of information which have been used in the thesis. This thesis has also not been submitted for any degree in any university previously.

Unnikrishnan Kuttan Chandrika

May 07, 2014

Acknowledgements

First of all, I would like to thank my supervisors Dr. Pallayil Venugopalan, A/Prof. Lim Kian Meng, and A/Prof. Chew Chye Heng for their esteemed guidance and encouragement throughout the research work. I would like to express my sincere gratitude towards Acoustic Research Laboratory (ARL) and DRTech Singapore for funding and supporting the research work.

It would not have been possible for me to progress in my research work without the assistance from research collaborators at I^2R, Singapore. I would like to thank Mr JunHong Ng, Dr. Yang Xiufeng, and Dr. Zihao Chen from I^2R for the fabrication of fibre lasers and assistance in setting up the measurement instrumentation.

I would like to thank Dr. Mandar Chitre, Head, ARL and Prof NG Kee Lin, Director, Tropical Marine Science Institute for their support and encouragement. I would also like to express my gratitude to all my friends and colleagues for their encouragements and support. Last but not the least, I thank my family without whose emotional support, it would not have been possible for me complete this work in time.

Table of Contents

Summary

Fibre laser based sensing technology is fast developing and may soon be a promising alternative to the conventional piezo-ceramic based sensors used in towed underwater acoustic arrays. The primary objective of this thesis is the development of a high performance fibre laser hydrophone with high and flat sensitivity up to 5 kHz for thin-line array application. The inherent advantages of fibre laser hydrophones are their intrinsic safety to water leakage, ease of multiplexing, high sensitivity to strain, remote sensing capabilities and immunity to electromagnetic interference.

A novel pressure compensated packaging scheme is proposed in this thesis. Major design considerations in the development of a fibre laser hydrophone for underwater surveillance applications along with a comprehensive design approach are presented. An analytical model for the metal diaphragm based sensing configuration is obtained through a four pole transfer matrix technique and validated using axisymmetric finite element analysis (FEA). Optimum values of the proposed sensor configuration were selected based on the simplified analytical model. Amplitude and phase responses from simplified model closely follows the predictions obtained form FEA simulations, deviating only at the fundamental resonance of the active sensing region. Prototype sensors were fabricated and testes. The experimental results were found to be in good agreement with the theoretical predictions.

The application of towed arrays for underwater surveillance to some extent is limited by flow noise. Equations for the flow noise levels inside the array tube were obtained by modelling the towed array as an infinite fluid filled tube submerged in water. Improved estimates of flow noise

levels for the actual array configuration were then obtained based on the finite element analysis of array sections. Although significant reduction in flow noise levels can be achieved through a fluid filled array configuration, the flow noise isolation decreases with increase in tow speed. The flow noise arising due to turbulent wall pressure fluctuations for the analysed configuration was found to be less than the usual ambient noise levels in the sea for operating speeds below 2 m/s.

Interferometric systems along with phase demodulators are usually employed in fibre laser based underwater acoustic sensing. Distortion free dynamic range of the sensor is mainly controlled by the demodulation techniques employed in signal reconstruction. Distortion performance of various widely used phase generated carrier (PGC) schemes were analysed in this thesis. It was observed that, in contrast to the reported analytical results, the distortions in practical implementation of PGC-arctangent scheme is frequency dependent due to spectral overlapping and errors in estimation of quadrature components of the phase change signal. PGC-optiphase algorithm, which uses feedback loop controls to keep the ideal operating parameters, was found to give better distortion performance over wide frequency and amplitude ranges.

The sensor was characterised for its temperature and acceleration sensitivity and the performance of the pressure compensation scheme was validated through hydrostatic testing in a pressure chamber. Temperature sensitivity measurements for the sensor indicate that variation in fibre laser wavelengths are not significant enough to cause any issues with wavelength division multiplexing schemes for normal operating temperatures in the sea. The sensor has an acceleration rejection figure of 0 dB ref $1 m/s^2 Pa$ which is comparable to the best values reported in the literature.

List of Tables

List of Figures

List of Symbols

δ	boundary layer thickness
$[T]$	four pole transfermatrix
$\check{A}$	amplitude
$\Delta\phi$	phase change at the interferometer output
η_P	pressure sensitivity
Γ	spatial correlation
$\hat{\alpha},\ \hat{\beta}$	contants of exponential decay
$\hat{\mathbf{k}}$	complex wavenumber
λ_L	wavelength of the fibre laser output
Λ_B	grating pitch
λ_B	Bragg wavelength
$\mathbb{D}$	optical path difference in the interferometer
$\mathbb{F}$	spectral excitation
$\mathbb{H}$	frequency response function
$\mathbb{n}_{eff}$	effective refractive index of the medium
$\mathbb{P}(\mathbf{k},\omega)$	frequency wavenumber spectra of the wall pressure fluctuations
$\mathbb{Q}$	flow noise response of the sensor
$\mathbb{S}_1,\ \mathbb{S}_2$	outputs of the lowpass filtering stage in PGC algorithm
$\mathbb{S}_{DCM},\ \mathbb{S}_{arctan}$	outputs of PGC-DM and PGC-artangent algorithms
$\mathbb{u}$	spectral displacement
$\mathbb{V}$	visibility of the interference signal
$\mathfrak{B}$	bulk modulus

$\mathfrak{H}(\mathbf{k}, \omega)$ frequency wavenumber response of the sensor packaging

μ dynamic viscosity

μ_f mass per unit length of the fibre laser

ν Poisson's ratio

ν_g Poisson's ratio of glass

ω angular frequency

ω_c carrier angular frequency

$\phi(t)$ phase change signal

ϕ_D, ϕ_R, ϕ_S phase delay, phase at reference arm of the interferometer, phase at the signal arm of the interferometer

ρ density

ρ_0 density of the acoustic medium

ρ_w density of water

σ flow resistivity

τ_ω wall shear stress

$\mathbf{k}$ wavenumber vector

ε strain

ξ_1, ξ_2 spatial separations along and normal to the flow direction

a radius

A, B DC and AC value of the optical intensity at the output of interferometer

b ratio of amplitudes of first and second Bessel harmonics of the carrier signal

C modulation depth

c speed of sound

C_{eq} equivalent damping coefficient

D signal amplitude

E Young's modulus

E_g Young's modulus of glass

F_L frequency of the fibre laser output

f_n natural frequency

$G,\ H$ amplitudes of the mixing signals in PGC algorithm

h thickness

H_n Hankel function of first kind of order n

$I,\ I_R,\ I_S$ light intensity, light intensity at reference arm, light intensity at sensor arm

J_n Bessel functions of first kind of order n

K stiffness

k wavenumber

k_λ wavenumber of light in vacuum

K_{eff} effective stiffness

L length of the optical path

L_E length of expansion chamber

L_f free length of fibre laser

M mass

MS modulation signal

p sound pressure

$P,\ \Delta P$ pressure, pressure change

$P_0(k_z, \omega)$ axisymmetric wall pressure spectra

P_i Pressure amplitude of the incident wave

P_r Pressure amplitude of the reflected wave

P_t Pressure amplitude of the transmitted wave

$p_{11},\ p_{12}$ elasto optic coefficients

Q volume velocity

R radiation loss

R_T time scale ratio

S cross section area

T temperature

T_π power transmission coefficient

T_{pre} applied tension

THD total harmonic distortion

U free stream velociy

u velocity along x direction

U_c convection velocity

u_c velocity at centre of the diaphragm

$v_*,\ u_*$ friction velocity

Φ auto-spectrum of the wall pressure fluctuations

$\varepsilon_r,\ \varepsilon_z,\ \varepsilon_\phi$ strain components along directions $r,\ z$ and ϕ in cylindrical coordinate system

AUV autonomous underwater vehicle

DCM differentiation and cross multiplication

DFB distributed feedback

DWDM dense wavelength division multiplexing

FL fibre laser

PGC phase generated carrier

SNR signal to noise ratio

TBL turbulent boundary layer

USV unmanned surface vessel

WDM wavelength division multiplexing

Chapter 1

Introduction

Underwater operations like oil explorations, anti-submarine warfare, and coastal monitoring often employ long arrays of acoustic sensors that run into many hundreds of meters. At present, most of these applications use piezo-ceramic based hydrophones, which generate electrical signals corresponding to the pressure variations caused by the sound waves in the water. Conventional arrays based on ceramic sensors are usually bulky and demand special handling gears for their operation and thus not suitable for autonomous underwater vehicle (AUV) or unmanned surface vessel (USV) based applications. In the recent years, as AUV and USV technologies have matured, there has been an increased demand for development of light weight thin-line sensor arrays[1] for underwater surveillance applications using AUVs and USVs. The demand for a thin-line array is also fuelled by the fact that these sensor arrays can be easily deployed from any platform of opportunity thus resulting in substantial savings in terms of expensive ship time.

Most of the recent efforts in light weight array development is directed towards piezo-ceramic based arrays [1–3]. The endurance of these hy-

[1] in this thesis thin-line array refers to towed arrays with outer diameter less than or equal to 20mm

drophone arrays are often constrained by the onboard power supply limitations and a few engineering problems such as need to route multiple electrical lines through available space in the array tube. In addition, piezo-ceramic sensors require associated electronics for multiplexing and data transmission, etc., to be kept inside the array, thus increasing the reliability risks associated with water ingress. Fibre optic sensing with its distinguishing features like ease of multiplexing, high sensitivity, immunity to electromagnetic interference, intrinsic safety to water leakage, and remote measurement capability provides an ideal technological platform for underwater acoustic sensing.

For the last three decades, extensive research has been carried out towards the development of fibre optic hydrophones [4]. Initial developments were towards the application of intensity-based schemes, in which external excitations produce corresponding changes in the intensity of the light carried over the fibre [5]. Later on, coherent detection schemes, which used long coils of fibres on compliant mandrels as hydrophones gained momentum due to its performance merits. But the high Young's modulus value of silica fibre necessitated new techniques to enhance the strains on the fibre under the action of acoustic waves. Thus, early works on the fibre optic hydrophones focused on achieving the required sensitivity values by coiling hundreds of meters of fibres on compliant mandrels or through the application of compliant coatings. Sensor arrays constructed using these hydrophones tend to be bulky as the sensor size is often controlled by the allowable bending radius of the fibre. Moreover, multiplexing of these sensors required the use of large number of fibre couplers in the wet-end of the sensor array. With the advent of Bragg gratings and fibre lasers with very high strain sensitivity, now the focus is towards the development of fibre optic hydrophone based on fibre lasers.

1.1 Motivation

Fibre laser sensing offers an attractive technology for the development of light weight acoustic sensor arrays due to their thin-line nature, high sensitivity to the strain, intrinsic safety to water leakage and multiplexing capabilities. The working of fibre laser hydrophones is based on the principle that pressure changes in acoustic wave will introduce corresponding changes in the wavelength of the fibre laser output. Interferometric systems along with phase demodulators are usually employed to convert the fibre laser wavelength changes into electrical signals. Even though the fibre laser wavelength is highly sensitive to strain, the high elastic modulus of glass fibre necessitates additional compliant mechanical packaging to achieve required sensitivity values in the operating bandwidth. Though there has been many attempts in the past to achieve sensitivity improvements, many of these sensors suffer from reduced operational bandwidth. In addition, sensitivity improvements are often associated with excessive response with static pressure which limits the safe operating depths of these sensors.

Unlike conventional ceramic hydrophones, fibre laser hydrophone's performance depends on the parameters of interferometer and demodulation techniques employed. Hence an holistic approach is required in the development of the fibre laser hydrophone. It is highly desirable to have a theoretical model for the performance prediction of fibre laser hydrophone as there are many parameters that need to be optimised to achieve desired performance characteristics. Flow noise is another important aspect that needs to be addressed in the application of these fibre laser hydrophones when used as towed arrays. Though there were a few attempts in the past to estimate flow induced noise for ceramic based hydrophone based towed arrays, to the best of author's knowledge, there are no published reports

in open literature on flow noise in fibre laser towed arrays. Thus this thesis attempts to address the above knowledge gaps and contribute to the existing knowledge base in the fibre laser acoustic sensing through the development and characterisation of a miniature pressure compensated fibre laser hydrophone.

1.2 Objectives

The primary objective of this work is to develop and characterise a miniature static pressure compensated fibre laser hydrophone with improved frequency response characteristics. The thesis aims to identify, model, and optimise key parameters of sensor packaging, interferometer and phase demodulation techniques and associated signal processing to realise a fibre laser hydrophone for thin-line towed arrays suitable for underwater surveillance and survey applications in littoral waters. The sensor configuration will be capable of achieving sea state zero noise floor with high and flat sensitivity up-to 5 kHz and operational depths of the order of 50 m. Though there are many attempts on development of mechanical packaging to improve the performance of fibre laser hydrophones, an integrated approach that addresses the sensitivity, wide bandwidth, noise floor, pressure compensation and related theoretical frame work is not available in open literature. This thesis aims to bridge this knowledge gap through the development of an integrated theoretical model for pressure compensated miniature diaphragm based fibre laser hydrophones that incorporate the fluid structure interaction effects, and viscous and frictional losses. The thesis also aims to validate the theoretical model through finite element analysis and experiments.

Coherent sensing schemes, as in fibre laser hydrophones, usually employ

phase generated carrier (PGC) schemes to address signal fading and signal distortions in interferometer based sensing. One of the major limitations in these algorithms is the signal distortions at the interferometer output. The distortion figure of demodulation technique has a direct impact on achievable distortion free dynamic range of the sensor. This thesis explores the origins of this signal distortion and performs a comparative study on the distortion performance of different PGC techniques.

Flow noise experienced under normal operating speeds is an important design consideration in towed arrays development, specifically in thin-line arrays. This thesis aims to estimate the flow noise levels in a fluid filled fibre laser hydrophones array though a finite element analysis based calculation procedure. It also aims to arrive at a simplified analytical model of fluid filled towed arrays for flow noise predictions.

Field application of fibre laser hydrophone demands good acceleration rejection characteristics to minimise the effect of platform vibrations and flow induced vibrations. Hydrostatic pressure and temperature variations experienced during normal operations might affect the performance of the sensor. Susceptibility of the sensor performance to these environmental conditions will also be explored in this thesis.

1.3 Outline

This thesis is organised into six main chapters. Chapter 2 presents the literature review related to fibre optic hydrophones and introduces the basic sensing principle and associated technologies. Chapter 3 presents the major design challenges and considerations in the development of a fibre laser hydrophone. A diaphragm based pressure compensated fibre laser hydrophone configuration is proposed in this chapter to achieve the per-

formance objectives. An analytical model for performance prediction and optimisation is presented along with its validation through finite element analysis.

Chapter 4 presents the study on signal distortion in fibre laser based hydrophones due to spectral overlapping in phase generated carrier schemes. Distortion performance of major PGC schemes arising from errors in estimation of quadrature components at the lowpass filtering stage for an ideal filter was obtained analytically using Bessel expansion of the signal. The performance of the algorithms were then compared in the context of a fibre laser based hydrophone array.

Chapter 5 presents flow noise analysis for a fluid filled fibre laser based thin-line towed arrays. An analytical estimate of the expected flow noise levels was arrived at using an infinite fluid filled and submerged tube model. The results were then compared against finite element analysis results for the actual sensor array configuration. Chapter 6 presents the experimental validation of the acoustic sensitivity characteristics, pressure compensation performance and acceleration sensitivity characteristics of the fibre laser hydrophone developed in the thesis. Thesis concludes with summary of findings in this study and suggestions for future work.

1.4 Key Contributions

This section lists the original contributions in this thesis.

- Developed a novel pressure compensated fibre laser hydrophone capable of achieving sea state zero noise floor, high and flat sensitivity, and large bandwidth (0-5 kHz). Identified key design parameters that control the performance of a fibre laser hydrophone and presented a holistic design approach towards the development of a high perfor-

mance fibre laser hydrophone. This thesis presents and validates an analytical model of the diaphragm based pressure compensated fibre laser hydrophone.

- Insights into the harmonic distortions in phase generated carrier schemes due to the errors in estimation of quadrature components of the phase difference at interferometer output. The performance of different PGC demodulation schemes were compared to characterise the harmonic distortion arising due to non-ideal reproduction of the quadrature components at the output of low pass filtering in PGC schemes.

- Developed a simplified analytical model that includes the fluid loading effects for the prediction of flow noise levels in a fluid filled towed array. A finite element based analysis procedure for the calculation of flow noise response of a diaphragm based fibre laser hydrophone packaged inside a fluid filled cylinder was presented. The flow noise level experienced by a thin-line fibre laser hydrophone towed array under normal operating conditions was also estimated.

- The fibre laser hydrophone described in thesis is characterised for its acoustic sensitivity, safe operating depth and its sensitivity towards acceleration and temperature variations.

Chapter 2

Literature Review

Parameters like phase, intensity, and polarisation of the light travelling in an optical fibre is sensitive to external excitations. Thus, through careful design and selection of transduction parameters, external excitations like pressure, temperature, displacement, velocity, acceleration, chemicals could be measured using fibre optic sensing technology [6–10]. Significant progress has been made over the last three decades in the area of fibre optic sensing of underwater sound. Based on the light parameter used for sensing, fibre optic sensing applications can be broadly classified in to two categories viz. 1) amplitude or intensity based detection and 2) coherent detection or phase based methods. Intensity based sensing applications mostly rely on increase in light attenuation due to bending of the fibres [11, 12]. Even though the intensity-based methods have limited dynamic range and their performance are often affected by the factors associated with laser source, interconnecting links, and coating materials, they still find wide applications in industrial use and damage monitoring applications where cost is a major deciding factor [5]. High performance applications like underwater acoustic sensing demand a combination of high sensitivity, wide bandwidth and large dynamic range. Hence coherent detections schemes are widely

used in high performance sensing applications due to their merits in terms of fine measurement resolution and large dynamic range [4].

Phase-based schemes, known as coherent detection schemes, are based on the principle that the external excitation like strain or temperature can introduce proportional change in length and refractive index of the fibre. These changes in physical parameters of the fibre will result in corresponding changes in the phase of the light travelling in the fibre. Phase delay caused by an optical path length of L meter in a medium of refractive index $\mathbb{n}_{eft}$ is given by equation (2.1). In equation (2.1), k_λ is the wavenumber. Interferometers utilise this property to convert the phase changes into intensity variation through coherent mixing of light travelling in the two different arms of the interferometer. Schematic representations of two of the most commonly used interferometers viz. Mach-Zehnder interferometer (MZI) and Michelson interferometer are shown in figure 2.1 [13, 14]. In a Mach-Zehnder interferometer, the light from a stable laser source is divided into sensor arm denoted by subscript S and reference arm denoted by subscript R. In most of the applications, only sensing arm is exposed to external excitations and reference arm is usually isolated from external disturbances. Excitation like strain or temperature variation in the sensing arm introduces corresponding change in the phase of the light passing through the sensing arm. Light travelling in the arms are then recombined before passing it on to the photo detector for detection. The intensity at the detector is given by equation (2.2) . ϕ_R and ϕ_S are the phases of light and I_R and I_S are the intensities of the light in reference and sensing arms, respectively .The operating principle of the Michelson interferometer is similar to that of MZI, but as the light passes through the arms twice, the phase change introduced also will be doubled.

Polarisation fading, arising due to random changes in polarisation states

of the light due to changes in the fibre birefringence, can lead to reduction in interference efficiency and is a major concern in high performance sensing applications [15]. Michelson interferometers with Faraday rotator mirrors or polarisation maintaining fibres are often used to address the issue of polarisation fading [16].

$$\phi_D = \mathbb{n}_{eff} k_\lambda L \tag{2.1}$$

$$I = I_0 \left[1 + \mathbb{V} \cos(\Delta\phi)\right] \tag{2.2a}$$

where

$$I_0 = I_R + I_S, \ \mathbb{V} = \frac{2\sqrt{I_R I_S}}{(I_R + I_S)}, \ \Delta\phi = \phi_R - \phi_S \tag{2.2b}$$

Fibre optic sensing of underwater acoustic sound was experimentally demonstrated by a team from Naval Research Laboratory, USA [17]. The pressure variations in sound act on the sensing arm to create intensity variations in the interferometer output corresponding to the phase changes produced in the sensing arm. The responsivity of the fibre defined as the fractional phase change $\Delta\phi$ due to a pressure change ΔP is given as [18]

$$\frac{\Delta\phi}{\phi \Delta P} = \frac{1}{\Delta P} \left([\varepsilon_r \left(p_{11} + p_{12}\right) + \varepsilon_z p_{12}] \right), \tag{2.3}$$

where ε_r and ε_z are radial and axial components of strain and p_{ij} are the elasto-optic coefficients. As the Young's modulus of the silica fibre is very high, the responsivity of the fibre is very low and initial designs used hundreds of meters of fibre windings to achieve required sensitivity

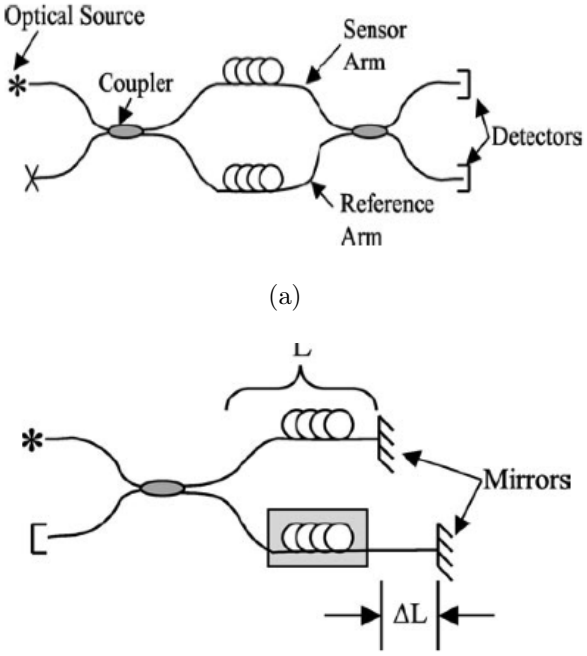

Figure 2.1: (a)Mach-Zehnder Interferometer (b) Michelson Interferometer [4]

values. For the subsequent designs, the focus was on strain sensitivity enhancements through coatings and coiling long fibres on compliant mandrels [19–22]. Some researchers managed to get substantial sensitivity improvements with the use of the air backed mandrel designs to achieve sea state 0 measurement resolutions [14, 23]. Safe operating depths of these sensors were limited due to the absence of static pressure compensation arrangements. Another limiting parameter was the frequency band of operation for the sensors. In another work, researchers explored a diaphragm based acoustic sensor in which fibre is bonded to a polymer diaphragm in zig-zag manner [24] and satisfactory application of these techniques for underwater acoustic surveillance demands further sensitivity improvements. Though mandrel wound sensor designs are actively pursued for thin line array applications [25], with the advent of Bragg gratings and Fibre lasers the focus has now shifted towards development of hydrophones using these

technologies [26–29].

2.1 Fibre Bragg grating and fibre lasers

Fibre Bragg grating (FBG) is produced by creating a periodic perturbation of refractive index along the fibre length as shown in figure 2.2. The first FBG was demonstrated by Hill et. al. in 1978 [30]. When illuminated by a broadband light source, FBG will selectively reflect a wavelength known as Bragg wavelength given by equation (2.4) where $\mathbb{n}_{eff}$ is the effective refractive index of the fibre and Λ_B is the grating pitch. Fibre Bragg gratings can be employed for sensing applications as any change in effective refractive index or grating pitch caused by pressure, temperature, strain etc. can be measured by observing the shift in wavelength of the light reflected from the FBG using a spectrum analyser or an interferometer.

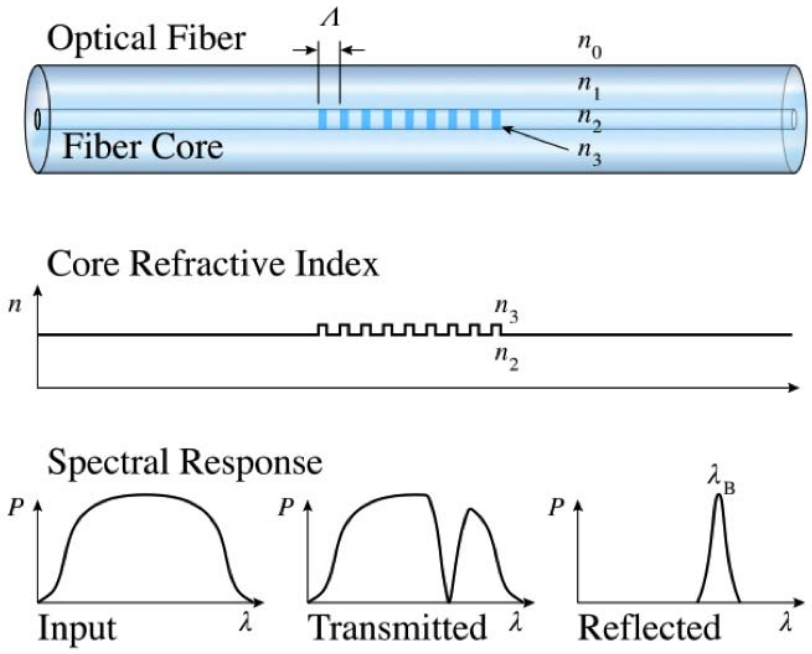

Figure 2.2: Refractive index variation is a fibre Bragg grating and its spectral response [31]

$$\lambda_B = 2\mathrm{n}_{eff}\Lambda_B \tag{2.4}$$

Periodic variation in the refractive index of the fibre required to create a fibre Bragg grating can be formed on a fibre by exposing it to an intense optical interference pattern [32]. Transverse holographic side illumination technique, which provides a cost effective method to produce fibre Bragg gratings, involves application of an ultraviolet fringe pattern onto photo-sensitive fibre to alter the fibre core's refractive index [33]. The ultraviolet fringe patterns are often created from the interference of two ultraviolet light beams or from a diffraction pattern produced using phase mask. The photo sensitivity of the fibre to ultraviolet light can be improved through hydrogen loading to enhance the efficiency of the process [34]. Though Bragg gratings on passive fibres can be used for hydrophone construction, fibre lasers offer a better solution for hydrophone construction as it is capable of much narrower light bandwidths.

A laser cavity can be formed in a fibre by writing spectrally matched FBG on either side of a rare earth element doped fibre. When pumped with external light source, fibre lasers generate a very narrow band laser at a wavelength that depends on parameters, like grating pitch, refractive index of the fibre and emission bandwidth of the dopant, etc. Erbium doped fibres (EDF) are the most commonly used in fibre lasers with an operating band width of 40nm centred around 1550nm. This wavelength region has a specific advantage as it corresponds to a region of lowest attenuation in silica fibre. Two most common approaches in achieving the fibre lasers are distributed Bragg reflector (DBR) and distributed feedback (DFB) [32,35].

2.1.1 Distributed Bragg reflector fibre laser(DBR-FL)

Figure 2.3 shows the configuration of a DBR laser where spectrally matched gratings are placed on either sides of an erbium-doped cavity. It forms a Fabry-Perot laser cavity whose lasing wavelength is determined by the grating pitch, lasing cavity length and emission bandwidth of the dopant [36]. Though the emission spectra of the erbium element is broad, due to the spectral characteristics of the Bragg grating, the resonance can occur only at frequencies at which the optical field match with the grating pitch of the FBG. As it can be seen in figure 2.4, the resonance cavity creates multiple resonant modes and the laser mode that matches the reflection band of the Bragg grating will result in a narrow line width laser generation. Narrow bandwidth laser can be generated by careful selection of Bragg grating pitch and the cavity length. Resonance modes that can fall in reflection band of the fibre Bragg grating increases with cavity length and can lead to a phenomenon called mode hopping.

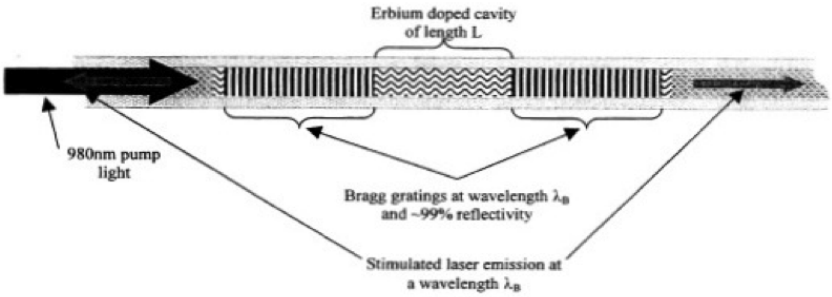

Figure 2.3: DBR fibre laser schematic [36]

2.1.2 Distributed feedback fibre laser (DFB-FL)

In DFB laser, shown in figure 2.5, Fabry-Perot laser cavity is formed by a π-shift in the Bragg grating. This creates a resonance cavity, which has a cavity length of $\lambda_B/4$ (by a phase shift of π in the grating pitch). This small

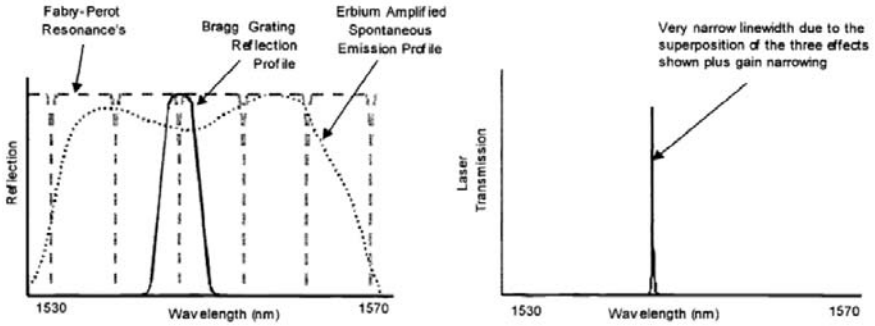

Figure 2.4: Operating principle of a DBR fibre laser [36]

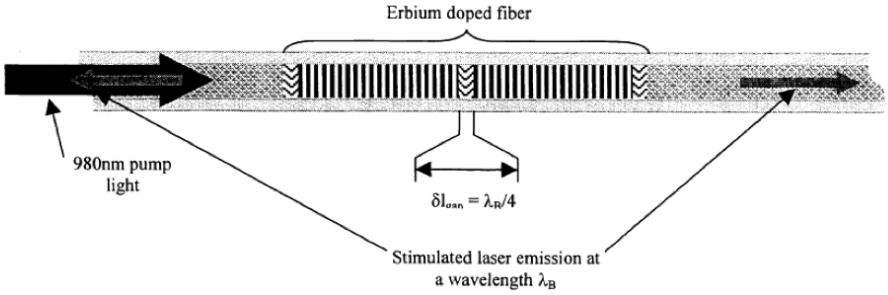

Figure 2.5: DFB fibre laser schematic [36]

cavity length limits the possible number of resonant modes and thus DFB lasers can achieve single mode operation at the fundamental resonance mode. This construction enables the DFB-FL to generate very narrow bandwidth laser at frequency centred at the stop band of Bragg grating as shown in Figure 2.6. DFB-FL was first demonstrated in 1994 [37] in a study where the necessary phase shift in the Bragg grating was created by localised heating. DFB-FLs offer very high stability of lasing mode owing to the very narrow lasing cavity, which eliminates the issue of mode hopping usually observed in the DBR-FLs. Due to this relative performance merit DFB-FLs are employed in the current study to develop high performance fibre optic hydrophones. However, the principles presented in this paper is very well applicable to hydrophones constructed using DBR-FLs.

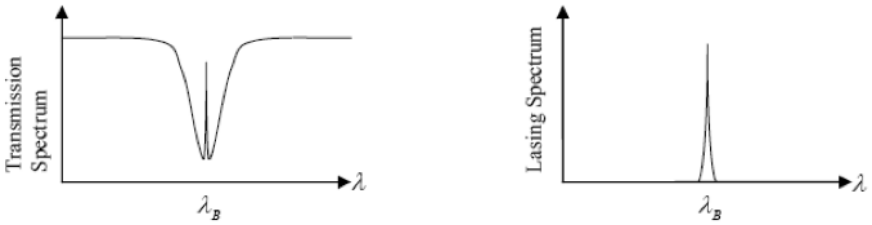

Figure 2.6: Operating principle of a DFB fibre laser [36]

2.1.3 Interferometer

Wavelength change in the reflected light from a Bragg grating or the laser output from a fibre laser can be converted to measurable phase change through the application of an interferometer. Interferometer used in a fibre optic hydrophone based on fibre lasers differs from the configuration shown in figure2.1 and a commonly employed configuration is shown in figure 2.7. In this configuration the laser output from the fibre laser is divided into two arms at the first coupler and then recombined at the second coupler before passing them into the photo detector. The phase difference introduced due to the length difference between the two arms of the interferometer, designated as optical path difference d, is given by equation (2.1). Unlike the mandrel wound fibre optic hydrophones, both the arms of the interferometer are isolated from external excitations.

As it is clear from the previous discussions and equation (2.2), actual measured signal manifests in the output of the photo detector in the form of $\cos(\Delta\phi)$, where $\Delta\phi$ is directly proportional to the external signal acting on the fibre. The dependence on cosine function restricts the operating ranges in which a linear relation can be obtained between the output of the interferometer and measured signal. Even though a linear operation with limited dynamic range can be achieved for very small amplitudes of $\Delta\phi$ around $\pi/2$, slow drifts in the wavelengths due to environmental

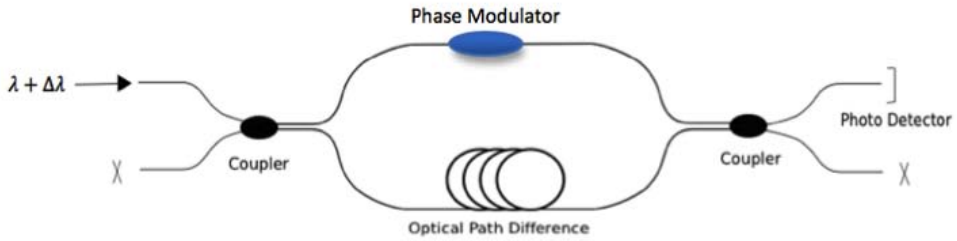

Figure 2.7: Sample configuration of an interferometer for a fibre laser hydrophone

parameters like temperature changes affects its operational stability. In order to overcome this limitation, phase modulators are usually employed to introduce a known carrier signal on the interferometer output. Piezoceramic based fibre stretchers are often used in interferometers as phase modulators [14]. Different demodulation techniques like phase generated carrier-differentiation and cross-multiplication (PGC-DCM), phase generated carrier- arctangent (PGC-arctan), etc., can then be employed to retrieve the signal information from the output of the interferometer. Detailed review and discussions on these techniques is presented in Chapeter 3.

A common configuration of fibre laser based sensing is shown in figure 2.8. A 980nm pump source is used to provide light energy to the fibre laser. The fibre laser absorbs this energy and emits a wavelength in 1550 nm range corresponding to the grating configuration of the fibre laser as explained in the previous section. A wavelength division multiplexer (WDM) is usually employed and it helps to couple 980nm to the fibre and separate out the 1550nm coming from the fibre laser. The output from the fibre laser is passed though an unbalanced interferometer. The phase demodulator generates a carrier signal and drives the fibre stretcher in the interferometer to introduce the carrier signal into the interferometer output. The output from the interferometer is then passed into the phase

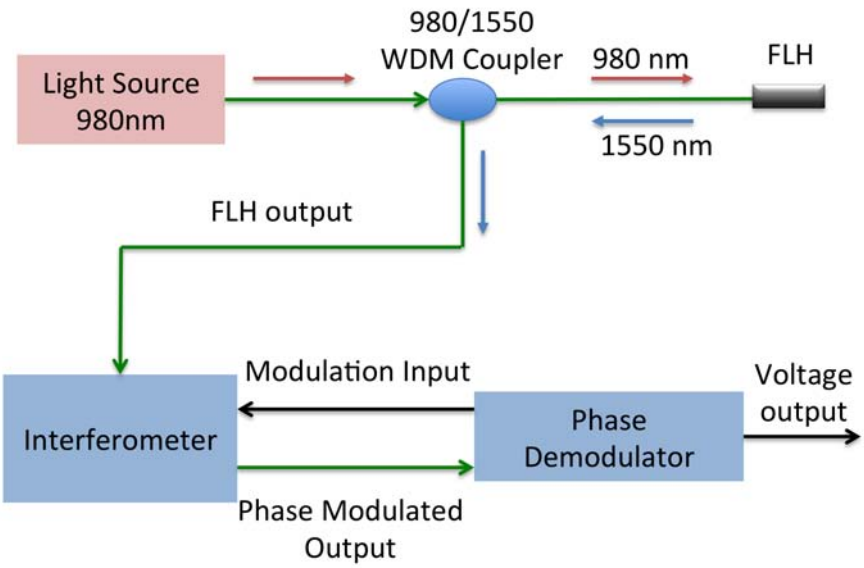

Figure 2.8: Typical measurement configuration used in fibre laser sensing

demodulator, which recovers the signal information from the interferometer output.

2.2 Fibre laser hydrophone

The wavelength of the laser generated by the fibre laser is extremely sensitive to strain [38]. This high sensitivity to strain along with its suitability for multiplexing make it a suitable candidate for underwater acoustic sensing. Koo and Kersy [39] demonstrated the feasibility of fibre laser in dynamic strain measurement applications and showed that the sensor performance is limited by the fibre laser thermal noise. In 1999, Hill et al. [35] demonstrated the application of fibre lasers for underwater acoustic measurements. Fibre optic hydrophones based on DFB and DBR fibre lasers were explored in their study. Experimental measurements showed significant sensitivity variation across the frequency range of operation due to

the presence of mechanical resonances. The authors also made attempts to improve on the sensitivity by flexible coatings. Though theoretical model predicted significant sensitivity improvements of the order of 30 dB, coated fibre lasers did not give predicted sensitivity improvements.

Cusano et al. [40] explored the effects of plastic coating shapes on the sensitivity performance of Bragg grating based sensors and observed the sensitivity values dropping at a much faster rate with frequency for spherical coatings compared to cylindrical coatings. Sun et. al. [41] reported experimental results from a polyurethane coated fibre laser hydrophones array and their results showed notable improvement in sensitivity over bare fibres. Polymer based compliant coating has to go through a curing process before it settle and this often resulted in uneven strains on the sensor grating structure. As the curing process progresses the wavelength tends to shift from its designed value before settling into a new final value at the completion of the curing process [42]. It has also been observed that the strains developed during curing process sometimes results in the damage of the grating structure and thereby destroying the sensor itself [35]. Hansen and Kullander [43] proposed a piston based configuration with soft material packing to improve up on the sensitivity values of fibre laser hydrophones. Even though the model predicts significant sensitivity improvements, the operational bandwidth of the proposed sensor is also limited by the low natural frequency of the system. In addition, safe operating depth of the sensor system is limited owing to the absence of any pressure compensation system.Bangoli et al. reported the application of acrylic coated fibre laser as hydrophones from high energy particle detection in deep waters [44]. They reported a lower than expected sensitivity which is in agreement with the results presented by Hill et al. in 1999 [35]. Zhang et al. presented a spindle based packaging for sensitivity improvements, but the sensor response has

a huge variation of the order of 40 dB arising due to the resonant modes in the frequency range of interest [45]. The above sensors were also susceptible to other non-acoustic excitations like acceleration. In order to overcome the acceleration sensitivity issues associated with the previous designs, Foster et al. [27] presented a fibre laser hydrophone configuration, which works in bending mode and has an operational bandwidth 0-2.5kHz. Goodman et al. [46] incorporated external air bladder for pressure compensation to the bending mode DFB-FL hydrophone to achieve safe operating depths of the order of 50m. Leung [47] presented a hydrophone based on composite cavity fibre laser, in which an additional laser cavity of shorter length is created on the same active element beside the main cavity. A non-uniform straining scheme in which shorter cavity is isolated from external excitation is proposed to improve the sensitivity of the fibre laser hydrophone. A fibre laser hydrophone system for measurements below 1kHz, which measures the sound through the measurement of change in beat frequency generated by two polarisation lines generated by fibre laser, was presented by Tan et al. [48]. A recent paper by Foster et al. [49] reports another fibre laser hydrophone with good acceleration rejection and enhanced frequency range of operation, though not pressure compensated. There are also many research efforts towards the development of fibre laser vector sensor in which the sensor responds to particle velocities rather than pressure. Ma et al. presented a fibre laser vector hydrophone based on v-shaped beams and reported a resonant frequency of 310Hz [50]. Currently these type of sensors have limited frequency range and are only suitable for low frequency applications [51–53].

One of the major design concepts gaining momentum in the recent years is diaphragm-based design of fibre laser hydrophones [24, 54]. Zhang et al [55, 56] presented a double diaphragm based hydrophone design and

explored the effects of diaphragm material properties on hydrophone performance. The design performance was limited by the presence of mechanical resonance of the diaphragm. In addition, the operational depths are limited due to the presence of watertight air cavities in the design.

2.3 Summary

The field of fibre laser based sensing of underwater acoustic sound is fast developing and may soon become a viable alternative to conventional piezo-ceramic based acoustic arrays. This chapter introduced the basic concepts and presented a review of the associated technologies in the field of fibre laser based sensing of underwater sound. Though there has been many attempts in the past towards the development of fibre laser packaging for high performance hydrophone applications, an integrated approach to the design of encapsulation that addresses the sensitivity, pressure compensation and wide bandwidth of operation and related theoretical framework is not available in open literature. The following chapters in this thesis address this issue through the development, analysis and testing of diaphragm based pressure compensated fibre laser hydrophone system. The review presented in this chapter provides an adequate background knowledge to appreciate the work presented in upcoming chapters.

Chapter 3

Pressure Compensated Fibre Laser Hydrophone

3.1 Introduction

The fibre laser hydrophone (FLH) technology has been fast developing and it may soon be an alternative to the existing mandrel wound fibre optic hydrophones due to their high sensitivity, ease of multiplexing and compact size. Although the wavelength of fibre laser output is highly sensitive to strains, high elastic modulus of the glass fibre necessitates methods to enhance the pressure sensitivity of the fibre laser. This chapter presents a miniature pressure compensated metal diaphragm based fibre laser hydrophone capable of measuring acoustic signals as small as sea state zero noise levels and a flat frequency response in the frequency range 10Hz-5kHz.

The chapter is organised into three main sections. In section 3.2, an overview of the design considerations of a fibre laser hydrophone in conjunction with the most widely used detection methodology is presented. The proposed design approach for the new FLH is described in section 3.3. A theoretical framework developed for the FLH encapsulation and its val-

idation through finite element analysis (FEA) is described in section 3.4, followed by a summary of findings in section 3.5.

3.2 Design considerations

The way fibre laser hydrophones work is based on the principle that the strains induced by the pressure changes due to an acoustic wave will introduce corresponding change in the wavelength of the laser generated by the fibre laser. Interferometeric systems are usually employed to convert the wavelength shifts in the fibre laser output into light intensity variations, which can then be converted to electrical signals using photodetectors [35]. The design parameters of FLH system considered in the current study are its sensitivity, frequency response, measurement resolution, dynamic range and signal distortion[1]. The performance objectives are summarised in table 3.1.[2]

Table 3.1: Summary of performance objectives

Feature	Value
Overall Diameter	$<$ 20mm
Overall Length	$<$ 80mm
Mechanical Sensitivity	$> 2 \times 10^{-9}$strain/Pa
Fundamental resonance	$>$ 7kHz
Distortion ratio	better than -60dB
Dynamic range	$>$ 100dB

The phase resolution and noise floor characteristics of the fibre laser hydrophone system depend directly on three major parameters: the measurement resolution of the opto-electronic instrumentation, the inherent frequency noise of the fibre laser and the optical path imbalance used in the

[1] represented using distortion ratio which is defined as the ratio of energy at signal harmonics and other spurious signals to the energy at the signal frequency

[2] arrived at based on a US Navy report on fibre optic hydrophone [57] and thin-line array operational requirements

interferometer. Commercial phase demodulation systems that can achieve measurement resolutions of the order of a few micro radians are available off the shelf. Thus for a fibre laser sensor with sufficient phase sensitivity to generate phase changes greater than the measurement resolution of the opto-electronic instrumentation, the noise floor is primarily dictated by the inherent noise from the fibre laser. The phase sensitivity of fibre laser hydrophone can be defined as the phase change produced per unit pressure and can be expressed as [4]

$$\frac{\partial(\Delta\phi)}{\partial P} = \mathbb{n}_{eff} k_\lambda \mathbb{D} \eta_P \tag{3.1a}$$

where

$$\eta_P = -\frac{1}{P}\frac{d\lambda_L}{\lambda_L} = \frac{1}{P}\frac{dF_L}{F_L}. \tag{3.1b}$$

In equation (3.1), $\mathbb{n}_{eff}$ is the refractive index, k_λ is the wavenumber and η_P is the pressure sensitivity of the active sensing region, $\mathbb{D}$ is the optical path imbalance in the interferometer and P is the pressure that produces a corresponding wavelength change of $d\lambda_L$ in the fibre laser wavelength λ_L (or frequency change dF_L in the fibre laser frequency F_L). The wavelength of the light emitted from the fibre laser depends on parameters like grating pitch, refractive index of the fibre, cavity length and emission spectra of the dopant. Differentiating equation (2.4), we arrive at a relationship between laser wavelength change and external excitation as given in equation (3.2) [32, 58]. The relation between applied strain and wavelength can be expressed as in equation (3.3), where elasto-optic coefficients p_{ij} are used to account for variation in refractive index to the applied strain [18, 35]. In

equation (3.3), ε_r and ε_z are the radial and axial strain respectively.

$$\frac{d\lambda_L}{\lambda_L} = \frac{d\Lambda_B}{\Lambda_B} + \frac{d\mathrm{n}_{eff}}{\mathrm{n}_{eff}} \tag{3.2}$$

$$\frac{d\lambda_L}{\lambda_L} = \varepsilon_z - \frac{\mathrm{n}_{eff}^2}{2}\left[(p_{11}+p_{12})\,\varepsilon_r + p_{12}\varepsilon_z\right] \tag{3.3}$$

When the wavelength of the acoustic wave is much larger than the active sensing region, it can be assumed that uniform pressure acts all along the sensor. The wavelength shift under the action of uniform pressure can be written as in equation (3.4).

$$\frac{d\lambda_L}{\lambda_L} = \left(1 - \frac{\mathrm{n}_{eff}^2}{2}\left(p_{11}+2p_{12}\right)\right)\frac{2\nu_g - 1}{E_g}P \tag{3.4}$$

In equation (3.4), λ_L is the fibre laser wavelength, E_g, ν_g are the Young's modulus and Poisson's ratio of silica glass fibre. The DFB fibre laser used in the study consists of a 35 mm long π-phase-shifted grating written on an Erbium -Ytterbium doped fibre. Application requirement of this sensor demands it to have sufficient mechanical sensitivity such that the frequency changes due to ambient acoustic noise is greater than the frequency noise floor of the fibre laser. The mechanical sensitivity required for the application of these sensors in a sea state zero environment where the ambient noise levels are as low as $160\mu\mathrm{Pa}/\sqrt{\mathrm{Hz}}$ at 1kHz [59] can be calculated from equations (3.1) and (3.4). Though there are fibre lasers with frequency noise as small as $10\mathrm{Hz}//\sqrt{\mathrm{Hz}}$ at 1kHz [27], the values reported in the literature vary from 10-35 $\mathrm{Hz}/\sqrt{\mathrm{Hz}}$ at 1kHz [4, 35, 60, 61]. The frequency noise of the fibre laser used in this study is considerably larger and a value of $62\mathrm{Hz}/\sqrt{\mathrm{Hz}}$ at 1kHz estimated from measurements suggests the pressure sensitivity (η_P) should be greater than $2\times10^{-9}\mathrm{Pa}^{-1}$ to produce measurable

phase changes in sea state zero ambient noise conditions. As optical fibres have a very large elastic modulus (72 GPa), the resultant pressure sensitivity is only $2.5 \times 10^{-12} \mathrm{Pa}^{-1}$. Compliant mechanical packaging, which leads to a reduction in the stiffness of the active sensing region, is often employed to improve the sensitivity. However reducing the stiffness also lowers the fundamental natural frequency of the active sensing region. It is desirable to have the resonances well away from the operating band to ensure a flat frequency response. Hence to achieve the performance objective of high and flat sensitivity over a large frequency range, the stiffness of the active sensing region needs to be optimised while minimising the mass associated with the fundamental mode of vibration.

The distortion free dynamic range of the fibre optic hydrophones depends directly on the phase sensitivity of the hydrophone system (Equation. (3.1a)) and phase modulation schemes employed. Phase generated carrier (PGC) schemes are commonly used in opto-electronic instrumentations for underwater acoustic sensing applications, as it is capable of achieving high dynamic range and fine phase resolutions. PGC-DCM (Differentiation and Cross multiplication) and PGC-Arctangent schemes are the most widely used among them. Many variants of these techniques have also been developed in the past to address the harmonic distortions associated with the fibre laser light intensity noise and errors associated with the modulation depth [62–65]. These schemes enable us to achieve total harmonic distortion (THD) factors smaller than 0.1% (harmonic suppression $>$ 60dB), provided sufficiently high enough carrier frequency is employed. The harmonic distortion characteristics of major PGC schemes will be discussed in detail in Chapter 4. As a general rule it could be stated that, for a given carrier frequency, THD values can be minimized by using lowest possible phase sensitivity value that meets the noise floor requirements of

the sensor. Thus the pressure sensitivity of the active sensing region directly depends on the frequency noise of the fibre laser output. Hence the optical path difference in the interferometer is the only major independent parameter (in equation (3.1a)) that determines the distortion free dynamic range and sensitivity of the sensor.

The sensor system should also need to be made insensitive to hydrostatic pressure. At a typical operational depth the hydrostatic pressure could be many orders greater than the acoustic pressure and a high mechanical sensitivity could lead to large shifts in the wavelength. This is a problem in multi-channel sensor arrays that use wavelength division multiplexing. In schemes, that use dense wavelength division multiplexing (DWDM) static pressure could push the fibre laser wavelength beyond the passband of the DWDM filter or result in the overlapping of channels. In some cases lack of pressure compensation may lead to structural failures under the action of hydrostatic pressures. Though external pressure compensation techniques could be applied, integrating the pressure compensation scheme into the encapsulation could lead to a more compact and less complex sensor configuration. Temperature variations experienced during operation can also lead to wavelength changes. But the temperature sensitivity values of the fibre is too small to cause significant wavelength changes for normal temperatures observed in the sea. (More details in subsection 6.2.4)

3.3 Design configuration

A design configuration where a thin metallic plate acts as a mechanical diaphragm as shown in figure 3.1 is proposed in this work to achieve the performance objectives specified in the previous section. A distributed feedback fibre laser (DFB-FL) is centrally placed inside the aluminium

packaging. The pre-tension arrangement, which consists of a sleeve, which is supported on a threaded supporting ring. During the sensor assembly, the fibre laser is suspended through the sleeve with the aid of assembly fixture. The fibre laser is then moulded on to the sleeve and metallic diaphragm under this freely suspended condition. Their alignments are marked after the mould is completely cured. To apply pre-tension to the fibre laser, the threaded support ring portion of the assembly is rotated. Rotational motion of the sleeve is constrained during this process to ensure the assembly maintains the initial alignment marking created after moulding. Thus the rotation of the support ring results in axial motion of the sleeve and this ensures no torsional stress is applied on to the fibre during pre-tensioning. The pretension levels can be monitored online as shift in wavelength of the fibre laser using a spectrum analyser. Once required pretension levels are applied, the cap at the pretension arrangement is used to lock the slider and supporting ring to prevent further movements. The application of pretension eliminates the string modes of the fibre laser in the frequency range of interest and reduces the vibration sensitivity of the sensor. Equation (3.5) gives the frequencies corresponding to the fundamental string mode, where T_{pre} is the pretension, μ_f is the mass per unit length of the fibre and L_f is the length of the fibre laser between mouldings at diaphragm and pretension sleeve [66]. A pre-tension value of the order of 5 N is sufficient to push the strings modes beyond the frequency range of interest (0-5kHz).

$$f_n = \frac{1}{2L_f}\sqrt{\frac{T_{pre}}{\mu_f}} \tag{3.5}$$

The diaphragm-based design amplifies the strain introduced on the fibre by effectively increasing the active sensing area of the sensor. The deflection of the diaphragm due to the acoustic pressure variations will impart

corresponding strain on the fibre, which is measured as a shift in the frequency or wavelength of fibre laser output. The slider arrangement ensures the static pressure compensation by altering the slider chamber volume proportionately with the operating depth. The compressed air in the slider chamber provides necessary restoring force to move the slider back towards the original position with reduction in the external hydrostatic pressure. It is also necessary to ensure that the acoustic sensitivity of the fibre laser hydrophone is not affected by the pressure compensation scheme. Hence the air chamber behind the diaphragm is connected to the slider chamber through an acoustic low pass filter so that only very low frequency pressure changes are allowed to pass into the diaphragm chamber.

3.4 Theoretical model

The sensitivity and frequency response characteristics of the proposed design configuration are determined by the following parameters: stiffness of the diaphragm, stiffness of the fibre, stiffness of the moulding used to attach the DFB-FL to packaging, frequency response characteristics of the pressure compensation systems and effective mass of the fundamental mode of vibration of the active sensing region. As the acoustic wavelengths of interest are much larger than dimensions of the sensor under considerations, the modelling of the acoustic components of the sensor system can be done using one dimensional wave equation. A theoretical model of the fibre laser hydrophone as represented in figure 3.2 and consisting of mainly three components namely, acoustic filter, slider, and diaphragm, is discussed in the following sections. This model will be used to study the effect of design parameters on sensor performance and selection of optimum values for those parameters.

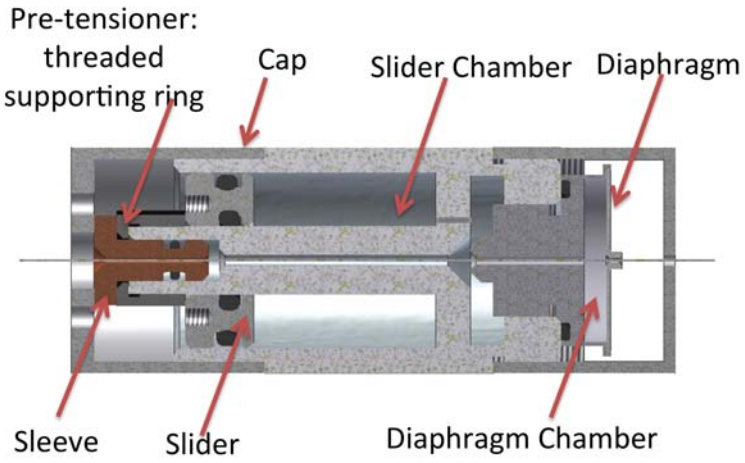

(a)

(b)

Figure 3.1: (a)Design configuration and (b) FLH prototype

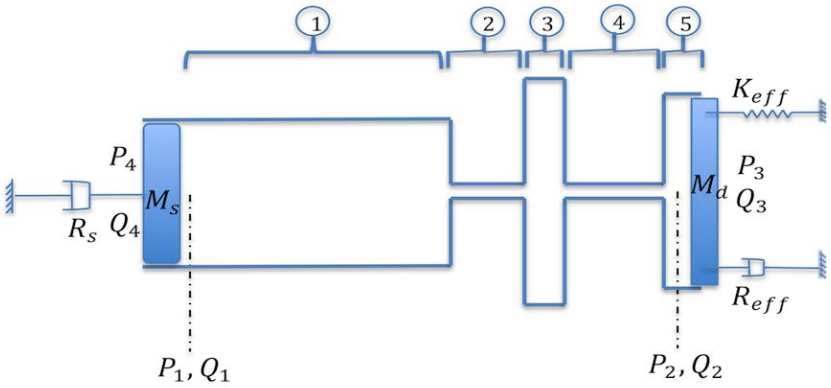

Figure 3.2: Schematic of the simplified sensor model

3.4.1 Acoustic filter

Acoustic filter of the sensor consists of five acoustic elements as marked in figure 3.2. Acoustic element 1 represents the slider chamber and its volume which will decide the operational depths up to which effective pressure compensation can be achieved. Elements 3 and 5 represent the expansion chamber and the diaphragm chamber, respectively. The sections 2 and 4 represent the links that connect the expansion chamber to the slider chamber and diaphragm chamber, respectively. An acoustic four-pole method offers a suitable tool for modelling of the sensor system as it consists of acoustic elements that could be accurately modelled using 1-D wave equations and structural elements that can be approximated using single degree of freedom second order systems. In acoustic four-pole method, the characteristics of individual sections or elements of sensor system are formulated in the form of transfer matrix, which relates the pressure and volume velocity at the input to pressure and volume velocity at the output . Thus, four-pole method allows the individual sections of the sensor to be independently modelled and then multiplied together to get the combined transfer matrix of the sensor. Figure 3.3 shows a schematic of a linear acoustic duct system of length L and cross section area S. The four-pole equation for this system can be expressed as [67]

$$\begin{bmatrix} P(0) \\ Q(0) \end{bmatrix} = \begin{bmatrix} T \end{bmatrix} \begin{bmatrix} P(L) \\ Q(L) \end{bmatrix} \tag{3.6a}$$

where

$$\begin{bmatrix} T \end{bmatrix} = \begin{bmatrix} \cos(kL) & j\left(\frac{\rho c}{S}\right)\sin(kL) \\ j(\frac{S}{\rho c})\sin(kL) & \cos(kL) \end{bmatrix}. \tag{3.6b}$$

In equation (3.6) P is the pressure and Q is the volume velocity, ρ is the density, c is the velocity of sound and k is the wavenumber. The diameters

Figure 3.3: Linear acoustic 1-D element

of the individual acoustic elements, that act as connecting links, are very small (0.25mm) and hence viscous effects plays a significant role in the attenuation of the sound energy. To incorporate this loss into the analysis, wave equations corresponding to sound propagation in a lossy medium need to be considered. For one dimensional case, the differential equations for acoustic wave in a lossy medium can be obtained from continuity and momentum equations as follows. From the continuity equation, the relation between time derivative of pressure and divergence of velocity can be written as [68]

$$\frac{\partial p}{\partial t} = -\mathfrak{B}\frac{\partial u}{\partial x}, \tag{3.7}$$

where $\mathfrak{B}$ is the bulk modulus of the medium. The momentum equation yields,

$$\frac{\partial p}{\partial x} = \rho_0 \frac{\partial u}{\partial t} + \sigma u \tag{3.8}$$

where flow resistivity σ accounts for the viscous losses in the medium. For harmonic case, using the relation $\frac{du}{dt} = j\omega u$ the equation (3.8) can be written as

$$\frac{\partial p}{\partial x} = \rho_0 \frac{\partial u}{\partial t} - j\frac{\sigma}{\omega}\frac{du}{dt}, \tag{3.9}$$

where ω is the angular frequency. Summing the results obtained through differentiating equation (3.7) with respect to t and equation (3.9) with respect to x gives

$$\frac{\partial^2 p}{\partial x^2} = \frac{\rho_0}{\mathfrak{B}} \frac{\partial^2 p}{\partial t^2} - \frac{\sigma}{\mathfrak{B}} \frac{\partial p}{\partial t} \tag{3.10}$$

Assuming a trial solution of the form

$$p(x,t) = \check{A} \exp(-j\hat{\mathbf{k}}x) \exp(j\omega t). \tag{3.11}$$

equation (3.9) yields

$$\hat{\mathbf{k}}^2 = \omega^2 \left(\frac{\rho_0}{\mathfrak{B}} - j \frac{\sigma}{\mathfrak{B}\omega} \right) \tag{3.12}$$

Algebraic simplifications, under the assumption that contribution of the flow resistivity to the real part of $\hat{\mathbf{k}}$ is negligible, yields

$$\hat{\mathbf{k}} = \frac{\omega}{c} - j \frac{\sigma}{2\rho c}. \tag{3.13}$$

In equation (3.13), flow resistivity σ accounts for the viscous losses in the duct. For circular ducts of radius a containing a fluid with dynamic viscosity μ, value of flow resistance can be expressed as in equation (3.14) [68].

$$\sigma = \frac{8\mu}{a^2} \tag{3.14}$$

Thus using equations (3.6),(3.13) and (3.14), the effective transfer characteristic of the acoustic filter section can be written as in equation (3.15) where $\left[T_1\right]$ to $\left[T_5\right]$ are the transfer functions corresponding to acoustic elements marked 1-5 in figure 3.2.

$$\begin{bmatrix} P_1 \\ Q_1 \end{bmatrix} = \begin{bmatrix} T_1 \end{bmatrix} \begin{bmatrix} T_2 \end{bmatrix} \begin{bmatrix} T_3 \end{bmatrix} \begin{bmatrix} T_4 \end{bmatrix} \begin{bmatrix} T_5 \end{bmatrix} \begin{bmatrix} P_2 \\ Q_2 \end{bmatrix} \tag{3.15}$$

The main component of the acoustic filter, that isolates diaphragm chamber from high frequency pressure fluctuations in the slider chamber, is the expansion chamber marked as element 3 in figure 3.2. In the current design the filter is chosen to have low pass cut off frequency (-3dB transmission point) 20 Hz. Figure 3.4 shows the schematic of the expansion chamber where $P_i,\ P_r,\ P_t$ represents at the amplitudes of the incident, reflected, and transmitted waves respectively. S_E & S_L represents the cross section areas at expansion chamber and connecting links respectively. Assuming anechoic termination at the output of the filter, the power transmission coefficient (T_π) can be derived as in equation (3.16) using four-pole transfer matrix formulation.

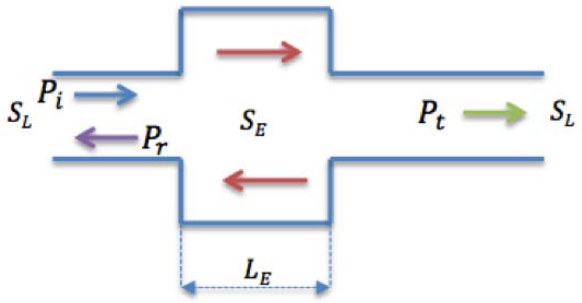

Figure 3.4: Schematic representation of the expansion chamber

$$T_\pi = \left|\frac{P_t}{P_i}\right|^2 = \frac{1}{\left(\frac{S_L}{S_E} + \frac{S_E}{S_L}\right)^2 \left(\frac{\sin(\hat{\mathbf{k}}L_E)}{2}\right)^2 + \cos^2(\hat{\mathbf{k}}L_E)} \tag{3.16}$$

The area ratio between the expansion chamber and connecting links plays the main role in controlling the cut off frequency of the acoustic fil-

ter. As the maximum allowable diameter of sensor along with assembly considerations puts the upper limit for the expansion chamber diameter, equation (3.16) can be used to decide on the dimension of the acoustic filter. Table 3.2 lists the dimensional details of filter section capable of achieving a low pass cut of frequency of 40 Hz and corresponding transmission coefficient characteristics are plotted in figure 3.5.

Table 3.2: Dimensional details of acoustic filter

Element No	Radius (mm)	Length (mm)
element 2	0.25	3
element 3	7.3	3
element 4	0.25	7

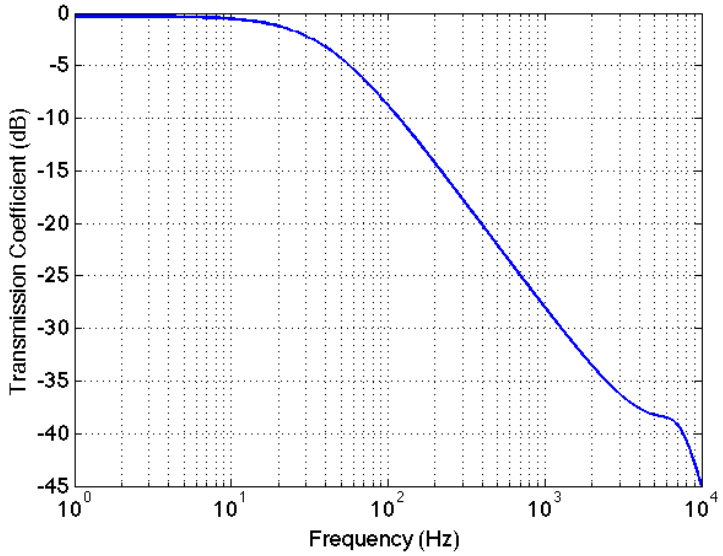

Figure 3.5: Transmission coefficient characteristics of acoustic filter configuration given in table 3.2

3.4.2 Slider

Frictional loss at the O-ring interface and acoustic radiation loss to surrounding water are the two major sources of energy dissipation at the slider. Only dynamic friction effects of O-ring sealing at the slider - slider

chamber interface is considered in the analysis, as the static friction at the interface will only introduce a fixed pressure imbalance between the outside environment and the slider chamber. The frictional loss happening at the O-rings were incorporated into the slider model using equivalent damping coefficient [69]. The radiation loss at the slider can be written as in equation (3.17) [70] where S_s is the area of slider, a_s is the radius of the slider, ρ_w is the density of water and c_w is the velocity of sound in water. As the slider motion happens in water, the added mass effect also needs to be considered. Hence total mass M_s associated with the slider motion can be written as in equation (3.18) where m_s is the mass of the slider [70].

$$R_s = \frac{1}{2}\rho_w c_w S_s (k_w a_s)^2 \tag{3.17}$$

$$M_s = m_s + \frac{8}{3}\rho_w {a_s}^3 \tag{3.18}$$

Assuming that uniform pressure acts over the entire area of the slider, its transfer characteristics can be written as

$$\begin{bmatrix} P_4 \\ Q_4 \end{bmatrix} = \begin{bmatrix} T_s \end{bmatrix} \begin{bmatrix} P_1 \\ Q_1 \end{bmatrix} \tag{3.19a}$$

where

$$\begin{bmatrix} T_s \end{bmatrix} = \begin{bmatrix} 1 & \left(\frac{j\omega M_s + R_s + C_{eq}}{{S_s}^2}\right) \\ 0 & 1 \end{bmatrix}. \tag{3.19b}$$

In equation (8) P_1 and P_4 represent the pressures acting on slider as shown in figure 3.2.

3.4.3 Diaphragm

The active sensing region of the sensor system consists of a fibre laser that is mounted centrally through a thin circular plate using a high modulus adhesive. The thin circular plate constrained at its outer diameter is exposed to water on one side and air on the other. The entire active sensing region can be represented by a single degree of freedom system as represented in figure 3.2. Deflection of a circular plate clamped at the circumference under the action of uniform pressure (P) is given in equation (3.20b) and for a concentrated load (W) applied at the centre the diaphragm, the deflection is given by equation (3.20b) [71]. In equation (3.20), E_d and E_f are the Young's modulus of the diaphragm and fibre respectively, h is the diaphragm thickness, a_d is the diaphragm radius ν_d is the Poisson's ratio for the diaphragm material, S_f is the cross section area of the fibre and L_f is the length of the fibre.

$$\delta_P = -\frac{Pa_d^4}{64\mathfrak{D}}, \tag{3.20a}$$

$$\delta_W = -\frac{Wa_d^2}{16\pi\mathfrak{D}}, \tag{3.20b}$$

where,

$$\mathfrak{D} = \frac{E_d h^2}{12(1-\nu_d^2)} \tag{3.20c}$$

Now the deflection of active sensing region to the action of pressure can be written as

$$\delta = \frac{Pa_d^4}{64\mathfrak{D}} - \frac{E_f S_f}{L_f}\delta\frac{a_d^2}{16\pi\mathfrak{D}} \tag{3.20d}$$

The effective stiffness K_{eff} of the model as expressed in equation (3.21) can be obtained by rearranging the terms in equation (3.20d).

$$K_{eff} = \frac{16\pi E_d h^3}{3{a_d}^2\left(1-{\nu_d}^2\right)} + \frac{4E_f S_f}{L_f} \tag{3.21}$$

The major source of energy dissipation at the diaphragm is the radiation loss to surrounding water. The radiation loss at the diaphragm depends on the effective volume flow rate at the diaphragm and it can be calculated using the average velocity of the diaphragm. For a vibrating circular plate of area S_d and constrained at the boundary, the average volume flow rate can be written as in equation 3.22 where u_c is the velocity amplitude at the centre. The factor 0.309 in equation (3.22) originated from the integration of the mode shape of the fundamental mode of vibration, which is essentially a Bessel function of first kind [72]. Total mass associated with the motion of the diaphragm can then be expressed as in equation (3.23). The contributions from the fibre mass is towards the effective mass associated with fundamental mode of the active sensing region is negligible in comparison to the contributions from terms given in equation (3.23) and hence neglected in the modelling.

$$Q_3 = 0.309 S_d u_c \tag{3.22}$$

$$M_d = 0.309\left(m_d + \frac{8}{3}\rho_w {a_d}^3\right) \tag{3.23}$$

Thus the transfer characteristics of the active sensing region can be written as

$$\begin{bmatrix} P_2 \\ Q_2 \end{bmatrix} = \begin{bmatrix} T_d \end{bmatrix} \begin{bmatrix} P_3 \\ Q_3 \end{bmatrix} \tag{3.24a}$$

where

$$\left[T_d\right] = \begin{bmatrix} 1 & -\left(\dfrac{j\omega M_d + R_d - K_{eff}}{{S_d}^2}\right) \\ 0 & 1 \end{bmatrix}. \tag{3.24b}$$

In equation (3.24), R_d is the radiation loss at the diaphragm which can be calculated using an expression similar to equation (3.17).

3.4.4 Sensor model

The transfer characteristics of the sensor can be expressed as a combination of the transfer function for the filter, slider and the diaphragm as given in equation 3.25. It can be assumed that $P_4 = P_3 e^{j\theta}$ and $\theta \approx 0$ as the dimensions of the sensor is much smaller in comparison to the acoustic wavelengths of interest. Thus the effective strain, ε on the fibre can be derived as in equation (3.27) using equations (3.25) and (3.22) as detailed in equation (3.26).

$$\begin{bmatrix} P_4 \\ Q_4 \end{bmatrix} = \left[T_s\right]\left[T_1\right]\left[T_2\right]\left[T_3\right]\left[T_4\right]\left[T_5\right]\left[T_d\right]\begin{bmatrix} P_3 \\ Q_3 \end{bmatrix}$$
$$= \begin{bmatrix} T_{11} & T_{12} \\ T_{21} & T_{22} \end{bmatrix}\begin{bmatrix} P_3 \\ Q_3 \end{bmatrix} \tag{3.25}$$

$$P_4 = T_{11}P_3 + T_{12}Q_3 \tag{3.26a}$$

$$Q_3 = \left(\frac{e^{j\theta} - T_{11}}{T_{12}}\right) P_3 \tag{3.26b}$$

now substituting for $Q_3 = 0.309 S_d u_c$

$$u_c = \left(\frac{e^{j\theta} - T_{11}}{0.309 S_d T_{12}} \right) P_3 \tag{3.26c}$$

Now substituting $u_c = j\omega x_c$ where x_c is the displacement at the diaphragm centre, and then dividing both sides with L_f we get equation for strain as given in equation (3.27)

$$\varepsilon = \frac{j3.24 \left(T_{11} - e^{j\theta} \right)}{\omega L_f S_d T_{12}} P_3 \tag{3.27}$$

For a fibre laser under the action of axial strain, the pressure sensitivity can be written as in equation (3.28) [32] where p_{ij} are the strain-optic coefficients and n_e is the effective refractive index of the fibre laser.

$$\eta_P = \left[1 - \frac{{n_e}^2}{2} \left(p_{12} - \nu \left(p_{11} + p_{12} \right) \right) \right] \varepsilon \tag{3.28}$$

The frequency response of the pressure compensation scheme can be derived using equations (3.24) and (3.25) as a ratio of the diaphragm chamber pressure to the external pressure as expressed in equation (3.29).

$$\mathbb{H}(\omega) = 1 - \left(\frac{e^{j\theta} - T_{11}}{T_{12}} \right) \left(\frac{j\omega M_d + R_d - K_{eff}}{{S_d}^2} \right) \tag{3.29}$$

The stiffness of the diaphragm is inversely related to the second power of diaphragm diameter and any reduction in diaphragm diameter will lead to corresponding reduction in sensitivity values. As discussed in Section 3.2, the sensitivity has a direct effect on the measurement resolution and noise floor of the sensor. The inherent frequency noise or intensity noise usually decides the sensor system as other noise contributions can be controlled by proper selection suitable opto-electronics instrumentation and careful

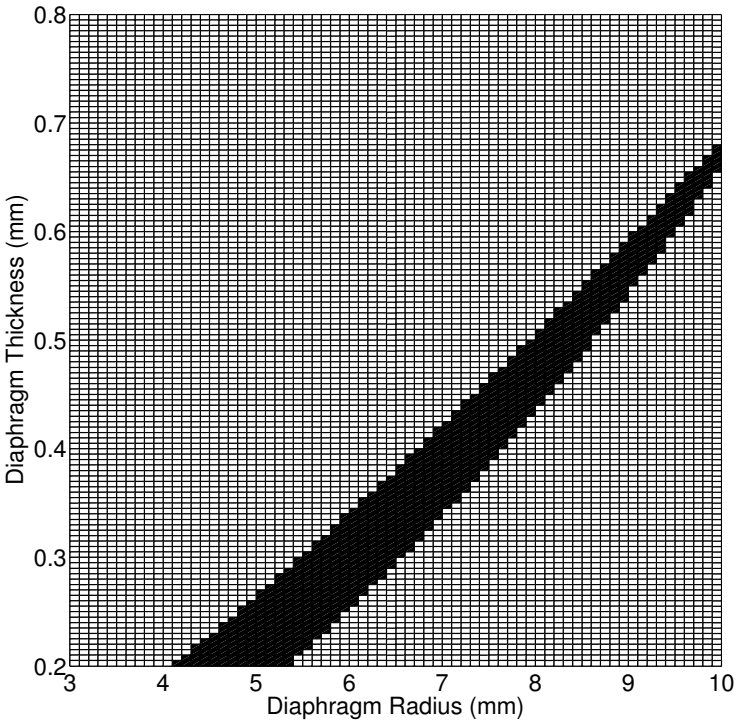

Figure 3.6: Effect of diaphragm dimensions on the sensor performance. The black coloured region of the graph satisfies the requirements on sensitivity and fundamental natural frequency

selection of optical path difference in the interferometer. Thus for the fibre lasers used in the current study the mechanical sensitivity should be greater than $2 \times 10^{-9}\text{Pa}^{-1}$ to produce measurable phase changes in low ambient noise conditions. But, the sensitivity improvements by increase in diaphragm diameter is also limited by constrains on maximum allowable sensor dimension. Moreover we need to keep the fundamental resonance as high as possible to achieve a frequency response that is flat. The fundamental natural frequency of the active sensing region is then mainly controlled by the effective mass of the active sensing region. The added mass from the surrounding fluid is the major contributor to the effective mass involved in the fundamental vibration mode of the active sensing region. From equation (3.23), it can be observed that mass associated with diaphragm motion is a cubic function of the diaphragm diameter. This also limits the achievable sensitivity improvements through increase in diaphragm diameter. Thus required sensitivity levels should be achieved through diaphragm thickness reduction.

The sensor model expressed in equations (3.28) and (3.29) can be used for the optimisation of the design parameters. To achieve the design objectives, the fundamental natural frequency and pressure sensitivity values of the systems were chosen to be more than 7.5kHz and $2 \times 10^{-9}\text{Pa}^{-1}$, respectively. A parametric study was performed by varying the thickness and the radius of the diaphragm. An acoustic filter configuration listed in table 3.2 is used in the analysis. Figure 3.6 shows the results from the parametric study and the region marked in black represents the acceptable operating points for which the natural frequency and sensitivity values met the design requirements.

It can be observed that the range of dimensional configuration that gives required performance increases with reduction in diaphragm diame-

ter. This arises due to the the fact that the effective mass of active sensing mode has a cubic dependence on diaphragm diameter while the stiffness has a quadratic dependence. Hence the diaphragm diameter reduction results in wider increase of the fundamental mode frequency, allowing for wider selection of diaphragm thicknesses. Though a performance matrix constructed by multiplying mechanical sensitivity of the sensor to its fundamental natural frequency will yield higher values for lower diaphragm diameters, the dimensions of the engineering requirements like acoustic filter, pre-tension arrangement, slider sealing, ease of assembly and ease of fabrication usually sets the lower limits on the diaphragm diameter. For example, the area ratio at the expansion chamber of acoustic filter will also decrease with decrease in diaphragm diameter thus requiring a much finer acoustic links leading to increaser complexity in fabrication. Details of the engineering considerations and practical aspects in sensor fabrication and assembly are detailed in section 6.1. The major contribution to the effective length of the sensor comes from the slider chamber. The length of the slider chamber depends on the dimensions of diaphragm and other elements of the acoustic filter. Static pressure compensation up-to a depth of 50 m requires the slider chamber to have at the least five times the volume of remaining acoustic elements.

Above discussed principles lays the guidelines to arrive at a working sensor configuration that meets the design specifications given table 3.1. The prototype sensor configuration arrived at based on above guidelines uses a metal diaphragm of 0.35 mm thickness and 7mm radius and has an overall diameter of 20 mm and length of 55 mm. Theoretical model was used to fine tune the dimension of the acoustic filter used in the pressure compensation arrangement. Detailed drawings of the sensor configuration are given in Appendix C. Figure 3.7 shows the transmission characteristics of the pres-

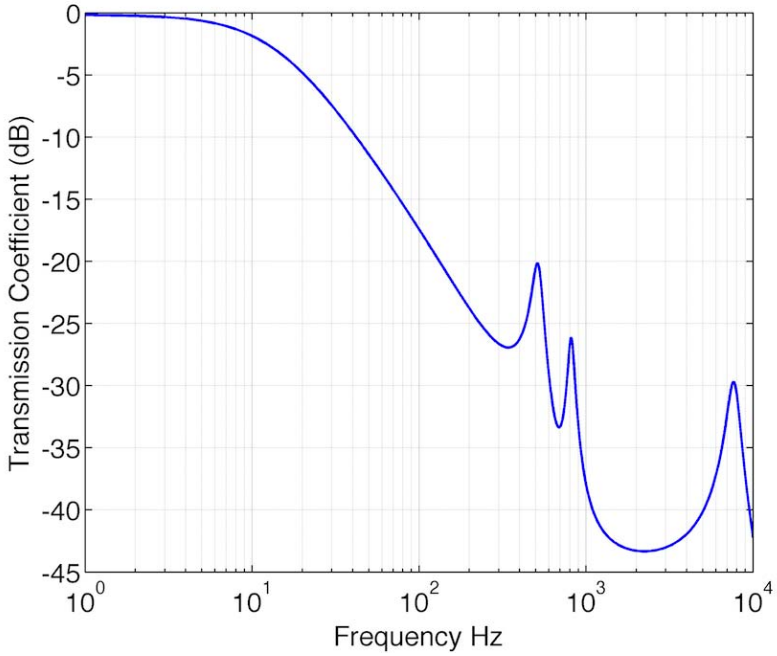

Figure 3.7: Frequency response characteristics of the pressure compensation scheme

sure compensation scheme obtained using equation (3.29). As can be seen from the plot, pressure compensation scheme allows the equalisation of the diaphragm chamber pressure and has a low pass cut off frequency of 15 Hz. It the attenuates pressure variations happening at higher frequencies. The peak observed around 7500Hz correspond to the diaphragm resonance and the peaks around 500Hz and 800Hz correspond to cavity resonances of the acoustic filter. These peaks get attenuated by more than 20dB due to the effect of radiation resistance at the slider and viscous losses in the acoustic filter. Figure 3.8 shows the simulated frequency response characteristics of the prototype. A flat frequency response within ±2dB with linear phase response characteristics is predicted in frequency range 10Hz-5kHz.

The distortion free dynamic range (distortion ratio $<$ -60dB) of sensor configuration depends on optical path difference in the interferometer, distortion characteristics of demodulation scheme, and electronic noise floor of the opto-electronics. The detailed analysis of distortion characteristics of

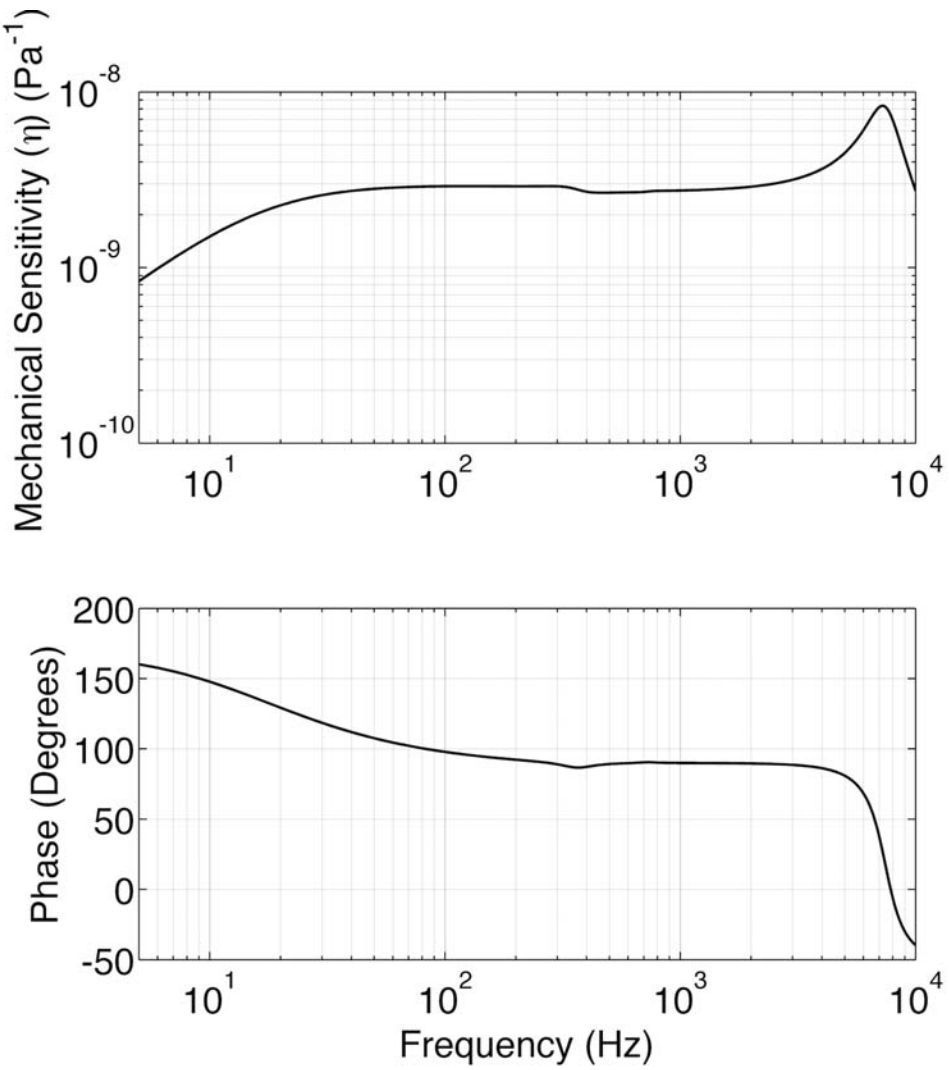

Figure 3.8: Frequency response characteristics prediction from theoretical model

demodulations schemes are presented in Chapter 4. Commercial phase demodulator from OPTIPHASE is selected is chosen in the present study due to two main reasons. The demodulation algorithm developed by Optiphase is capable of achieving required distortion ratios for the frequency range of interest up to amplitude levels as high as 1 radian (see figure 4.15). Secondly its self noise levels are as low as $3\mu\text{rad}/\sqrt{\text{Hz}}$. The minimum optical path difference required that will achieve same electrical and optical noise floor can be calculated by substituting fibre laser frequency noise values in equation (3.1). This yields an optical path difference of 1.5 m. This optical path difference can now be used in equation (3.1) along with mechanical sensitivity radians/Pa. As the demodulator is capable of achieving distortion ratios better than -60 dB up to amplitude levels as high as 1 radian, the sensor system is capable of achieving distortion free dynamic ranges in excess of 100 dB.

3.4.5 Performance prediction: FEA

Finite element analysis (FEA) of the proposed design configuration was carried out using ABAQUS® software to validate the results obtained from simplified theoretical model and to further optimise the design parameters. Figure 3.9 shows the axisymmetric finite element model of the DFB FL based hydrophone. Analysis was performed in two stages. In the first stage a static analysis was performed to incorporate the effect of pretension into the analysis, which was then followed by a steady state dynamic analysis. Fluid structure interaction effects between sensor shell and fluids (air inside the cavity and surrounding water) were taken into account in the model to include the effects of fluid loading on the sensor and radiation losses. The viscous losses in the acoustic filter were modelled using volumetric drag property of acoustic medium available in ABAQUS® software. Volumet-

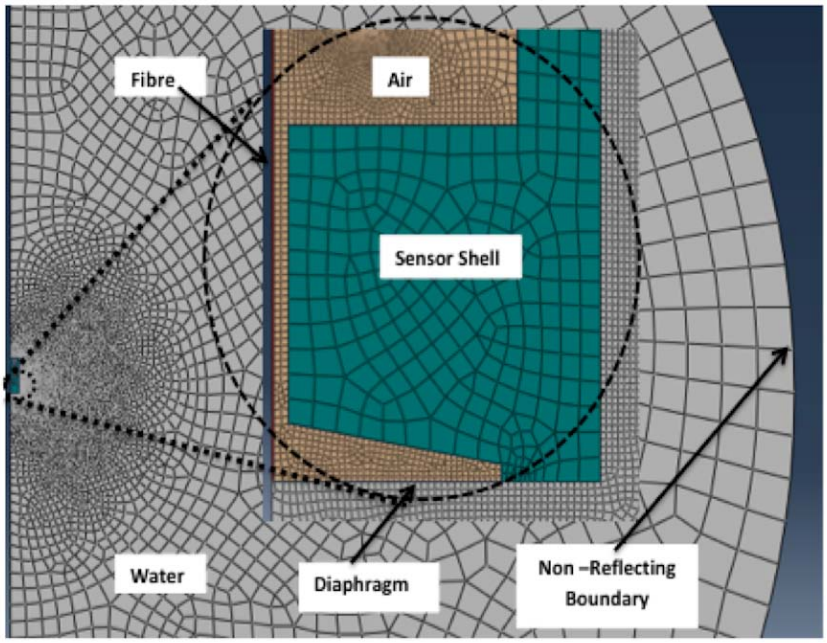

Figure 3.9: FEA model

ric drag is defined as the force experienced by acoustic medium per unit volume per unit velocity. The theoretical values of flow resistance obtained for each element of the acoustic filter using equation (3.14) were applied to corresponding domain in the finite element model. Plane wave excitations were applied on the sensor using acoustic propagation models available in ABAQUS®. Non-reflecting impedance boundary condition was applied on the outer boundary of external fluid domain and a scattered wave formulation was used in the analysis. Steady state dynamic analysis was carried out over the frequency range of interest to predict the sensitivity and frequency response characteristics of the sensor. Figure 3.10 shows the scattered pressure distribution around the sensor for a plane wave excitation at 4100 Hz and amplitude of 1 Pa. Figure 3.11 shows the comparison between the FEA results and the frequency response predicted by simplified theoretical model. It can be observed that the simplified theoretical model accurately predicts the response of the sensor system. The resonance frequency and peak amplitude predicted by the simplified analytical model

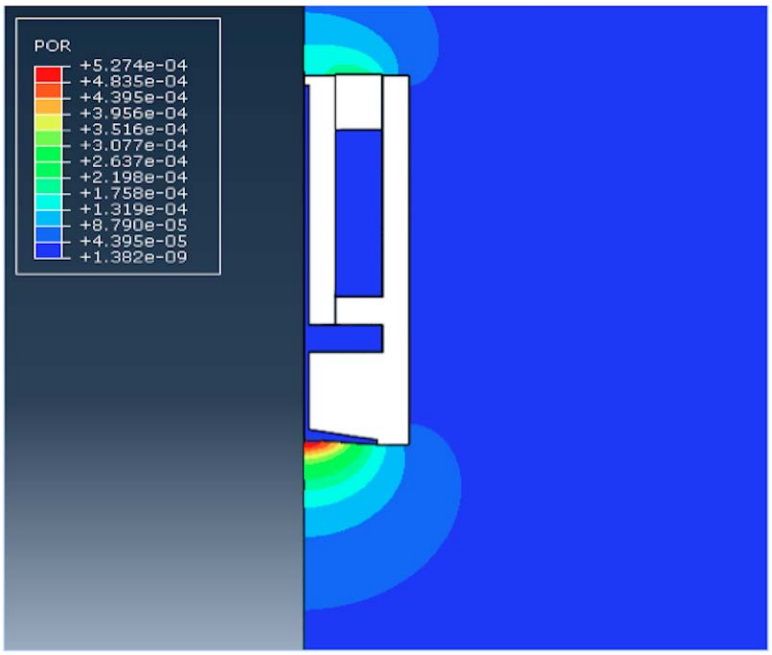

Figure 3.10: Scattered pressure amplitude (in KPa) distribution from axisymmetric finite element analysis

deviates marginally from the results obtained from the FEA. The natural frequency predicted by the analytical model is higher compared to the simplified theoretical model of the diaphragm as it neglects actual geometry and the effects of epoxy moulding at the centre of the diaphragm, which introduces additional mass and reduction in stiffness of the diaphragm. It was also observed that the changes in diaphragm resonance with pretension in the fibre was negligible for the configuration investigated as the bending stiffness of the diaphragm is the major parameter that controls the strain sensitivity as well as the natural frequency for the proposed configuration. Acoustic radiation by a diaphragm mounted on an infinite baffle is used for the estimation of the radiation loss in the simplified model. This differs from the actual scenario and over predicts the losses at the diaphragm and results in a flatter response at the fundamental resonance.

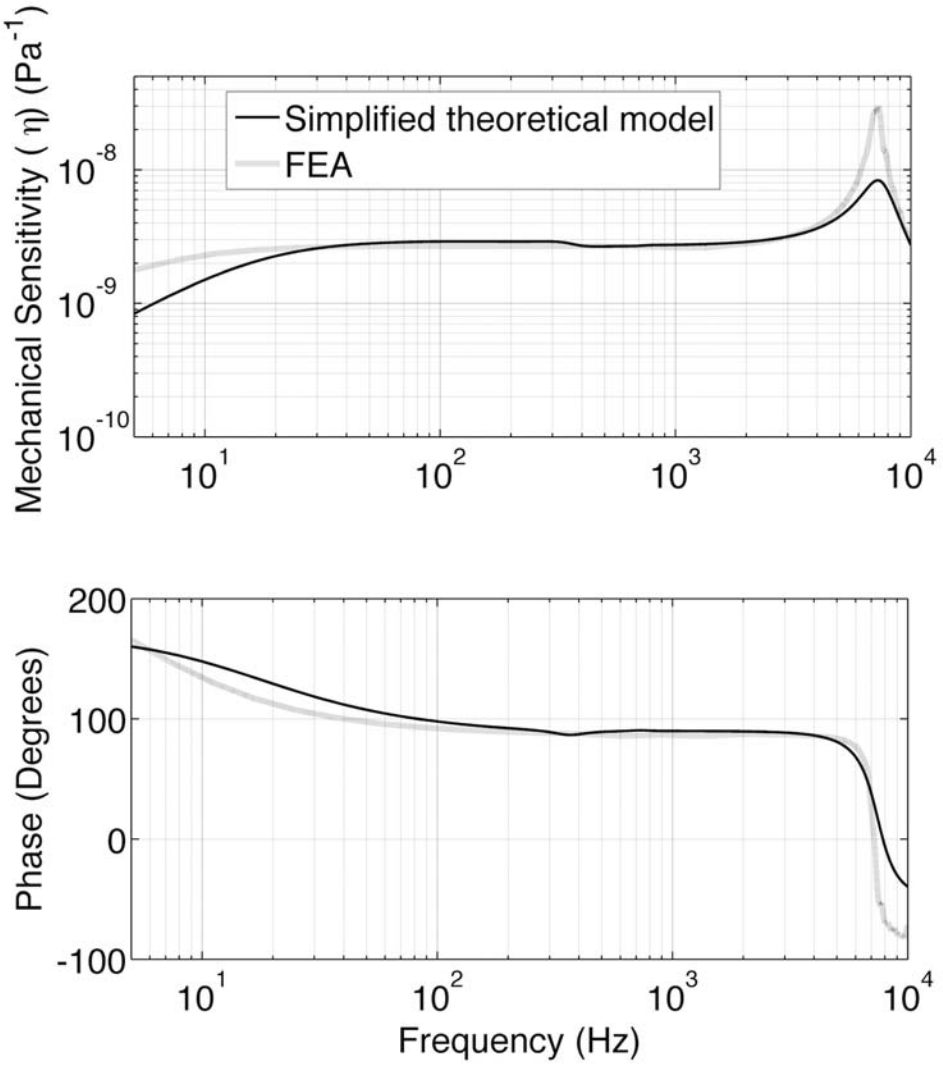

Figure 3.11: Comparison between theoretical and FEA results

3.5 Conclusion

Major design considerations in the development of a fibre laser hydrophone for underwater acoustic sensing applications have been presented. Development of a simplified analytical model for the pressure compensated metal diaphragm hydrophone has also been discussed and results have been presented. An optimum configuration of the hydrophone packaging parameters was selected based on the simplified analytical model and the same is validated using axisymmetric FEA. Though the prediction from the simplified analytical model deviates from FEA predictions at the fundamental resonance of the active sensing region, the amplitude and phase response from simplified model closely follows the predictions obtained form FEA simulations.

Chapter 4

Harmonic Distortion in Demodulation Schemes

4.1 Introduction

Interferometric systems are generally used in high performance sensing systems that demand a combination of high sensitivity, fine measurement resolution, and large dynamic range. The performance of a simple interferometeric system, as given in figure 2.1, is limited by phenomenon called signal fading and associated signal distortion. Signal fading arises due to the drifts in phase difference between the arms of the interferometer caused by random environmental excitations. As given in equation (2.2a), the output intensity of the interferometer is a cosine function of the differential phase between the arms of the interferometer. Linear operating range of such a configuration is limited to very small phase changes around a fixed differential phase of $\pi/2$. When the fixed phase offset between the arms of the interferometer is near 0 or π, the intensity variations due to the phase changes are significantly reduced due to cosine form of the interferometer output (equation (4.1)), resulting in signal fading. In fibre laser

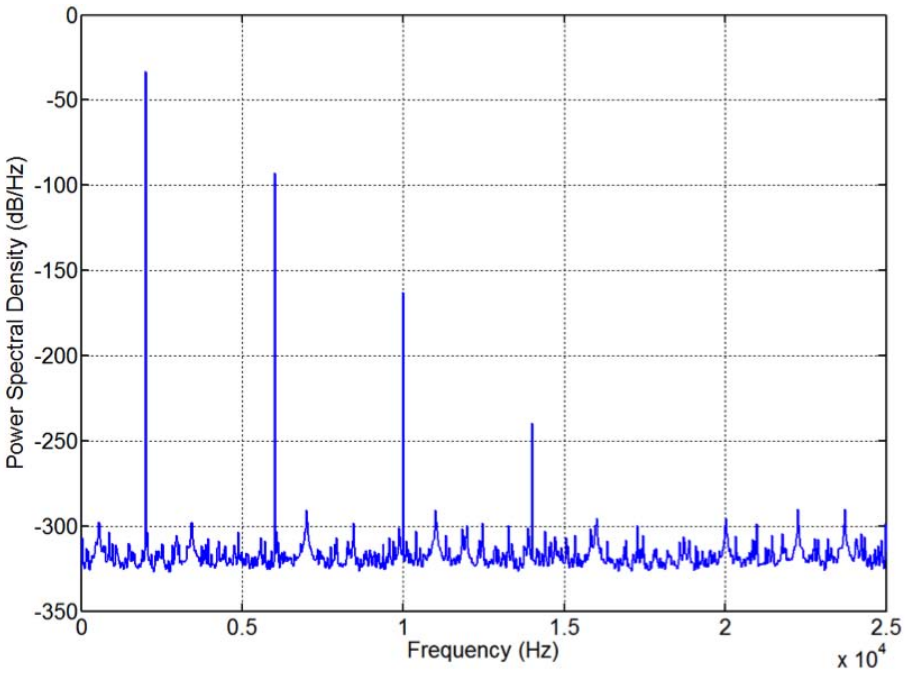

Figure 4.1: Spectrum of $\cos(\pi/2 + 0.15\sin(2\pi ft))$ where $f = 2000Hz$

hydrophones, any random frequency drifts in the lasing frequency arising from temperature fluctuations can also contribute to signal fading and harmonic distortion. Even at the most suitable operating point (mean value of phase $= \pi/2$) the non-linearity introduced due to the cosine function will result in harmonic distortion as demonstrated in figure 4.1 where the spectrum of a signal of the form $\cos(\pi/2 + 0.15\sin(2\pi ft))$, $f = 2000$ Hz clearly shows the presence of harmonics. Though there are many techniques available for signal retrieval in an interferometric sensing scheme [73], phase generated carrier schemes (PGC) are widely employed as they are capable of achieving fine phase resolutions and large dynamic ranges [62].

PGC-arctangent and PGC - differentiation and cross multiplication (DCM) are two of the most widely used PGC schemes in fibre laser sensing applications. While the PGC-arctangent scheme is capable of rejecting the noise contributions from laser intensity noise, its performance is affected by any deviation in modulation index from its most suitable value of ≈2.63 [62]. Similarly PGC-DCM scheme performance is affected by the

laser intensity noise while the effect of modulation depth variation is minimal [74]. Many variants of PGC-DCM and PGC-arctangent schemes have been developed in the past to address some of their drawbacks [64, 74]. In all these schemes, the quadrature components of the signal ($\cos(\phi(t))$ and $\sin(\phi(t))$ where $\phi(t)$ is the phase change signal) are recovered form the interferometer output through the application of low pass filters. Any error in this estimate of the quadrature components can lead to distortions in the demodulated output even in the absence of laser intensity noise and variations in the modulation depth.

Signal distortion is an important aspect in the development of fibre laser hydrophone system as the distortion free dynamic range of the sensor is mainly controlled by the demodulation technique employed in signal reconstruction. While there are some previous works on signal distortion in PGC schemes, all these works assume the absence of spectral overlapping between the signal information on adjacent harmonic carriers. This chapter address this issue by analysing the distortion characteristics of major PGC demodulations schemes in presence of spectral overlapping. This chapter is organised into three major sections. Section 4.2 presents the theory behind different PGC-techniques considered this chapter. Distortion characteristics of widely cited PGC schemes are analysed in section 4.3 followed by a summary of findings.

4.2 Theory

In a fibre optic interferometric sensing application that uses PGC demodulation, a sinusoidal carrier signal is introduced into one of the arms of the unbalanced interferometer. This carrier signal modulates the signal information which appears as sideband components of the harmonics of the

carrier signal. The schematic of a Mach-Zehnder interferometric configuration for fibre laser based sensing using PGC scheme is shown in figure 2.7. In this configuration, a modulation signal is introduced into the interferometer output though the fibre stretcher placed in one of the arms of the interferometer. The output of the unbalanced interferometer can be written as in equation 4.1 [62] where the values of A and B are proportional to the input optical power, C is the modulation depth, J_n are the Bessel functions of first kind of order n and $\phi(t)$ is the phase change signal of interest. From equation (4.1) it can be observed that the odd and even harmonics of the modulation signal carry the quadrature components $\cos(\phi(t))$ and $\sin(\phi(t))$ respectively. PGC-Arctangent and PGC-DCM schemes and their variants estimate a pair of quadrature components from the interferometer output to reconstruct the signal.

$$\begin{aligned} I &= A + B\cos\left(C\cos(\omega_c t) + \phi(t)\right) \\ &= A + B\left\{\left[J_0(C) + 2\sum_{k=1}^{\infty}(-1)^k J_{2k}(C)\cos\left(2k\omega_c t\right)\right]\cos\phi(t)\right. \\ &\quad \left. - \left[2\sum_{k=0}^{\infty}(-1)^k J_{2k+1}(C)\cos\left((2k+1)\omega_c t\right)\right]\sin\phi(t)\right\} \end{aligned} \tag{4.1}$$

The block digram representation of the technique used for retrieval of the quadrature components of phase change signal is shown in figure 4.2. The output of the interferometer (electrical signal from the photo detector) is mixed with an odd harmonic and an even harmonic (ω_c and $2\omega_c$) of the carrier signal and then low pass filtered to remove terms above half the modulation frequency to obtain signals $\mathbb{S}_1$ and $\mathbb{S}_2$. Signals $\mathbb{S}_1$ and $\mathbb{S}_2$ can be written as in equation (4.2) where G and H are the amplitudes of the mixing signals [62].

A block diagram representation of the PGC-DCM (differentiation and

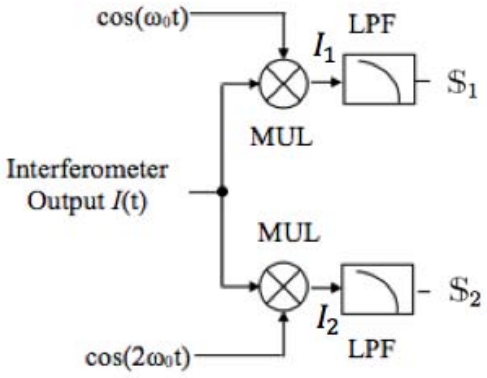

Figure 4.2: Block diagram of the technique used for estimation of the $\cos\phi(t)$ and $\sin\phi(t)$ from interferometer output

cross-multiplication) scheme is shown in figure 4.3 . In PGC-DCM scheme, the signals $\mathbb{S}_1$ and $\mathbb{S}_2$ in equation (4.2) are differentiated, cross multiplied, subtracted and then integrated to retrieve the signal back as show in equation (4.3). It can be observed that the amplitude of DCM algorithm output depends on optical power and mixing efficiency through the factor B. Thus any variation in the intensity of the light from the fibre laser can introduce change in B. The effect of intensity variation could be addressed through the application of an automatic gain control circuit as proposed in reference [63]. In PGC-arctangent scheme, arctangent of the ratio of the signals in equation (4.2) reproduces the signal as represented in equation (4.4a) when $J_1(C) = J_2(C)$ [62]. Any deviation from this optimum value of C will introduce signal distortions in the demodulated output. Thus, the PGC-arctangent scheme requires the modulation depth to be maintained at an optimum value of 2.63 radians at which the amplitudes of the first and second Bessel harmonics are equal. The quadrant of operation (quadrant corresponding to the phase shift signal) is identified from the signs of signals $\mathbb{S}_1$ and $\mathbb{S}_2$. While the PGC-arctangent scheme is capable of rejecting the noise contributions from laser intensity noise, modulation depth variations

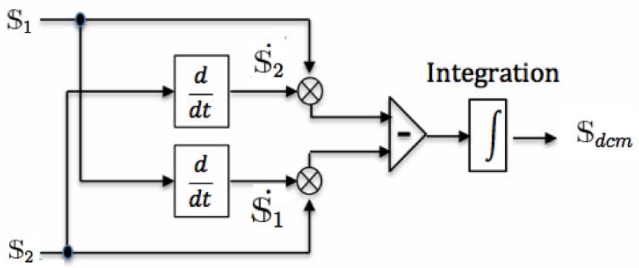

Figure 4.3: Block diagram representation of PGC DCM algorithm

have minimal impact on PGC-DCM scheme performance.

Signal distortion is one of the important performance metrics of the PGC demodulation schemes, especially in their digital implementations. The presence of Bessel harmonics of the signal necessities use of a carrier signal that is many times higher than the maximum frequency of interest. Moreover, all the major PGC algorithms require the photo detector output to be sampled at least 6 times the carrier frequency. The maximum sampling frequency is generally limited by the hardware used and total number of channels in the array. Liu et.al. [65] analysed the non-linearity in PGC-DCM algorithm due to the presence of ripples in the passband of low pass filters. A quantity named signal slope frequency (SSF), which is a measure of instantaneous rate of change of the phase change signal, was used in calculating harmonic distortion values. They observed a reduction in distortion values with increase in filter order and reduction in passband ripples, but hardware sets a limitation on the maximum filter order. The harmonic distortions due to modulation depth variation in PGC-arctangent schemes have been analysed in reference [64] and an expression for harmonic distortions arising due to small variations in modulation depth has been

presented.

$$\mathbb{S}_1 = -BGJ_1(C)\sin\phi(t) \tag{4.2a}$$

$$\mathbb{S}_2 = -BHJ_2(C)\cos\phi(t) \tag{4.2b}$$

$$\mathbb{S}_{dcm} = \int \left(\mathbb{S}_2\dot{\mathbb{S}_1} - \mathbb{S}_1\dot{\mathbb{S}_2}\right) dt = B^2HGJ_1(C)J_2(C)\int \dot{\phi(t)}dt \tag{4.3}$$

$$\mathbb{S}_{arctan} = \arctan\left(\frac{\mathbb{S}_1}{\mathbb{S}_2}\right) = \arctan\left(b\tan\phi(t)\right) \tag{4.4a}$$

where

$$b = \frac{J_1(C)}{J_2(C)} \tag{4.4b}$$

Many variants of PGC-DCM and PGC-arctangent algorithms have been developed in the past to address some of their drawbacks [64, 74, 75]. He et. al. [64] presented a demodulation scheme named ameliorated PGC to address the susceptibility of PGC-arctangent scheme to modulation depth variations. In ameliorated PGC, the ratio of the Bessel amplitudes, denoted by b as in equation (4.4b), is evaluated from signals $\mathbb{S}_1$ and $\mathbb{S}_2$ through a differentiation and self multiplication as expressed in equation (4.5). This estimate of b is then used to correct for modulation depth variations in

arctangent algorithm given in equation (4.4a).

$$Y_1 = \mathbb{S}_1\dot{\mathbb{S}}_1 = -B^2J_1^2(C)\dot{\phi(t)}\sin(\phi(t))\cos(\phi(t)) \tag{4.5a}$$

$$Y_2 = \mathbb{S}_2\dot{\mathbb{S}}_2 = B^2J_2^2(C)\dot{\phi(t)}\sin(\phi(t))\cos(\phi(t)) \tag{4.5b}$$

$$b = \sqrt{-\frac{Y_1}{Y_2}} \tag{4.5c}$$

Another method which tries to mitigate the effect of light intensity noise on the performance of PGC-DCM algorithm is presented by Tong et al. [74]. Their method utilises the sideband information from the first three harmonics of the carrier signal instead of two used in other methods. This additional information along with recurrence relation of Bessel function is used to account for the light intensity noise. Another method that accounts for the modulation depth variation in PGC-arctangent scheme is proposed by Yang et.al. [75] as given in equation (4.6). Similar to the method used in conventional arctangent algorithm, the signs of signals $\mathbb{S}_1$ and $\mathbb{S}_2$ are used in the identification of quadrant, thus extending the phase range limit of $(0, \pi/2)$ provided by the $\tan^2(\phi(t))$.

$$Y_3 = \mathbb{S}_1\dot{\mathbb{S}}_2 = -B^2J_1(C)J_2(C)\dot{\phi(t)}\sin^2(\phi(t)) \tag{4.6a}$$

$$Y_4 = \mathbb{S}_2\dot{\mathbb{S}}_1 = B^2J_1(C)J_2(C)\dot{\phi(t)}\cos^2(\phi(t)) \tag{4.6b}$$

$$\phi(t) = \arctan(\sqrt{-\frac{Y_3}{Y_4}}) \tag{4.6c}$$

One of the key assumptions used in all these studies, is the absence of spectral overlapping. Spectral overlapping arises when the frequency components of $\cos(\phi(t))$ or $\sin(\phi(t))$ carried over a Bessel harmonic of the modulation signal overlaps into the sideband of the adjacent Bessel harmonics. Though spectral overlapping is always present, its effects are negligible when the signal amplitudes are very small and signal frequencies are significantly smaller compared to the carrier frequency. But as the signal frequency and amplitude increase, the energy of the signal components in the overlap region also increases correspondingly. The quadrature components of the signal, which is being measured, are recovered through the application of filters in general. Thus the occurrence of spectral overlapping introduces error in the estimation of quadrature components of the phase change signal resulting in distortions in the demodulated output even in the absence of laser intensity noise and variations in the modulation depth. The effect of spectral overlapping on distortion performance of PGC-DCM and PGC-arctangent scheme is analysed in section 4.3.

Bush et al. presented a phase generated carrier algorithm that eliminates the low pass filtering stage in the estimation of quadrature components [76]. This method was patented by Optiphase Inc. and will be referred as PGC-optiphase in this thesis. PGC-optiphase algorithm uses a modulation signal of the form given in equation (4.7). The output from the interferometer is synchronously sampled in conjunction with a feedback loop servo controller that keeps the phase of the modulation signal $\phi_c = 0$. Feedback loops are also used to maintain a constant modulation depth of π radians.

$$MS = \pi \sin(\omega_c t + \phi_c) \tag{4.7}$$

The interferometer output can be written as

$$\begin{aligned} I &= I_{dc} + I_{ac}\cos(MS + \phi(t)) \\ &= I_{dc} + I_{ac}\cos(\phi(t))\cos(MS) - I_{ac}\sin(\phi(t))\sin(MS) \end{aligned} \tag{4.8}$$

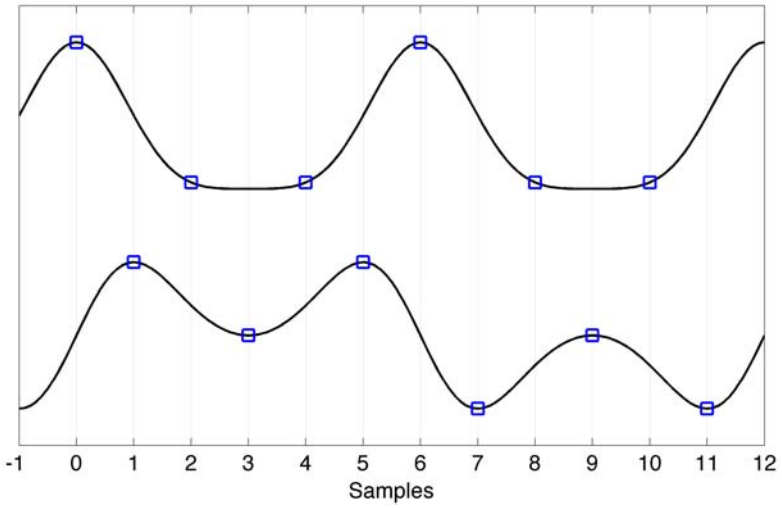

Figure 4.4: Demonstration of twelve point sampling in PGC-optiphase algorithm

The interferometer output is sampled such that there are 12 equally spaced samples in every modulation cycle. While modulation amplitude and modulation signal phase are maintained at their ideal values π and 0 respectively, the properties of the modulation signals $\cos(MS)$ and $\sin(MS)$ enables estimation of quadrature components $\cos(\phi(t))$ and $\sin(\phi(t))$. Figure 4.4 shows the pictorial representation of the signals $\cos(MS)$ and $\sin(MS)$ over a single modulation cycle. Let A_0 to A_{11} represent the amplitudes of the interferometric output corresponding to the points marked in the plot. Now consider a representative point 6. Equation for intensity at point 6 can be written as in equation (4.9).

$$\begin{aligned} A_6 &= I_{dc} + I_{ac}\cos(\phi(t))\cos(\pi) - I_{ac}\sin(\phi(t))\sin(\pi) \\ &= I_{dc} - I_{ac}\cos(\phi(t)) \end{aligned} \tag{4.9}$$

Similar equations can be written for other points. Under the assumption that change in the signal $\phi(t)$ during a modulation cycle is negligible, equations of quadrature components of the signal can be expressed as

$$4I_{ac}\sin(\phi(t)) = (A_7 - A_1) + (A_{11} - A_5) \tag{4.10a}$$

$$4I_{ac}\cos(\phi(t)) = (A_0 + A_6) - (A_3 + A_9). \tag{4.10b}$$

From this point onwards, an algorithm similar to PGC-arctangent can be used to retrieve the signal from the quadrature components. The algorithm estimates the errors in modulation amplitude and phase using equation (4.11) and uses these error values in control loop feedback to maintain the modulation amplitude and phase of the signal at their ideal values. In equation (4.11), M is the actual modulation amplitude.

$$Erramp = (A_3 - A_9) = 2I_{ac}(\pi - M)(\sin(\phi(t))) \tag{4.11a}$$

$$Errphase = (A_6 - A_0) = 2I_{ac}M\phi_c(\sin(\phi(t))) \tag{4.11b}$$

This method avoids the application of low pass filters in estimation of quadrature components. One of the fundamental assumptions in this algorithm is that the change in signal $\phi(t)$ in a single modulation cycle is negligible. This assumption is valid when the signal amplitudes are small and frequency is very small in comparison with the modulation frequency. But, it breaks down as the signal slope frequency increases leading to signal distortions. The average time, over which the estimate of $\sin(\phi(t))$ and $\cos(\phi(t))$ are obtained, is another important aspect of this algorithm. Notable improvement in distortion performance can be achieved by selecting data samples such that the same average time is used in the estimation of

$\sin(\phi(t))$ and $\cos(\phi(t))$. The formula for $\cos(\phi(t))$ given in equation (4.10) can be modified as in (4.12) to achieve same averaging time and improved distortion performance.

$$4I_{ac}\cos(\phi(t)) = \left(\frac{A_0 + A_{12}}{2} + A_6\right) - (A_3 + A_9). \tag{4.12}$$

Distortion performance of all the three PGC methods discussed in this section are compared in following section.

4.3 Distortion due to spectral overlapping

The signal that is being measured is assumed to be of the form given in equation (4.13). The quadrature components of the signal can also be represented using Bessel series expansion as given in equation (4.14). A pictorial representation of the application of the low pass filter to obtain $\sin\phi(t)$ from signal marked I_1 in figure 4.2 is given in figure 4.5. Equation (4.2) shows the desired forms of the quadrature components estimated in the PGC scheme when mixing signals of unit amplitude are employed. But the low pass filtering results in removal of some of the higher order Bessel harmonics in the quadrature components of the phase change signals ($\cos\phi(t)$ and $\sin\phi(t)$). In addition the spectral overlapping from the sidebands of the adjacent Bessel harmonics of the carrier signal will also manifest as spurious signals in the estimates of $\cos\phi(t)$ and $\sin\phi(t)$ as marked in figure 4.5.

$$\phi(t) = D\cos(\omega t) + \phi_0 \tag{4.13}$$

$$\cos\left(\phi(t)\right) = \left[J_0(D) + 2\sum_{k=1}^{\infty}(-1)^k J_{2k}(D)\cos\left(2k\omega t\right)\right]\cos\phi_0 - \left[2\sum_{k=0}^{\infty}(-1)^k J_{2k+1}(D)\cos\left((2k+1)\omega t\right)\right]\sin\phi_0 \tag{4.14a}$$

$$\sin\left(\phi(t)\right) = \left[2\sum_{k=0}^{\infty}(-1)^k J_{2k+1}(D)\cos\left((2k+1)\omega t\right)\right]\cos\phi_0 + \left[J_0(D) + 2\sum_{k=1}^{\infty}(-1)^k J_{2k}(D)\cos\left(2k\omega t\right)\right]\sin\phi_0 \tag{4.14b}$$

Most of the widely used PGC schemes utilise the quadrature components

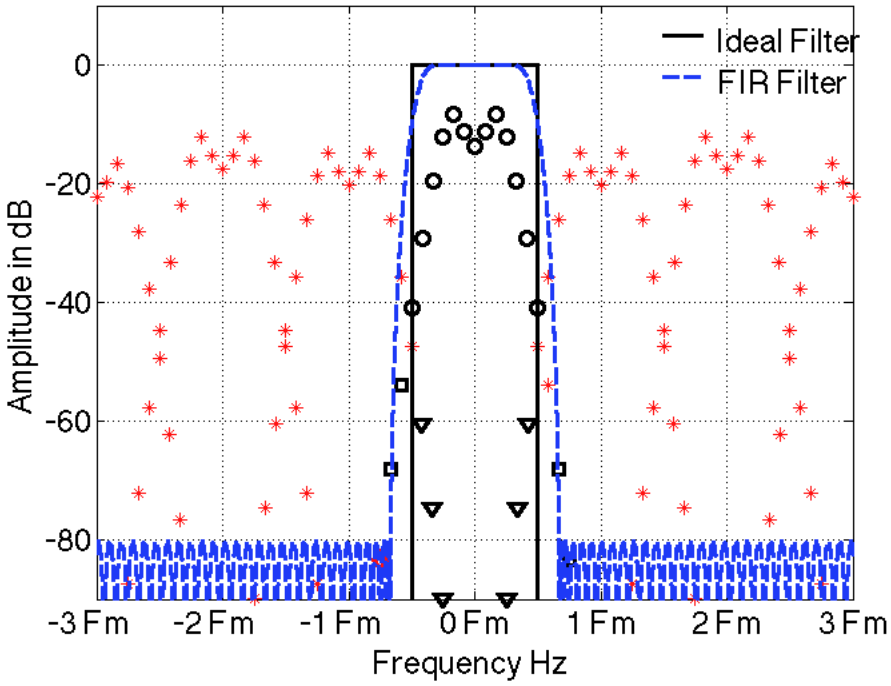

Figure 4.5: Application of the filter on the signal I_1 in figure 4.2 to estimate $\sin\phi(t)$ * - sideband signal components of higher order harmonics, ∘ - in-band components of quadrature signal,▽ - spectral overlapping from quadrature components on adjacent carrier harmonics and □ - out of band components of quadrature signal

of the phase change signal from the interferometer to reconstruct the original signal $\phi(t)$. Hence, any error in quadrature component estimation will

lead to distortions in the demodulated output. The presence of Bessel harmonics of the signal in a frequency range that lies beyond the passband of the lowpass filter employed to retrieve signals $\mathbb{S}_1$ and $\mathbb{S}_2$ is the main source of error in estimation of signals in equation (4.2). As the amplitude and the frequency of the phase change signal increases, larger number of Bessel harmonics of the signal with significant energy are pushed outside the passband. This results in corresponding increase in the signal distortion at the demodulator output. Even in the absence of spectral overlapping, passband ripples of the low pass filter can also lead to harmonic distortion as illustrated in [65]. Thus the effect of passband ripples needs to be isolated to analyse the distortions arising due to spectral overlapping. To achieve this, an ideal filter as shown in figure 4.5 is considered. Following subsections compare the distortion characteristics of PGC-arctangent and PGC-DCM schemes for two different filter characteristics; 1) ideal filter which eliminates all the frequencies above half the modulation frequency and 2) finite impulse response (FIR) filter with a frequency response as represented in figure 4.5.

4.3.1 Ideal filter

To compare the effect of spectral overlapping on PGC algorithms, an ideal filter with frequency response characteristics as given in figure 4.5 is considered in this section. In order to evaluate the distortion characteristics with an ideal low pass filter, the outputs of the low pass filtering stage is reconstructed analytically. The spectral components of the signals $\mathbb{S}_1$ and $\mathbb{S}_2$ in the passband of the ideal filter (components marked in green colour in figure 4.5) were estimated using amplitudes of the Bessel harmonics of the carrier, amplitudes of the Bessel harmonics of the signal and the DC operating point of the signal. This spectral information is then used to

obtain the time domain representations of signals $\mathbb{S}_1$ and $\mathbb{S}_2$ for further processing using equations (4.3) and (4.4a).

Distortion ratio parameter, which is defined as the ratio of the sum total of the energy at the harmonics of the signal and the energy at the spurious signals arising from spectral overlapping to the energy at signal frequency in the demodulated output, is used for performance comparison of the demodulation schemes. The parameters of the simulation are summarised in table . Carrier signal amplitude is maintained at the recommended value of 2.63 radians in the simulation to ensure most favourable operating parameters for PGC-arctangent scheme. An eleventh order differentiation scheme has been used in PGC-DCM algorithm since the performance improvement with further increase in oder of numerical differentiation was negligible. A sampling frequency $F_s = 12 \times F_c$, where F_c is the carrier frequency, is used in the simulations. Even in the absence of an anti-aliasing filter at the output of the photo detector, effect of aliasing is negligible as magnitudes of $J_n(2.63)$ are negligible for $n > 10$. The variation of distortion ratio with frequency ratio and amplitude of the signal observed in PGC-DCM and PGC-arctangent algorithms are shown in figures 4.6 and 4.7 respectively. The parameter frequency ratio represents the ratio of signal frequency to the carrier frequency $(\frac{\omega}{\omega_c})$. Distortion ratio figures smaller than -120 dB were forced to -120 dB to improve the readability of the plots in the regions where distortion is significant. Figure 4.8 compares the performance

Table 4.1: List of parameters for simulations

Parameter	Value
Modulation depth C	2.629874
Sampling frequency F_s	$12\times F_c$; F_c is the carrier frequency
Numerical differentiation scheme	11th order forward difference
Intensity noise	absent
Fibre laser frequency noise	absent

of PGC-DCM and PGC-arctangent algorithms under most favourable con-

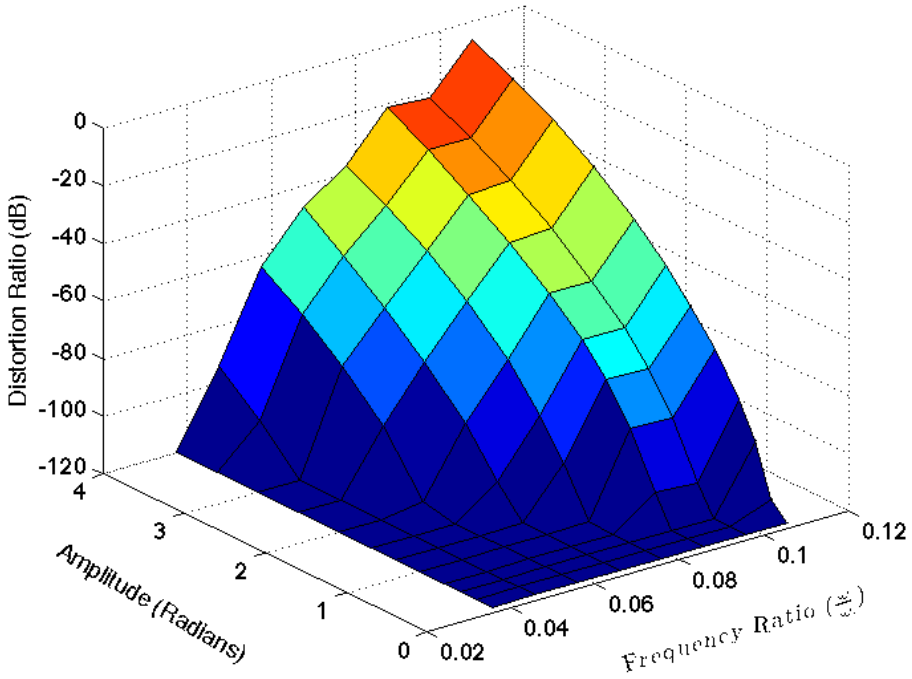

Figure 4.6: Variation in distortion characteristics of PGC-DCM scheme with frequency ratio and signal amplitude for an ideal filter

ditions (i.e. absence of frequency and intensity noise, modulation depth $C = 2.6298$, and an ideal low pass filter for estimation of quadrature components). Distortion ratio values at sample frequency ratios are presented in figure 4.8. It could be observed that the PGC-arctangent algorithm has lower distortion compared to PGC-DCM algorithm. The distortion ratio increases with increase in signal frequency and signal amplitudes as more number of Bessel harmonics are pushed beyond cut off frequency of the low pass filter. It is evident that even under most favourable conditions, modulation frequency should be at least 10 times the signal frequency to achieve distortion ratios better than -60 dB for a sinusoidal signal with 1 radian amplitude. The effect of modulation depth on PGC-arctangent scheme in the context of spectral overlapping is studied by varying the modulation depth in the range 2.56 to 2.7 which corresponds to a deviation of the order of 3% from the recommended value. Modulation depth variations of

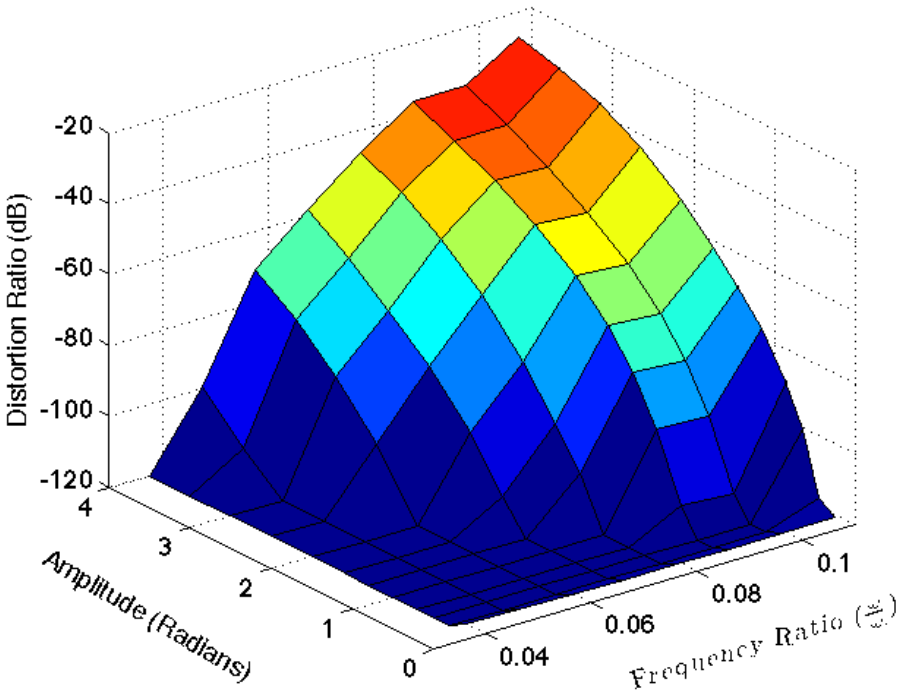

Figure 4.7: Variation in distortion characteristics of PGC-arctangent scheme with frequency ratio and signal amplitude for an ideal filter and modulation depth is maintained at the ideal values of C=2.629874

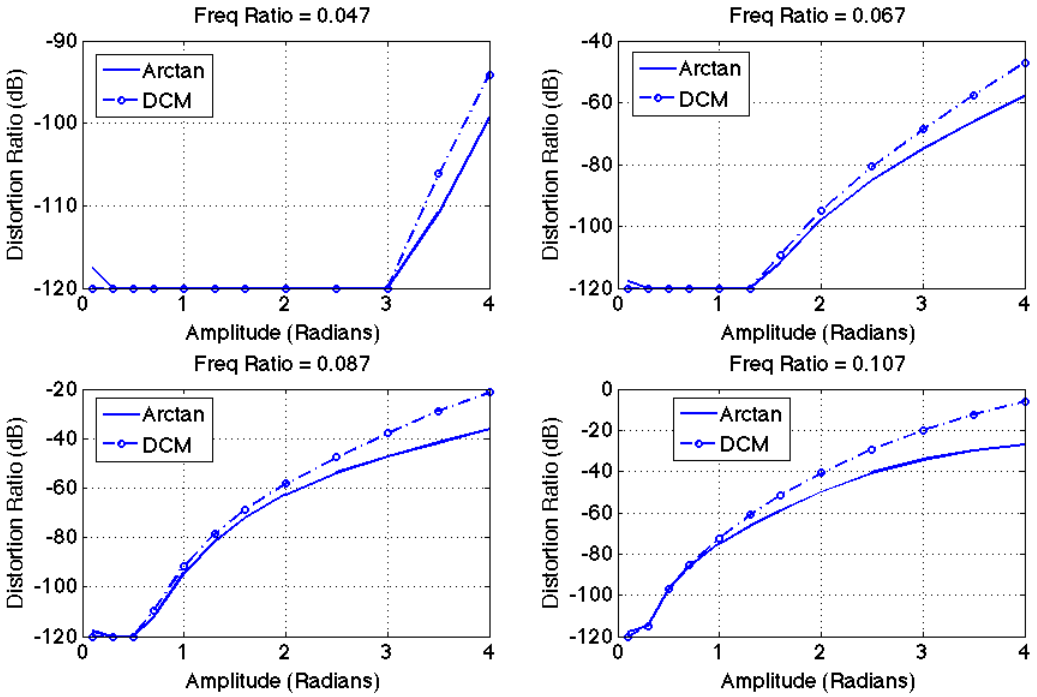

Figure 4.8: Comparison between distortion ratios in PGC-DCM and PGC-artangent algorithms. An ideal filter is employed in the estimation of quadrature components and a most suitable modulation amplitude C=2.6295 radians is used in the simulation. Absence of frequency and intensity noises is assumed in the analysis.

the order of one to two percentage are common in fibre laser sensing using frequency division multiplexing. A procedure similar to previous analysis is used to evaluate the distortion ratio from the Bessel expression of the signal. These results are then compared with analytical predictions of harmonic distortion as expressed in equation (4.15) given by He et.al [64]. Figure 4.9 compares the distortion ratios for PGC-arctangent scheme with analytical values of total harmonic distortion (THD) for signal of 2 radian amplitude. Distortion ratio for analytical case is equal to its THD as analytical estimation ignores the effects of spectral overlapping that produces spurious signals. Though the analytical estimation of distortion ratio is independent of frequency of the signal, it can be observed that the distortion ratio increases with increase in signal frequency. Even at optimal modulation depth, significant distortions can be observed in the demodulated output due to spectral overlapping effects. This observed difference increases with increase in signal frequency and amplitude.

$$THD_{arctan} = (|b-1|)\frac{\sqrt{\sum_{k=1}^{\infty} J_{2k}^2(D)\sin^2(2\phi_0) + \sum_{k=1}^{\infty} J_{2k+1}^2(D)\cos^2(2\phi_0)}}{|D + (b-1)J_0(2D)\cos(2\phi_0)|} \quad (4.15)$$

4.3.2 FIR filter

In real applications, the frequency response characteristics of the low pass filters deviate from ideal filter. To simulate actual performance of PGC schemes, an FIR low pass filter with frequency response characteristics represented in figure 4.5, is employed in the simulation. The parameters of the filter used in the simulation are listed in table 4.2. Normally observed intensity noise figure of -120 dB/Hz is used in the study to simulate the noise in the interferometer output [60, 61]. Modulation depth value of 2.63 radians

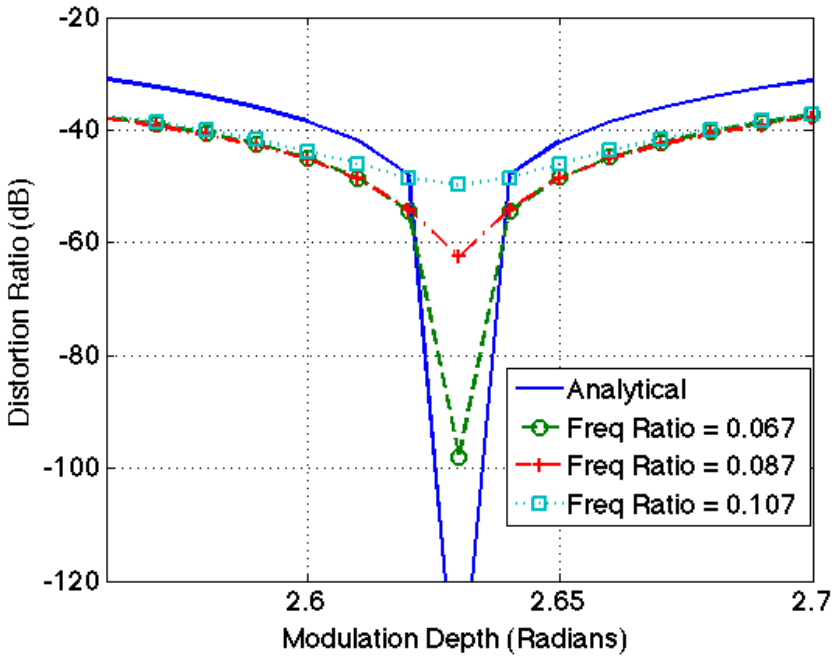

Figure 4.9: Variation in distortion characteristics of PGC-Arctangent scheme with frequency ratio and modulation depth for a phase amplitude of 2 Radians

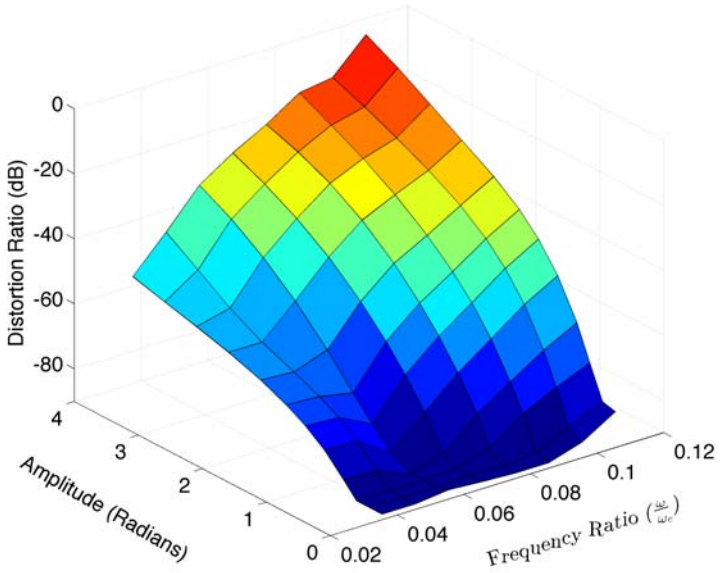

Figure 4.10: Distortion characteristics when FIR filter of order 87 is employed in the estimation of quadrature components

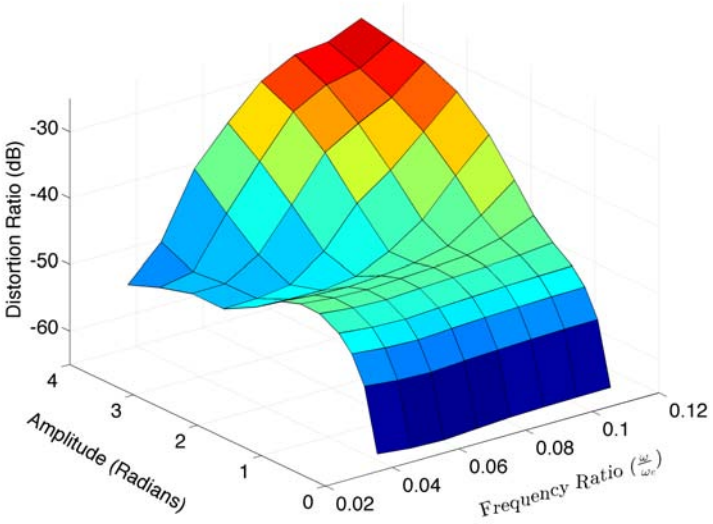

Figure 4.11: Distortion characteristics when FIR filter of order 87 is employed in the estimation of quadrature components

is used to see the effect of a practical low pass filter on the distortion performance. Results from the simulation is plotted in figure 4.12. While both the algorithms give similar performance at low frequency ratios, the PGC-arctangent algorithm gives better performance at higher frequency ratios.

Table 4.2: Parameters of low-pass FIR filter

Parameter	Value
Filter Length	87
Passband edge	$\omega_c/2$
Stopband edge	ω_c
Passband ripple	0.1 dB
Stopband Attenuation	80 dB

The phase change produced at the fibre stretcher varies among the sensors due to the difference in fibre laser wavelengths. Thus, the modulation depth can vary among the sensors in a wavelength division multiplexed configuration for normal operating conditions. A modulation amplitude of 2.61 radians which corresponds to a deviation of 0.7% from the optimum value is considered in the simulation. Figures 4.10 and 4.11 show the distortion

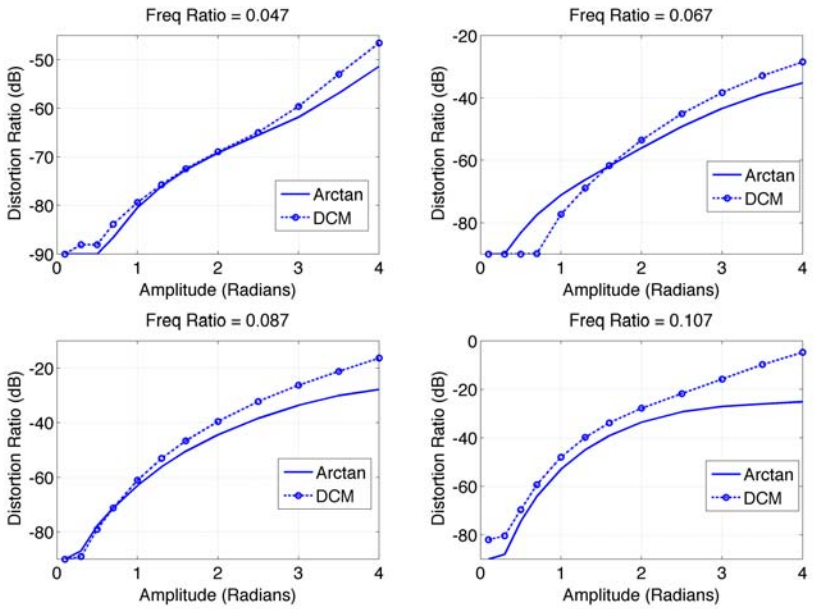

Figure 4.12: Distortion characteristics when FIR filter of order 87 is employed in the estimation of quadrature components; Modulation depth of 2.629874 is used in the simulations

ratios for the PGC-DCM and PGC-Arctangent schemes and their comparison is shown in figure 4.13. It can be observed that the performance of PGC-arctangent scheme deviates significantly due to the non-optimal modulation amplitude. In real applications, while signal amplitudes are smaller than 1 radian, the PGC-DCM schemes have lower signal distortions and its distortion ratios deteriorates rapidly as the amplitude and frequency of the signal increases. Similarly, when the signal amplitudes are of the order of a few radians, distortion is lower for PGC-arctangent scheme.

4.3.3 PGC-Optiphase

PGC-optiphase algorithm uses a carrier signal of modulation amplitude of π radians. Feedback loop controls are used to achieve this optimal condition in PGC-optiphase algorithm. For the simulation study, an error of 0.7% in modulation signal amplitude and phase is assumed. The PGC-optiphase algorithm detailed in section 4.2 was implemented in matlab

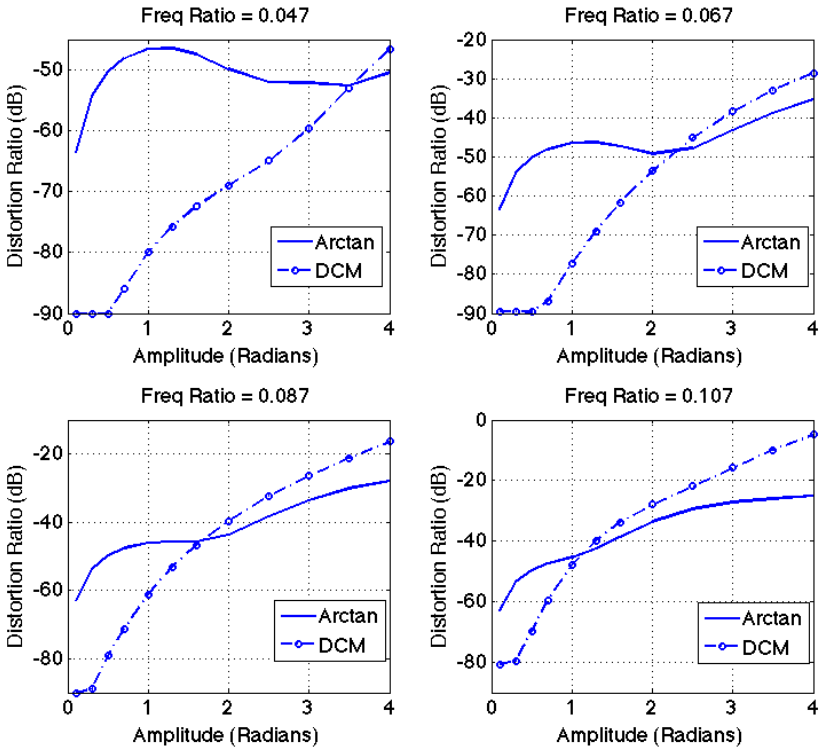

Figure 4.13: Distortion characteristics when FIR filter of order 87 is employed in the estimation of quadrature components for a 0.7% deviation from optimal modulation depth

and its distortion characteristics are studied using a method similar to the one used to evaluate the performance of PGC-arctangent and PGC-DCM schemes.

The results from the simulation study on distortion performance is given in figure 4.14. Though there is an increase in distortion characteristics with increase in frequency ratio distortion performance is better than -60 dB over most of the amplitude and frequency ratio range considered in the simulation. Figure 4.15 shows the comparison of distortion performance of PGC-optiphase algorithm with that of PGC-DCM and PGC-arctangent algorithms. It can be observed that PGC-DCM and PGC-acrtangent schemes give better performance while the signal amplitudes are very small. But as the the amplitudes and frequency of the signal increase, the distortion performance of PGC-DCM and PGC-arctanget schemes deteriorates rapidly while the performance degradation in PGC-optiphase algorithm is minimal. The PGC-optiphase algorithm provides distortion performance better than -60 dB in entire range considered in the simulation.

4.4 Conclusion

Distortion characteristics of PGC-DCM and PGC-arctangent schemes, arising due to errors in estimation of the quadrature components of the phase change signals, are presented. The quadrature component estimates ($\cos(\phi(t)$ & $\sin(\phi(t))$ where $\phi(t)$ is the phase change signal) were obtained analytically to study the effect of spectral overlapping in isolation. It was observed that even when operating under the most favourable conditions (modulation amplitude =2.63 radians, ideal low pass filter and absence of laser intensity and frequency noise) the distortion ratio of PGC-arctangent schemes vary with frequency of the signal while the analytical estimates

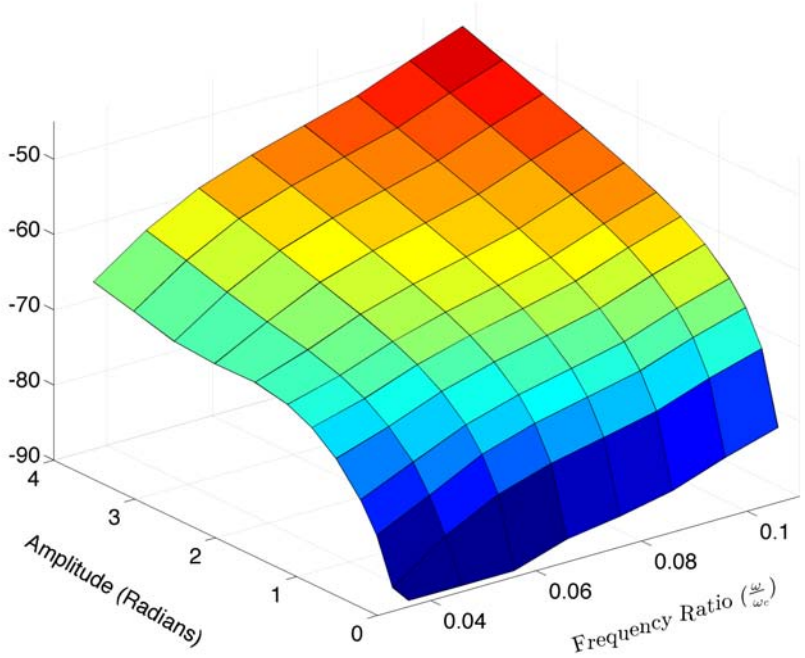

Figure 4.14: Distortion performance of PGC-optiphase algorithm

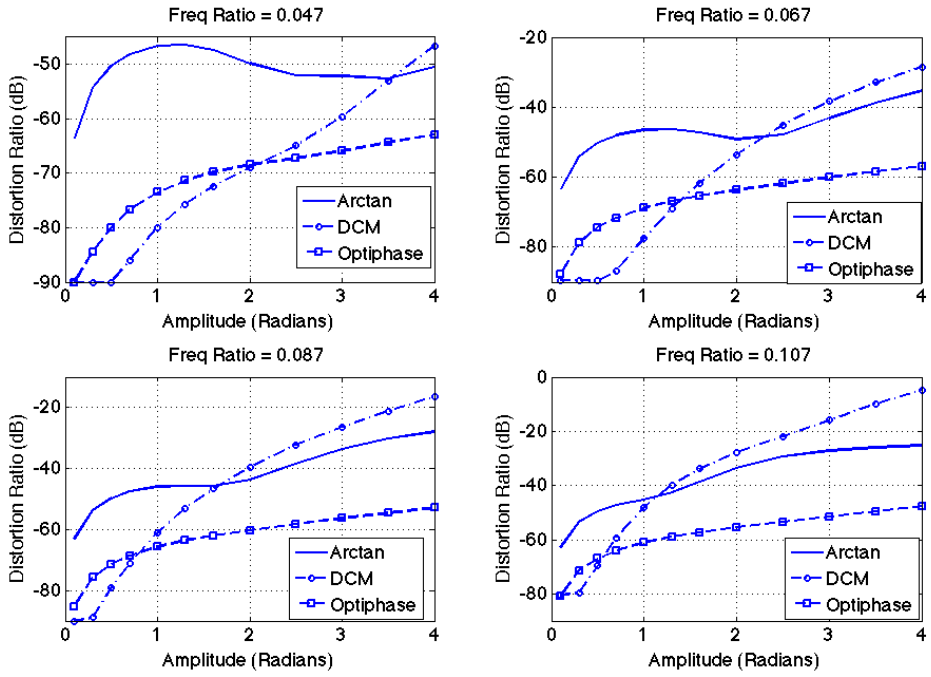

Figure 4.15: Distortion characteristics of PGC demodulation algorithms. 0.7% deviation from optimal values of modulation parameters are considered in the simulation. For PGC-DCM and PGC-artanget schemes a low pass FIR filter of order 80 is employed in the estimation of quadrature components.

of THD are independent of signal frequency. The PGC-arctangent offers better distortion performance when the signal amplitudes are of the order of a few radians while PGC-DCM scheme offers better performance for lower amplitudes for sensing applications using distributed feedback fibre laser. PGC-optiphase algorithm eliminates the low pass filtering stage in the estimation of quadrature components and it was found to give lower distortion values over the frequency and amplitude ranges of interest.

Chapter 5

Flow Noise Response

5.1 Introduction

Towed hydrophone arrays find wide application in many underwater operations like oil explorations, anti-submarine warfare, coastal monitoring etc. Figure 5.1 shows an AUV based measurement configuration in which a flexible acoustic array is towed behind an AUV for underwater surveillance. The application of towed arrays for the underwater surveillance to some extent is limited by the noise generated due to the turbulent boundary layer pressure fluctuations, usually referred as flow noise in the literature. Magnitudes of these wall pressure fluctuations depend directly on the tow speed and are also expected to increase with reduction in the towed array diameter [77, 78] with detrimental effect on the achievable signal to noise ratio (SNR) of the sensor. Thus, flow noise is one of the major considerations in estimating the performance of thin line towed arrays.

Flow noise response calculations for towed arrays require an adequate statistical model of wall pressure fluctuations and knowledge of frequency-wavenumber transfer function of the towed array packaging, response characteristics of the sensor and filtering characteristics of the array processing

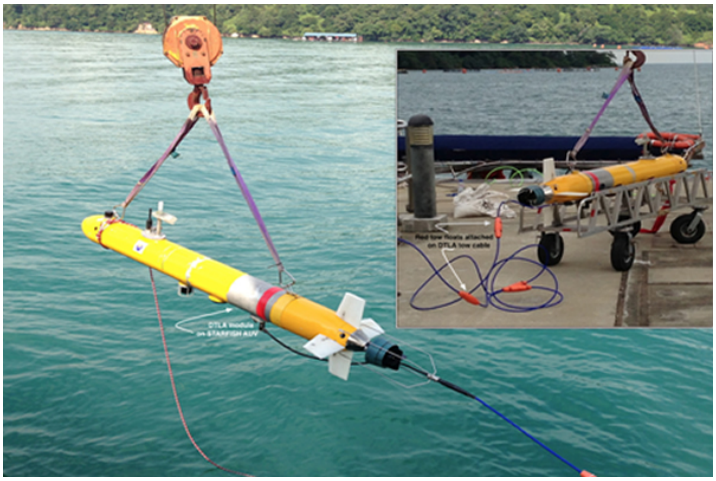

Figure 5.1: Flexible acoustic towed array on an AUV. Both the array and the AUV were developed at the Acoustic Research Laboratory of National University of Singapore.

algorithms. Carpenter and Kewley presented one of the early results on flow noise response of a fluid filled towed array and their study employed a very simple mechanical transfer function to model the response of array packaging. They observed that the predicted levels were lower than the experimentally measured noise floor [79]. A similar procedure was employed by Knight [80] to study the flow noise filtering by a group of hydrophones, but this study was also limited by the elementary transfer function used to model the wavenumber filtering by the array packaging . There have been many attempts in the past to improve upon the models of frequency wavenumber transfer characteristics of fluid filled towed arrays [81, 82]. In all of these studies, either the presence of sensors were neglected or the sensors were considered as line elements or infinite cylinders located along the axis of the array.

The fibre laser hydrophone considered in this study consists of a fibre laser sensor mounted centrally on a diaphragm. The diaphragm helps in achieving the required sensitivity values by amplifying the strain on the fibre laser and its orientation is normal to the axis of the towed array. Hence, the flow noise averaging due to finite size of the sensor along the axis is min-

imal in these diaphragm based sensors. Thus a different analysis approach for flow noise estimation is necessary and this chapter presents a finite element analysis based procedure to estimate the flow noise levels experienced by the fibre laser sensors packaged in a fluid filled elastomer cylinder. The results are then compared with the predictions from a simplified analytical model of a submerged fluid filled infinite cylinder.

This chapter is organised into 3 main sections. The array configuration and sensor details are presented in section 5.2 followed by the analytical model and finite element analysis procedure in section 5.3. Results and discussions are presented in section 5.4 followed by summary of findings and conclusions.

5.2 Fibre laser hydrophone array

The sensor configuration similar to the one described in chapter 3 is used in the construction of the array and is shown in Fig. 5.2. A distributed feedback fibre laser (DFB-FL) is centrally placed inside the aluminium packaging with one end of the fibre attached to a thin metallic diaphragm and the other end to a pre-tensioning arrangement. A water filled polyurethane tube inside which individual hydrophones are packaged as shown in figure 5.2b is considered in this study. The polyurethane tube helps in streamlining the flow and isolates the sensors from hydrodynamic disturbances in the turbulent boundary layer schematically represented in Figure 5.2. Furthermore, it serves as a wavenumber filter to reduce the flow noise experienced by the sensors.

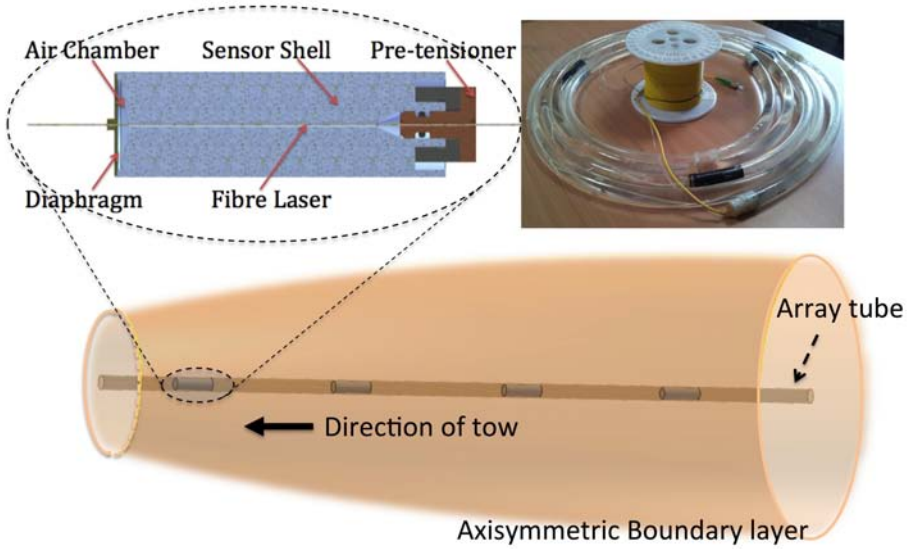

Figure 5.2: Schematics of sensor and array configurations

5.3 Theory

Two major parameters that determine the flow noise response of a fibre laser hydrophone packaged inside an array tube are the frequency wavenumber response of the sensor in packaged condition denoted by $\mathfrak{H}(\mathbf{k}, \omega)$ and the wall pressure excitation spectra $\mathbb{P}(\mathbf{k}, \omega)$. The flow noise response of the sensor in the array can be written as [83]

$$\mathbb{Q}(\omega) = \int_{-\infty}^{\infty} \mathbb{P}(\mathbf{k}, \omega) |\mathfrak{H}(\mathbf{k}, \omega)|^2 d\mathbf{k} \tag{5.1}$$

where $\mathbf{k}$ is the wavenumber vector and ω is the angular frequency.

5.3.1 Flow noise model

Wall pressure fluctuations in a turbulent boundary layer are random in nature and calculation of the response of a structure to these pressure fluctuations requires a valid statistical description of wall pressure field in wavenumber-frequency or space-time domain. Experimental results re-

ported by many researchers showed that the wall pressure field consists of a broad spectrum of wavenumber components that changes slowly with time in a reference frame that moves along with the flow [84]. One of the successful early attempts on modelling wall pressure spectra was by Corcos [83] and his model was based on narrowband spatial correlations of wall pressures on a flat plate. As per Corcos model, the spatial correlation function can be written as

$$\Gamma(\omega, \xi_1, \xi_2) = \Phi(\omega)\ \exp\left(-\hat{\alpha}|\frac{\omega\xi_1}{U_c}| - \hat{\beta}|\frac{\omega\xi_2}{U_c}| + \frac{i\omega\xi_1}{U_c}\right), \tag{5.2}$$

where ξ_1 and ξ_2 are the spatial separations along and normal to the flow direction respectively. $\hat{\alpha}$ and $\hat{\beta}$ are the constants of decay corresponding to the exponential decrease in correlation with spatial separation. U_c is the convection velocity and it has a magnitude of the order of flow velocity. Frequency wavenumber spectrum obtained by Fourier transform of equation (5.2), with parameter values estimated from curve fitting the experimental results, was used in references [85] and [86] for flow noise calculations.

Figure 5.3 shows a schematic representation of a wavenumber distribution of wall pressure spectra over a flat plate at a sample frequency and its prominent features are highlighted. Corcos model gives a satisfactory prediction of the wall pressure spectra in the “convective ridge" where majority of the flow noise energy is concentrated, but it over-predicts the levels corresponding to low and high wavenumber regions. The response peak for underwater structures may correspond to excitations by the components with phase velocities that matches the structural wave speeds corresponding to sub-convective region [84, 87]. Hence the response peaks can

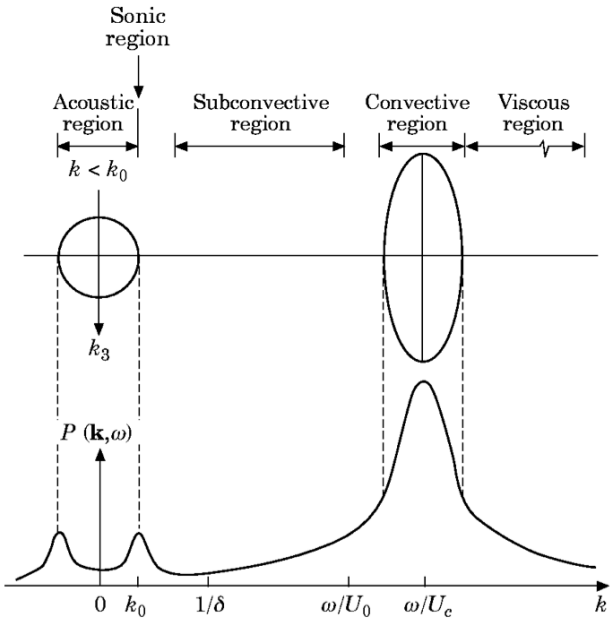

Figure 5.3: Schematic representation of variation of frequency wavenumber spectrum at constant frequency (reproduced from [84])

fall in a region corresponding to $\frac{\omega}{k_z} > U_c$ where k_z is the wavenumber along the flow. Thus the contributions from both convective and sub-convective regions are equally important. Thus, a wall pressure spectrum model that provides better predictions in the entire convective and sub-convective region is essential in obtaining reliable estimates of flow noise levels in towed sensor arrays due to turbulent wall pressure fluctuations. A review of wavenumber-frequency spectra models of TBL pressure fluctuation was presented by Graham [88]. He compared the radiated sound from a plate driven by TBL pressure fluctuations for different TBL wall pressure models using an excitation spectra which is normalised by corresponding frequency spectra. He observed that the predicted results deviated among the models, especially when the contribution from sub-convective region is significant.

Another important aspect of the TBL wall pressure model is its autocorrelation or auto-spectrum characteristic. Extensive studies were conducted in the past by many research groups to arrive at a suitable frequency spec-

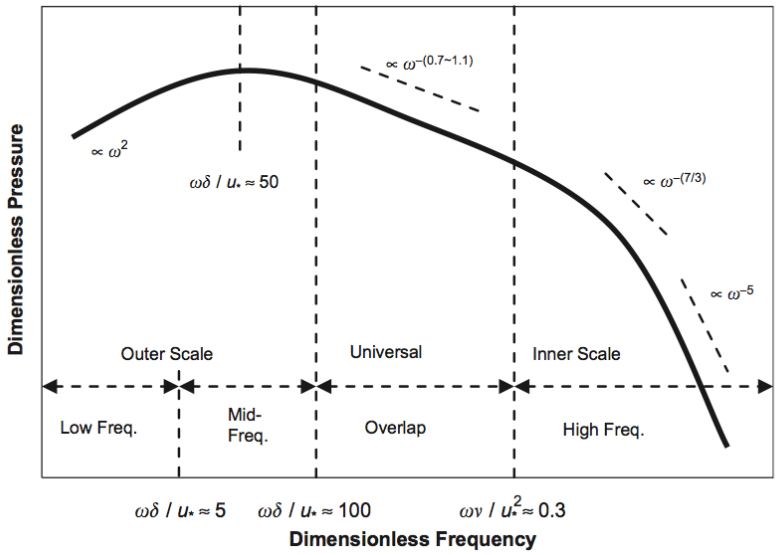

Figure 5.4: Schematic representation of variation of wall pressure spectrum (reproduced from [89])

tra model for the wall pressure fluctuations in a turbulent boundary later and a recent review by Hwang et al. [89] compares the widely cited models. Many researchers explored the possibility of a scaling method to collapse the non-dimensionalized pressure spectrum using the concept of self similarity [90–92]. Previous experimental results suggest that it would be more reasonable to use appropriate scaling in different spectral ranges based on corresponding predominant physical feature of TBL pressure fluctuations. A schematic representation of non-dimensionalized power spectral distribution against dimensionless frequency (with corresponding scaling) of wall pressure fluctuations in a turbulent boundary layer is shown in figure 5.4 (reproduced from [89]). While outer layer scaling is used in low frequency regions, better collapse of experimental data was observed through the use of inner layer scaling in high frequency region. Comparisons of wall pressure spectrum models show a gradual improvement over the years mainly due to the improved knowledge on the characteristics of TBL pressure fluctuations from experimental studies.

A recent empirical model by Goody [91] which is based on experimental results from seven research groups provides a good representation of the spectral characteristics presented in figure 5.4. His model, which is based on Chase model for wall pressure spectra [93], incorporates the effects of Reynold's number in to the model through the ratio of time scales of outer boundary layer to inner boundary layer. Goody's model for wall pressure frequency spectra is given in equation (5.3) where τ_ω is the wall shear stress, U is the free stream velocity, v_* is the friction velocity, δ is the boundary layer thickness and R_T is the time scale ratio. While this model is capable of obtaining reasonable predictions for underwater cases, its usefulness in the current study is limited as it models only frequency distribution while the energy distribution in the wavenumber domain is essential for response calculations.

$$\frac{\Phi(\omega)U}{\tau_\omega^2\delta} = \frac{3\left(\frac{\omega\delta}{U}\right)^2}{\left[(\frac{\omega\delta^*}{U})^{0.75}+0.5\right]^{3.7}+\left[1.1R_T^{-0.57}\left(\frac{\omega\delta}{U}\right)\right]^7} \tag{5.3}$$

A model for frequency wavenumber spectra for wall pressure in a turbulent boundary layer by Chase is widely used for flow noise calculations at subsonic speeds, especially for underwater case. Chase presented a semi-empirical model F-K spectra for wall pressure over a flat plate in 1980 and modified it again in 1987 to include the effects of compressibility [93, 94]. Many of the observed structural features of the cylindrical boundary layer are similar to those observed in flat-plate turbulent boundary layers even though the turbulence intensities for boundary layers over cylinders are lower than that for a flat plate case for most of the boundary layer (outer regions) as the smaller surface area of the cylinder limits the amount of vorticity introduced in to the fluid [95]. The applicability of Chase flat plate

model for prediction of axisymmetric boundary layer wall pressures was demonstrated by [96] based on wall pressure measurements on a full scale towed array. They employed measured values of axisymmetric boundary layer parameters in the Chase model ([93]) to obtain predictions matching the measured wavenumber frequency spectra. Following similar arguments used in flat plate case, [77] presented a semi empirical model of circumferentially averaged frequency wavenumber wall pressure spectra in an axisymmetric boundary layer around a cylinder. The model constants in this axisymmetric spectra are also estimated by curve fitting the model to experimental results and it can can be expressed as

$$P_0(k_z,\omega) = \mathbb{C}\rho^2 v_*^3 a^2 \frac{(12k_z^2a^2+1)}{12}\left(\frac{(\omega a - U_c k_z a)^2}{h^2 v_*^2} + k_z^2a^2 + \hat{b}^{-2}\right)^{-2.5}. \tag{5.4}$$

In equation (5.4), ρ is the fluid density; U is the tow velocity; $U_c = 0.68U$ is the convection velocity of turbulence; v_* is the friction velocity; k_z is the wavenumber along the axis of the cylinder in the direction of the flow and the suggested values of the constants are $\mathbb{C} = 0.063,\ h = 3.17,\ \hat{b} = 1.08$. This model is employed in the current study to model the excitation spectra acting on the towed array surface.

Caution should be exercised when interpreting the results obtained from Chase model as it over predicts the spectral region beyond the universal (or overlap) region in figure 5.4. Frequency-wavenumber spectrum from chase model can be integrated over the wavenumber to obtain the frequency spectrum. This frequency spectrum decay as ω^{-1} at high frequencies while the actual spectral decay is much steeper ($\omega^{-2.33}$ and ω^{-5}). Figure 5.5 presents the spectral distribution of wall pressure on a cylinder of 20 mm diameter. As it can be observed at low tow velocities, $\frac{\omega\nu}{u_*^2} > 0.3$ and

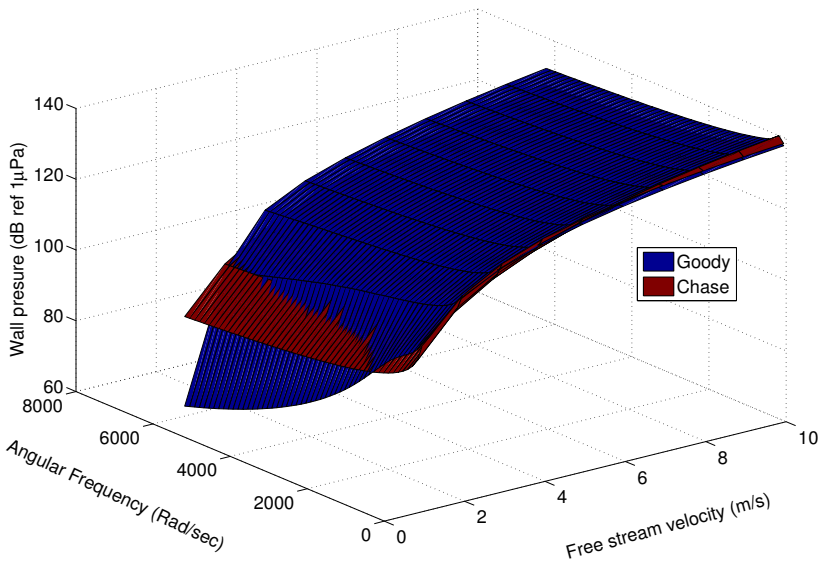

Figure 5.5: Comparison of spectral characteristics of wall pressure between Goody model and Chase model for typical thin line array of 20 mm diameter

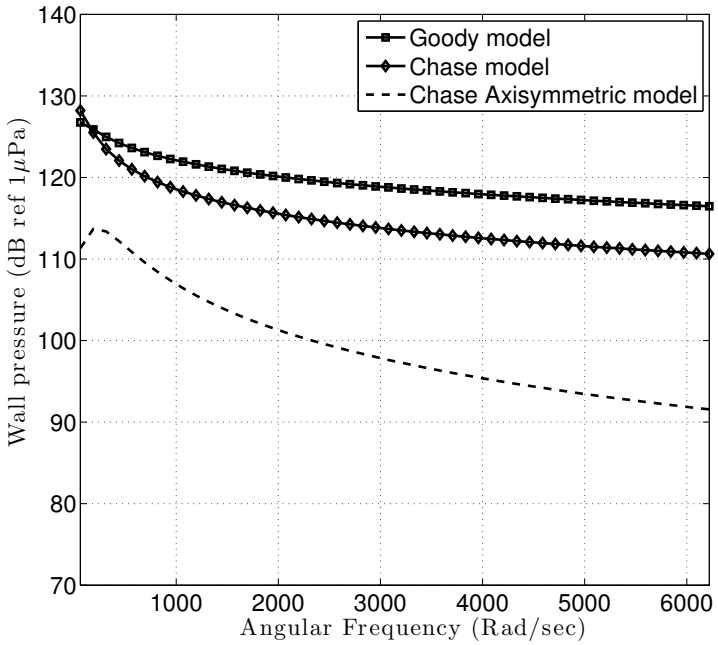

Figure 5.6: Comparison of spectral characteristics of wall pressure between Goody model and Chase model for typical thin line array of 20 mm diameter for a tow velocity of 4 m/s

the Chase model over predicts the spectral levels. Figure 5.5 plots the spectral distribution predictions from Goody model and Chase model for a tow velocity of 4 m/s and compares it against the axisymmetric spectral distribution. Though the spectral estimates from Chase model deviates by a maximum of 10 dB compared to the estimates from Goody model at high velocities, Chase spectrum is found to give predictions matching the one from Goody models for most of the operational speeds and frequency range where flow noise energy is significant.

5.3.2 Analytical model

A good insight into frequency wavenumber response characteristics of water filled towed arrays can be obtained from the analysis of an infinite fluid filled tube excited by turbulent boundary layer pressure fluctuations. The array tube can be modelled as an isotropic shell. Effects of the inside and outside fluid on the response of the tube to wall pressure fluctuations can be included in the analysis through a fluid loading term. The fluid loading term can be derived by equating normal velocities at the fluid structure interface. Following a detailed procedure given in reference [97], the equation of motions after Fourier transform can be written in terms of spectral field quantities as in Eq. (5.5). The steps involved in deriving Eq. (5.5) are detailed in Appendix.

$$\left[\mathbf{S}\right]\left[\mathbb{u}\right] = \left[\mathbb{F}\right] \tag{5.5a}$$

where

$$\left[\mathbf{S}\right] = \begin{pmatrix} \mathbf{S}_{11}(n,k_z) & \mathbf{S}_{12}(n,k_z) & \mathbf{S}_{13}(n,k_z) \\ \mathbf{S}_{21}(n,k_z) & \mathbf{S}_{22}(n,k_z) & \mathbf{S}_{23}(n,k_z) \\ \mathbf{S}_{31}(n,k_z) & \mathbf{S}_{32}(n,k_z) & \mathbf{S}_{33}(n,k_z) + f_l \end{pmatrix}, \tag{5.5b}$$

$$\left[\mathbb{u}\right] = \begin{pmatrix} \mathbb{u}_z(n,k_z) \\ \mathbb{u}_\phi(n,k_z) \\ \mathbb{u}_r(n,k_z) \end{pmatrix}, \quad \left[\mathbb{F}\right] = \begin{pmatrix} \mathbb{F}_z(n,k_z) \\ \mathbb{F}_\phi(n,k_z) \\ \mathbb{F}_r(n,k_z) \end{pmatrix}, \tag{5.5c}$$

$$\mathbf{S}_{11}(n,k_z) = -E_1\left(k_z^2 + n^2\frac{1-\nu}{2a^2}\right) - \omega^2\rho_s h, \tag{5.5d}$$

$$\mathbf{S}_{12}(n,k_z) = \frac{-E_1(1+\nu)nk_z}{2a}, \tag{5.5e}$$

$$\mathbf{S}_{13}(n,k_z) = \frac{-E_1\nu i k_z}{a}, \tag{5.5f}$$

$$\mathbf{S}_{21}(n,k_z) = \mathbf{S}_{12}(n,k_z), \tag{5.5g}$$

$$\mathbf{S}_{22}(n,k_z) = E_1\left(\frac{(1-\nu)k_z^2}{2} + \frac{n^2}{a^2} + 2k_z^2\Lambda^2(1-\nu) + \frac{\Lambda^2 n^2}{a^2}\right) - \omega^2\rho_s h, \tag{5.5h}$$

$$\mathbf{S}_{23}(n,k_z) = -E_1\left(\frac{in}{a^2} + i\Lambda^2(2-\nu)k_z^2 n + \frac{i\Lambda^2 n^3}{a^2}\right) \tag{5.5i}$$

$$\mathbf{S}_{31}(n,k_z) = -\mathbf{S}_{13}(n,k_z), \tag{5.5j}$$

$$\mathbf{S}_{32}(n,k_z) = -\mathbf{S}_{23}(n,k_z), \tag{5.5k}$$

$$\mathbf{S}_{33}(n,k_z) = E_1\left(\frac{1}{a^2} + \Lambda^2 a^2 k_z^4 + \frac{\Lambda^2 n^4}{a^2} + 2\Lambda^2 k_z^2 n^2\right) - \omega^2\rho_s h, \tag{5.5l}$$

$$f_l = \rho\omega^2\mathbb{u}_r(n,k_z)\frac{H_{|n|}(\gamma a)}{\gamma H_{|n|}{}'(\gamma a)} - \rho\omega^2\mathbb{u}_r(n,k_z)\frac{J_{|n|}(\gamma a)}{\gamma J_{|n|}{}'(\gamma a)}, \tag{5.5m}$$

$$\Lambda^2 = \frac{h^2}{12a^2}, \tag{5.5n}$$

$$E_1 = \frac{Eh}{1-\nu^2}, \tag{5.5o}$$

$$\gamma = \sqrt{({k_0}^2 - k_z^2)}, \;\; k_0 = \omega/c. \tag{5.5p}$$

Equation (5.5) is a simplified representation of the differential equations of motion for a fluid filled cylinder for time harmonic motion. In equation (5.5) $\mathbb{u}_z(n,\alpha)$, $\mathbb{u}_r(n,\alpha)$ and $\mathbb{u}_\phi(n,\alpha)$ are the spectral displacements and $\mathbb{F}_z(n,\alpha)$, $\mathbb{F}_\phi(n,\alpha)$, and $\mathbb{F}_r(n,\alpha)$ are the spectral excitations in cylindrical coordinate system along directions denoted by the subscripts. E, ν , ρ_s are the tube material's Young's modulus, Poisson's ratio and density respectively and c is the speed of sound in water and ρ is the density of water. a and h are radius and thickness of the tube respectively. In equation (5.5m) J_n and H_n are the Bessel and Hankel functions of first kind with order n. n represents the wavenumber along the circumference of the cylinder and takes only integer values. For the problem at hand, n=0 as we are interested in the axisymmetric part of the solution.

The centre line pressure should be finite and normal velocities should be equal at fluid structure interface. Application of these boundary conditions gives the equation for pressure inside the array tube and it can be written as

$$p_i(r,n,k_z) = \rho_i\omega^2\mathbb{u}_r(n,k_z)\frac{J_{|n|}(\gamma r)}{\gamma J_{|n|}{}'(\gamma a)} \tag{5.6}$$

where r is the radial location of the observation point inside the array tube.

The boundary layer pressure fluctuations over the towed array in axial flow are random in nature. They are usually characterised in terms of correlation functions or power spectral density characteristics. A relation between external excitation and flow noise spectra a point inside the array cane be obtained from equation (5.5a) by multiplying both sides with $\left[\Psi\right] = \left[\mathbf{S}\right]^{-1}$ yields

$$\left[\mathbb{u}\right] = \left[\Psi\right]\left[\mathbb{F}\right]. \tag{5.7}$$

Multiplying Eq. (5.7) with $\left[\mathbb{u}\right]^*$, where * represents the Hermitian operation, yields

$$\left[\mathbb{u}\right]\left[\mathbb{u}\right]^* = \left[\Psi\right]\left[\mathbb{F}\right]\left[\mathbb{F}\right]^*\left[\Psi\right]^*. \tag{5.8}$$

It can be assumed that the external excitation is primarily radial in nature and arise from the normal wall pressure acting at the external surfaces of the cylinder. As $\mathbb{F}_z(n,k_z)$, $\mathbb{F}_\phi(n,k_z) = 0$, Eq. (5.8) gives

$$\mathbb{u}_r {\mathbb{u}_r}^* = \Psi_{33}{\Psi_{33}}^* P_0(k_z) \tag{5.9}$$

The power spectral density of the internal pressure at any radial location, as expressed in in equation (5.10), can be derived using relations given in equations (5.6) and (5.9).

$$P_i(\omega) = \int \rho_i^2\omega^4 \left|\Psi_{33}\right|^2 \left|\frac{J_0(\gamma_1 r)}{\gamma_1 {J_0}'(\gamma a)}\right|^2 P_0(k_z,\omega)dk_z. \tag{5.10}$$

5.3.3 Wavenumber frequency response spectra : FEA

The analytical model derived in section 5.3.2 is highly simplified and completely neglects the presence of the sensors in the tube which can introduce considerable changes in acoustic modes leading to corresponding variations in predictions on flow noise response of the fluid filled arrays. Analytical representation of the response characteristics of the actual array and sensor configuration is difficult due to the complex geometrical and structural features. Hence a finite element analysis technique is used to obtain the frequency wavenumber response characteristics of the sensor packaged in a fluid filled towed array tube. An axisymmetric acoustic analysis procedure was employed in the study considering the axisymmetric nature of geometry and loading, leading to significant reduction in computational size of the problem.

Table 5.1: Material properties

Array Tube		
	Young's Modulus	1.0+0.1i Gpa
	Poisson's Ratio	0.33
Water		
	Density	1000 Kg/m^3
	Speed of Sound	1500 m/s

Figure 5.7 shows the typical configuration of the FEA model used in the study. Table 5.1 summarises the material properties used in the analysis. Visco-elastic nature of the array tube is incorporated into the analysis through a complex modulus with $\tan\delta = 0.1$. A non-reflecting boundary condition is used at the outer boundary of external fluid domain. Harmonic analysis was performed at 50 different frequencies in the range 0-500Hz to obtain an effective coverage of frequency range of interest where flow noise is significant ([98, 99]). A distributed pressure load at the external surface of the array tube with sinusoidal variation along the axis of the tube was applied to simulate excitations corresponding to different wavenumbers. The wavenumber range required for accurate prediction of flow noise levels were arrived at based on a preliminary analysis to obtain response characteristics of the sensor configuration. The spatial distribution of the time harmonic load applied on the tube was varied over a wavenumber range of 0.01-6500 radians/m to cover the frequency wavenumber domain where structural response to flow noise excitation is significant. At each frequency, the external loading on the array tube was varied to sample frequency wavenumber space with sufficient resolution to capture the structural response features accurately. The strain response at the fibre laser is captured at each analysis point, which is then converted to equivalent sound pressure level using analytical value of acoustic sensitivity of the

fibre laser hydrophone.

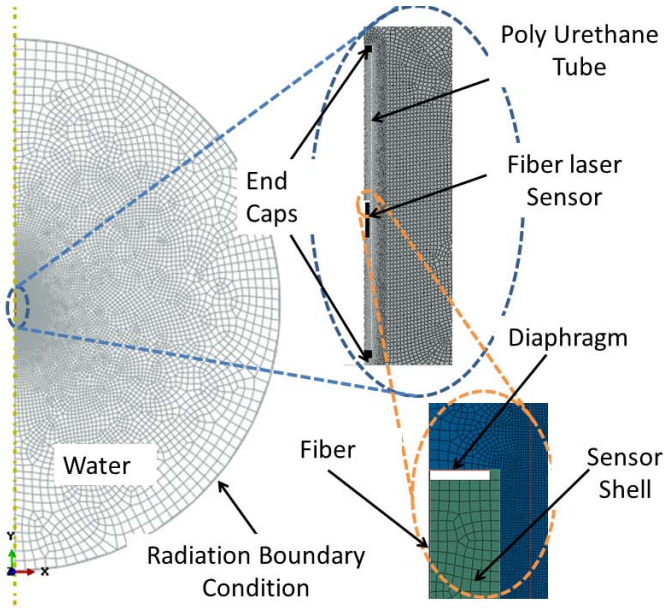

Figure 5.7: FEA Model showing different computational domains

5.4 Results and discussion

The wall pressure spectra given in equation (5.4) is applicable only for cases in which boundary layer thickness $\delta >> a$, the radius of the tube. The momentum thickness (θ) for the fibre laser sensor array configuration was obtained from drag measurements conducted on similar arrays ([100]) following a control volume approach given in reference [101]. Using a conservative assumption of $\delta = 8\theta$ ([102]), the boundary layer thickness for the fibre laser hydrophone has a value greater than 80mm and is significantly larger than the array tube radius. The spectral levels of wall pressure fluctuations depend directly on the skin friction coefficient of the towed array through friction velocity(v_*). The friction velocity value of $0.038U$ is used in equation (5.4) based on skin friction values estimated from drag measurements on thin line arrays [100].

The flow noise power spectral densities were numerically evaluated for different tow speeds ranging from 1 m/s to 8 m/s. Figure 5.8 compares the circumferentially averaged flow noise spectrum at the surface of the array tube with the flow noise spectrum at the centre line of the towed array at different tow velocities. It can be observed that significant reductions in flow noise levels could be achieved by packaging the sensor inside a fluid filled tube.

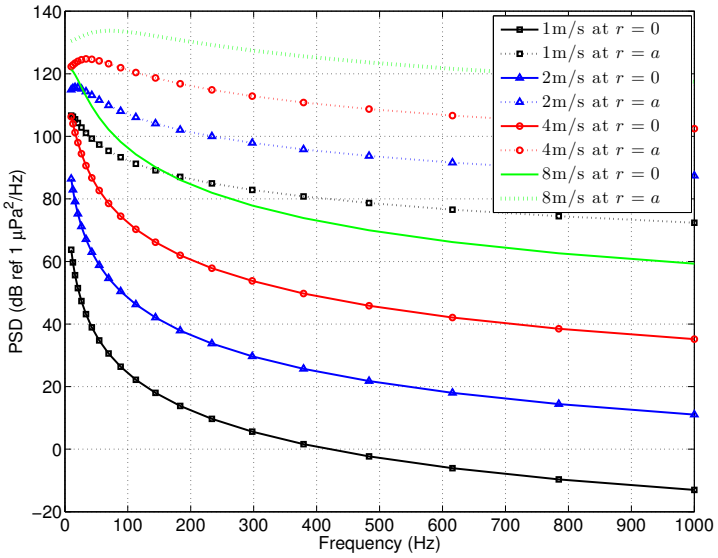

Figure 5.8: Power spectral density of pressure at the surface and at the centre of the towed array tube for different tow velocities. The solid lines correspond to flow noise spectrum at the central line of the array and dotted lines correspond to flow noise spectrum on the surface of the array tube.

The analytical model was also used to examine the variation of the power spectrum of the pressure at the different radial locations inside the array. Variation of the frequency spectrum along the radius of the array scaled by the value at the centre line is given in figure 5.9 for a sample tow velocity of 2 m/s. It can be observed that the variation along the radial direction is negligible as it is mainly controlled by Bessel function amplitudes in equation (5.6). The argument to the Bessel function is very small for the wavenumbers and radius used in the study. In physical terms,

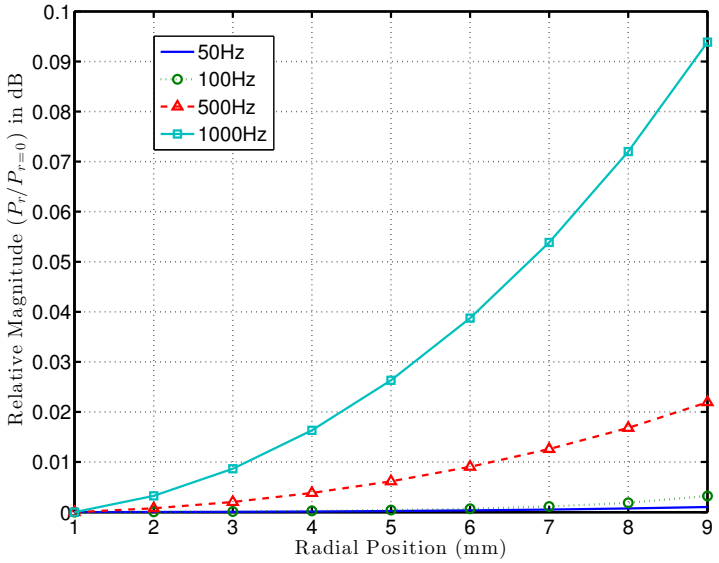

Figure 5.9: Internal pressure spectrum variation with radial location at different frequencies

the internal wavelengths along the radial direction mainly depends on the acoustic velocities of the internal fluid and are much larger in comparison to the array diameter used in the study to result in significant variation in pressure amplitudes along the radius. The variation of internal pressure spectrum with tube diameter for a tow velocity of 2 m/s is shown in figure 5.10. The flow noise spectrum inside the tube was observed to increases with decrease in array tube diameter.

The flow noise response at the fibre laser hydrophone can be calculated from the strain response spectrum ($H_s(k,\omega)$)and frequency wavenumber spectrum of the flow noise on array tube(($P_0(k,\omega)$) using equation (5.11). In equation (5.11), the factor 4π is used to account for conversion from two sided radian frequency measure to Hertz [80]. The obtained flow noise response is then scaled using the sensitivity of the fibre laser hydrophone to represent flow noise in dB ref 1μPa. Thin line arrays used in underwater surveillance application usually consists many individual sensors, which are spaced as per array signal processing requirements. It can have length of

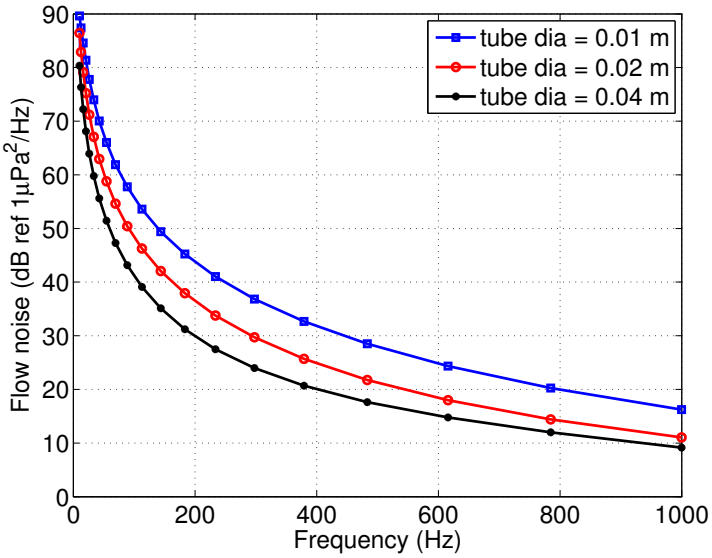

Figure 5.10: Variation in internal pressure spectrum at r=0 for different array diameters for a tow velocity of 2 m/s

the order of a few tens of meters. Key dimensional features of the sensor and the tube used in the analysis is summarised in table 5.2. Modelling the entire array for its response characteristics is computationally prohibitive. Hence a section of the array of 0.2 meter with acoustically hard blocking plugs at both the ends is considered initially to get preliminary estimate of the response characteristics. Figure 5.11 shows the strain response characteristics for the above mentioned array configuration. The flow noise response of the sensor in terms of equivalent acoustic noise (through scaling by the acoustic sensitivity value of 2.9×10^{-9} strain/Pa) is calculated according to equation (5.11). Flow noise estimates for different tow speeds are presented in figure 5.12.

$$\varepsilon(f) = 4\pi \int_{-\infty}^{\infty} P_0(k,\omega) H_s(k,\omega) dk \tag{5.11}$$

Finite element simulations were further extended to study the effect of tube length considered in the analysis. Length of the array section modelled in the analysis was varied from 0.2m to 1.6m. Flow noise estimates

Table 5.2: Dimensions used in the analysis

Feature	Value
Sensor packaging outer diameter	16 mm
Diaphragm diameter	12 mm
Diaphragm thickness	0.3 mm
Sensor length	70 mm
Tube outer diameter	20 mm
Tube thickness	1 mm

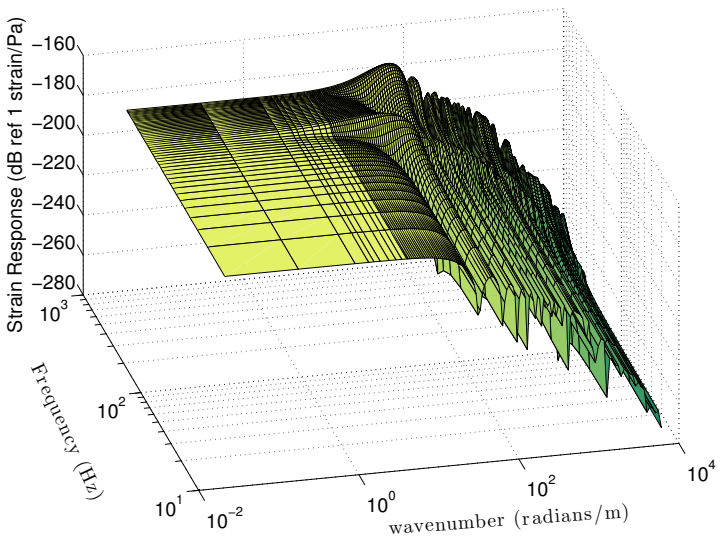

Figure 5.11: Strain response characteristics of the prototype sensor for a tube length of 0.2m

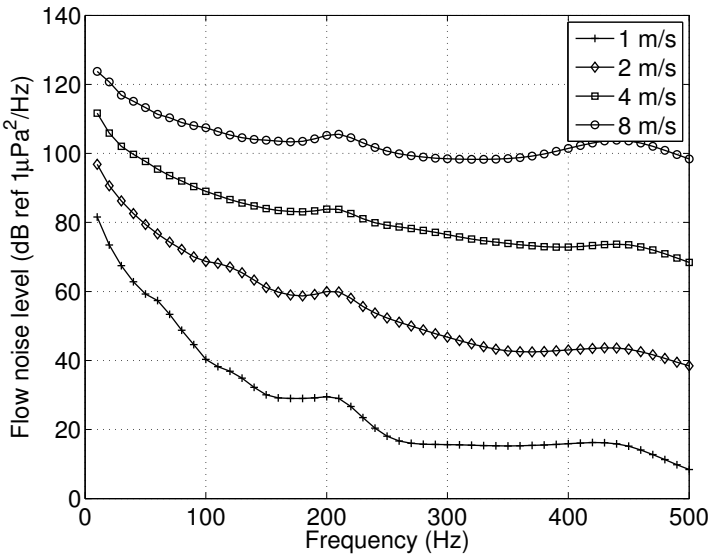

Figure 5.12: Flow noise estimates for a fibre laser hydrophone array with dimensional features given in table 5.2. Tube length = 0.2m

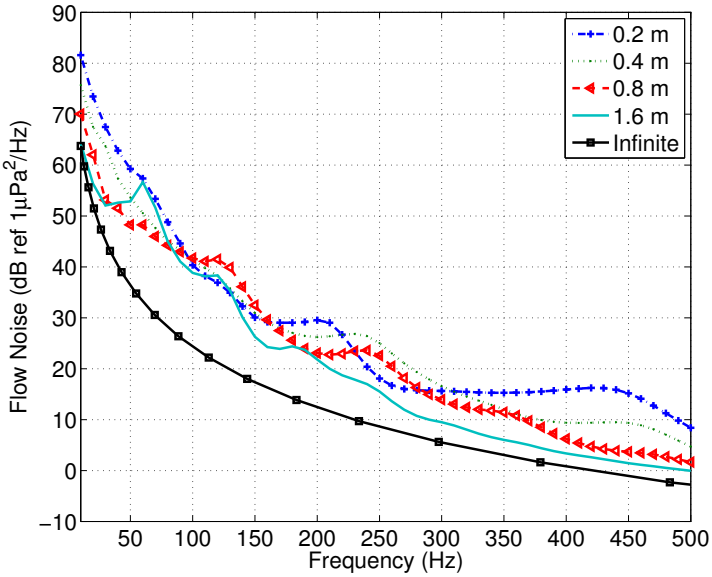

Figure 5.13: Effect of tube length on flow noise response of fibre laser array with dimensional features given in table 5.2 for a tow speed of 1 m/s

were obtained for different tube lengths and they are compared against analytical prediction for centre line pressure spectra using simplified geometry in figure 5.13. As expected, the peak corresponding to the breathing mode moves to lower frequency with increase in the tube length and the flow noise spectra marginally decreases with increase in the tube length. The maximum tube length considered in the analysis corresponds to Nyquist spatial sampling rate for a maximum acoustic frequency of 500 Hz. It is reasonable to assume that thin line arrays for underwater surveillance applications rarely use sensor spacing greater than 1.5 meters. The analytical prediction using the infinite cylinder model is lower than the results obtained using finite element analysis due to difference in tube lengths. The effective sensor dimensions are comparable to the tube diameter and hence results in noticeable changes in dynamic characteristics of the fluid filled array. These changes also partly contribute to this observed difference in predicted values.

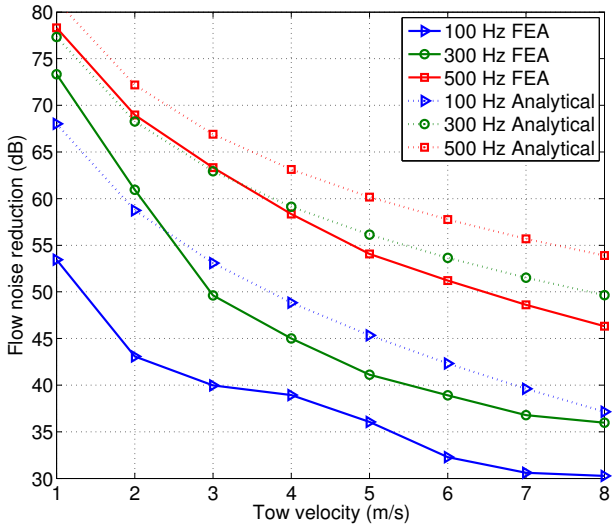

Figure 5.14: Variation in flow noise isolation with tow velocity

Flow noise isolation, defined as the ratio of flow noise spectrum at the surface of the tube to the flow noise spectrum at the array centre line, ob-

tained from analytical model as well as FEA is plotted in figure 5.14. There is a difference in the flow noise isolation levels predicted by analytical model and FEA, nevertheless both approaches predict a similar trend. Although, the fluid filled array configuration is capable of achieving large reduction in flow noise experienced by the sensor, the magnitude of flow noise isolation decreases with increase in tow speed. This arises due to the fact that as the tow speed increases, the wavelengths corresponding to the convective peaks also moves closer to the structural response peak in the wavenumber domain. Hence the amount of isolation to the convective peak significantly reduces with increase in the tow speed as demonstrated in figure 5.15. As the tow speed increases from 2 m/s to 8 m/s, the convective peak moves to a wavenumber region where the sensor packaging has a higher sensitivity leading to a reduction in flow noise isolation.

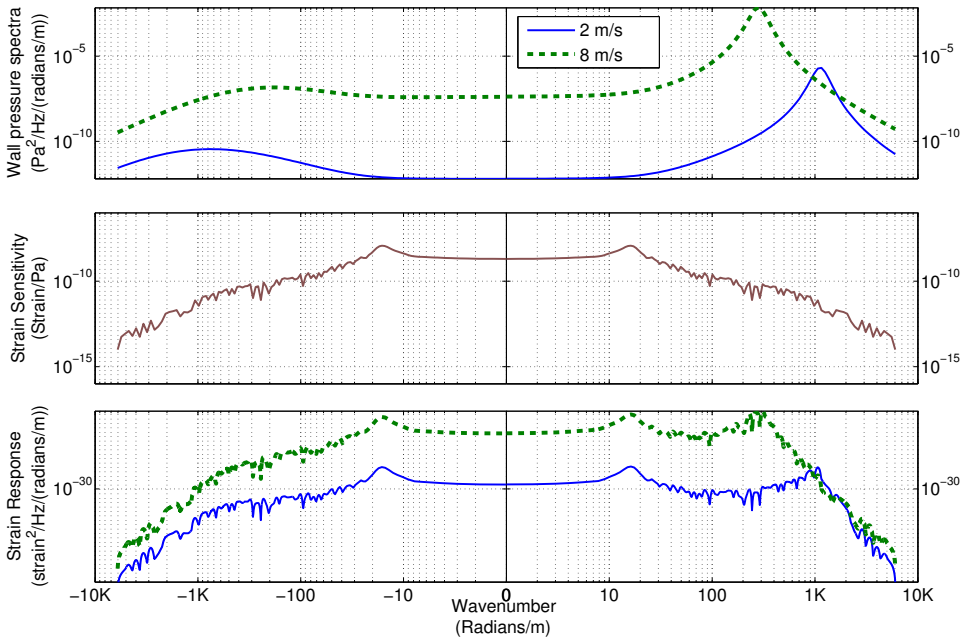

Figure 5.15: Wavenumber distribution of flow noise excitation, sensor transfer function and sensor response at 250 Hz. Top plot shows flow noise excitation on the surface of the cylinder, middle plot shows variation in sensitivity of the sensor array packaging with wavenumber and bottom plot show the flow noise response at the sensor

5.5 Conclusion

The flow noise response of a diaphragm based fibre laser hydrophone array to wall pressure fluctuations in an axisymmetric boundary layer at different tow speeds is presented. Equations for the flow noise levels inside the array tube were obtained by modelling the towed array as an infinite fluid filled tube submerged in water. Improved estimates of flow noise levels for the actual array configuration were then obtained based on the finite element analysis of array sections. Though, significant reduction in flow noise levels can be achieved through fluid filled array configuration, the flow noise isolation decreases with increase in tow speed. The flow noise arising due to turbulent wall pressure fluctuations for the analysed configuration was found to be less than the usual ambient noise levels in the sea for operating speeds below 2 m/s. It was also observed that the variation in flow noise levels corresponding to increase in length of array section in FEA model is only marginal for typical sensor spacings used in thin line arrays used for underwater surveillance applications.

Chapter 6

Performance Characterisation: Experiments

Previous chapters presented the principles behind fibre laser based underwater acoustic sensing and a design configuration to achieve the performance objectives. Many different sensor packaging configurations were tried out during the course of this thesis work to to understand the practical issues of engineering them as well as to evaluate their performance against the requirements discussed earlier. Figure 6.1 shows the pictures of the different configurations.

The simplest among them is a fibre laser packaged inside a water filled acrylic tube as shown in Figure 6.1a. It provides sufficient protection for easy handling. Figure 6.1b shows a configuration in which low modulus poly-urethane moulding is applied on the fibre laser. A teflon shell packaging configuration which tries to enhance the sensitivity through geometrical feature is shown in figure 6.1c. Though, these configurations were able to provide sensitivity improvements, their operational bandwidth with flat frequency response were limited by the presence of mechanical resonances.

Figures 6.1d to f shows metal diaphragm based configurations where

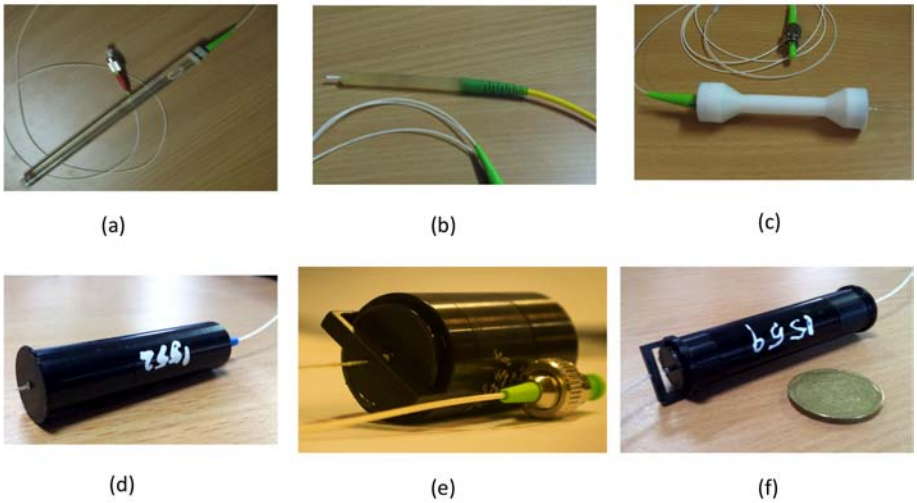

Figure 6.1: Photos various sensor configurations: a) fibre laser packaged in a water filled acrylic tube b) PU moulding c) teflon shell packaging d) metal diaphragm packaging, d) pressure compensated diaphragm based design f) sensor packaging for array construction

6.1d shows a prototype developed to validate the metal diaphragm based sensing scheme and to understand associated practical issues. Figure 6.1 e & f shows the pressure compensated hydrophone configuration discussed in chapter 3 and its modified version for fibre laser hydrophone array construction respectively. This chapter is organised into two main sections; section 6.1 presents the engineering aspects in construction of sensor configurations shown in figure 6.1 e & f. Results of measurements carried out on the fibre laser hydrophone towards its performance characterisation and experimental validation of the analytical model given in chapter 3 is described in section 6.2.

6.1 Engineering considerations

As illustrated by the parametric study on the diaphragm based design presented in chapter 3, there are many dimensional configurations that could achieve the performance objectives. The actual configuration for

sensor construction was chosen based on the engineering considerations. A sensor configuration with small diameter is advantageous, especially for thin line array construction. But, as the diameter decreases, the space available to incorporate the pre-tensioning arrangement also decreases, thus necessitating the use of non-standard design features. Another challenge arises from the fact that, as the diaphragm diameter is reduced, the thickness also need to be reduced to achieve the required sensitivity figure as discussed in subsection 3.4.4. The cross-sectional area of diaphragm chamber and expansion chamber also reduces with the reduction of diaphragm diameter, affecting the performance of the acoustic filter significantly, unless the connecting link diameters are also reduced correspondingly.

Another major consideration is the ease of fabrication and associated cost. Manufacturing the main sensor shell in a single piece will significantly increase the complexity associated with fabrication of of acoustic filter elements. Hence, the main sensor shell was split into multiple-segments to improve the manufacturability. Necessary tolerance specification ensured alignment of holes after the assembly. Any localised bending on the fibre laser due to misalignment can lead to fibre laser output power reduction, and in many cases, these bends can distort the grating structure to stop the lasing action.

Fibre laser is centrally placed inside the sensor shell and bonded to the pre-tensioning arrangement and diaphragm using epoxy. The selection of the bonding compound and application technique also plays a significant role. First of all, the moulding technique should be effective in transferring the diaphragm deformations on to the fibre. A very simplified model of the active sensing region is shown in figure 6.2. The effective stiffness depends on the values of stiffness of diaphragm (K_{dia}), fibre (K_{fibre}), and moulding K_{mould}. The effect of air stiffness K_{air} is very small in comparison with

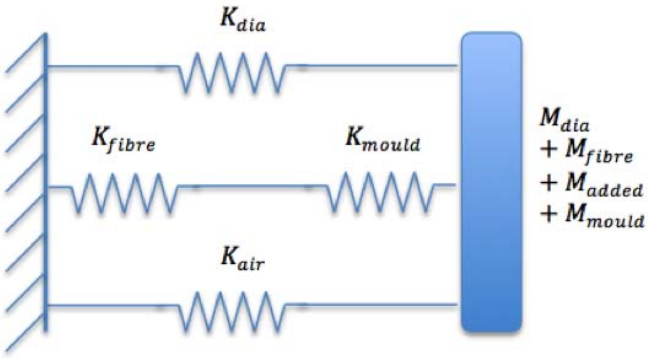

Figure 6.2: Simplified mechanical model of diaphragm-based design

other terms and neglected in analysis. Deformation at the fibre due to a load N can be expressed as in equation (6.1), which suggest that it would be ideal to have $K_{mould} >> K_{fibre}$.

$$\delta_{fibre} = \frac{N}{K_{dia} + K_{fibre} + \dfrac{K_{fibre}K_{dia}}{K_{mould}}} \tag{6.1}$$

It would be advantageous to keep the free length of fibre (the length between the mouldings) to the minimum due to two reasons. Amount of pretension depends on the free length of the fibre and any reduction in this length yields corresponding reduction in the required pretension. Secondly, it improves the sensitivity of the hydrophone as the same deformation of the diaphragm imparts higher strain on a shorter fibre, specifically when the diaphragm stiffness is much larger than the fibre stiffness. The fibre lasers used in the study is fabricated by writing the grating structure on to a rare-earth element doped active fibre. Normal optical fibre is then fusion spliced on both ends of this active element. Moulding of the fibre during the sensor packaging needs special attention due to proximity of the moulding to the fibre splicing points. If proper care is not taken, the moulding can run over the splicing points. This could lead to lower power outputs from

fibre laser as the splice junctions are sensitive to uneven strains introduced during the curing of the moulding compound.

Usually optical fibres are given a protective resin coating to improve its handling properties. These coatings usually consist of a low modulus ultraviolet curable resin and has a significantly low shear strength. Hence this protective coating should be removed to establish direct bonding to the glass fibre.

The depths up-to which pressure compensation arrangement can effectively eliminate the effect of static pressure depends on the maximum achievable compression ratio. As the depth changes, the slider moves inside the slider chamber to compress or expand the air inside the sensor to compensate for the static pressure variation due to changes in operation depth. Maximum compression ratio is achieved when the slider motion uses up the entire slider chamber volume. In the current study, the sensor configuration was designed to provide a compression ratio of up-to 5 with the slider using up the entire volume under an external pressure corresponding to a 50m water depth. The effective volume of the slider chamber necessary to achieve the required compression ratio depends on the volumes of diaphragm chamber and expansion chamber. Thus, it is necessary to minimise the diaphragm chamber volume to minimise the overall size of the sensor. As the diaphragm diameter is selected based on the sensitivity and frequency band requirements, the gap in the diaphragm chamber should be optimised.

As the gap in the diaphragm chamber is very small (of the order of 1mm) special attention is needed to avoid accidentally gluing the diaphragm on the diaphragm chamber walls during the assembly. Thus viscosity, capillary action and the working time of the epoxy play an important role in the realisation of a working sensor. Two different dimensional configurations

as given in figure 6.1 e & f were fabricated for experimental studies. Key features of these two configurations are summarised in table 6.1. Config.A corresponds to the pressure compensated fibre laser hydrophone discussed in chapter 3. Config.B is a modified version of Config.A, where pretensioning arrangement was modified to achieve a thinner sensor. In addition it is provided with features required for proper packaging of these sensors in a polyurethane tube for fluid filled array construction. The dimensional features of Config.B were chosen so as to achieve a frequency response characteristic similar to that of Config.A.

Table 6.1: Comparison of sensor configurations

Feature	Config.A	Config.B
Overall Diameter	20mm	16mm
Overall Length	55mm	70mm
Diaphragm Diameter	7mm	6mm
Diaphragm Thichness	0.35mm	0.3mm
Sensitivity (strain/Pa) [Predicted]	3.4×10^{-9}	2.8×10^{-9}
Resonance Frquency (Hz) [Predicted]	7.2×10^{3}	8.5×10^{3}

6.2 Experimental results

6.2.1 Pressure compensation scheme

The effectiveness of the pressure compensation arrangement was tested through hydrostatic pressure tests. Two different prototypes of sensor Config.A in table 6.1, one with pressure compensation scheme and the other without pressure compensation scheme, were subjected to hydrostatic pressures and corresponding changes in the wavelengths of the fibre laser were measured using an optical spectrum analyser with a wavelength resolution of 0.01nm. Both configurations are same in all aspect expect the fact that connecting link between the slider chamber and diaphragm chamber

is missing in the sensor configuration without pressure compensation. The pressure compensation scheme for the prototype sensor used for the testing provided a compression ratio of up-to 4.9 with the slider using up the entire volume under an external pressure corresponding to approximately 50m of water depth.

The hydrostatic test chamber was fitted with a custom designed bulkhead penetrator with optical connectors. This enabled the sensor operation inside the chamber. A digital pressure gauge was used to measure the hydrostatic pressure while a hand pump flitted with release valve was used for adjusting the pressure inside the test chamber. The penetrator was carefully designed to retain a small air pocket in the region where the optical connectors are placed. This avoided the performance issues related to water ingress into the optical connector. But this arrangement necessitated more wait time before the pressure in the test chamber stabilised due to higher solubility of air in water at higher pressure. The hydrostatic pressure readings and wavelengths were noted once the pressure in the chamber stabilised.

The results are plotted in figure 6.3. The sensor without pressure compensation was tested up-to a depth of 11m and at higher pressures the lasing action stopped intermittently. The sensor with pressure compensation was subjected to hydrostatic pressures corresponding to 100-meter depth though the maximum compression ratio of pressure compensation scheme is expected to provide static pressure compensation only up to 49 meter of water depth. Experimental results showed that the shift in the wavelength of the fibre laser corresponding to the static pressure is negligible for operational depths up to about 43 meters, which is approximately 6 meter lower than the theoretically value. A mismatch between the slider chamber volume accounted for in the computation and the actual volume

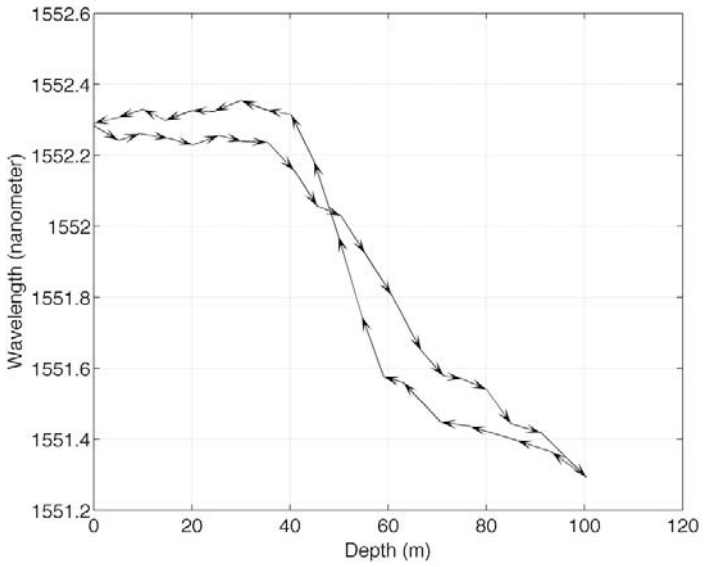

(a)

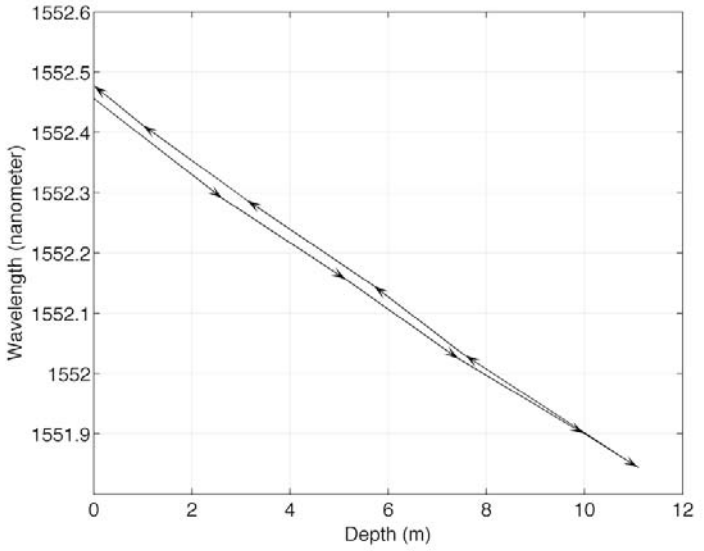

(b)

Figure 6.3: Experimental results from hydrostatic testing. (a) shows the variation of fibre laser wavelength with hydrostatic pressure for a pressure compensated sensor prototype and (b) shows the similar results for a prototype sensor without pressure compensation.

could be one of its the possible causes. Manufacturing errors, observed during the assembly of the sensor is believed to be another contributor to this deviation. Slider motion was not very smooth over the end section of slider chamber, resulting in increased friction at these points. In addition, the air volumes in the O-ring grooves of the slider and little extra free space getting generated in the side chamber due to the chamfer provided on the slider etc. are not considered in the calculation. Depending on the functional requirements, operating range of the pressure compensation scheme can be further increased by providing additional volume in the slider chamber. Further optimisation of diaphragm chamber volume could also lead to improvements in the operating range of static pressure compensation scheme.

The effects of friction at the O-ring sealing between the slider and the slider chamber walls could be observed in the test results. Stick-slip friction at the O-rings is possibly the main contributor to the wavy nature of wavelength variations with external hydrostatic pressure. The difference in the wavelengths between pressure increase and pressure decrease for the depth range 0-40 meter is also partially linked to the friction effects. Static friction effects produce a small pressure difference between side chamber pressure and external hydrostatic pressure. When the external hydrostatic pressure is increased, the air chamber pressure will be slightly lower than the external pressure and vice versa when the external hydrostatic pressure is decreased. This small pressure difference will result in corresponding wavelength changes on fibre laser output. The stick-slip friction at the O-ring sealing in the chamber is possibly the main contributor to the wavy nature in the wavelength variations with external hydrostatic pressure.

The hydrostatic pressure has negligible effect on the acoustic sensitivity of the pressure compensated hydrophone as the effective stiffness contribu-

tion from the air in the chambers of the sensor is insignificant compared to the total stiffness of the active sensing area. In addition, the acoustic impedance of the air is much lower than that of water. Even when the sensor operates at 50m water depths, the acoustic impedance of water is more than 700 times higher than that of air. Figure 6.4 compares the predicted sensitivity performance of the sensor at 1 m depth and 50 m depth.

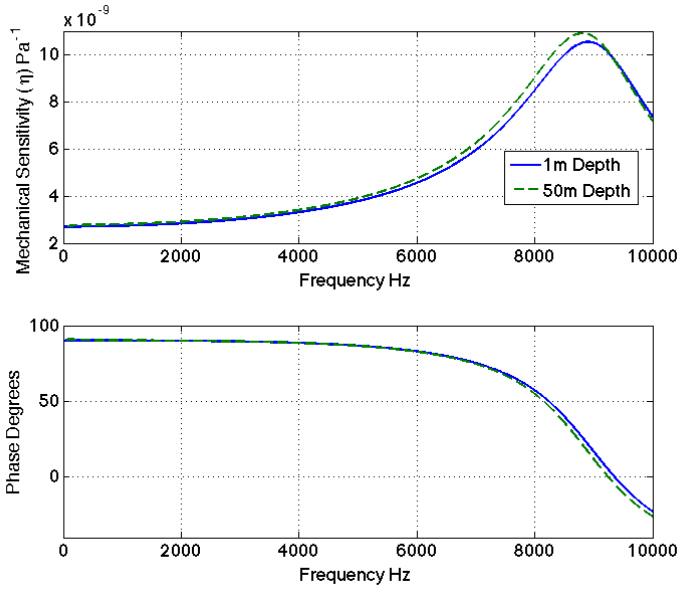

Figure 6.4: Effect of hydrostatic pressure on acoustic sensitivity of the pressure compensated fibre laser hydrophone

6.2.2 Acoustic test

The schematic of the experimental set up, used to evaluate the acoustic characteristic of the DFB-FL hydrophone, is shown in figure 6.5 and a picture of measurement instrumentation is shown in figure 6.6. A Mach Zehnder interferometer, configured with 1m path imbalance and a peizoceramic fibre stretcher, was used in the measurement. The phase demodulator, OPD4000 from Optiphase®, employed a phase generated carrier (PGC) demodulation technique as detailed in the reference [76]. Sensitivity of the pressure compensated fibre laser hydrophone in the frequency

range 1-10kHz were evaluated in a 2m × 2m × 2m acoustic tank using signal pulses at each frequency to eliminate the effect of acoustic modes of the tank on the measurement results. The low frequency measurement limit was imposed by the tank size as well as the low transmitting voltage response (TVR) of the transmitter. Test signals were amplified and then transmitted using B&K 8105 acoustic transducer.

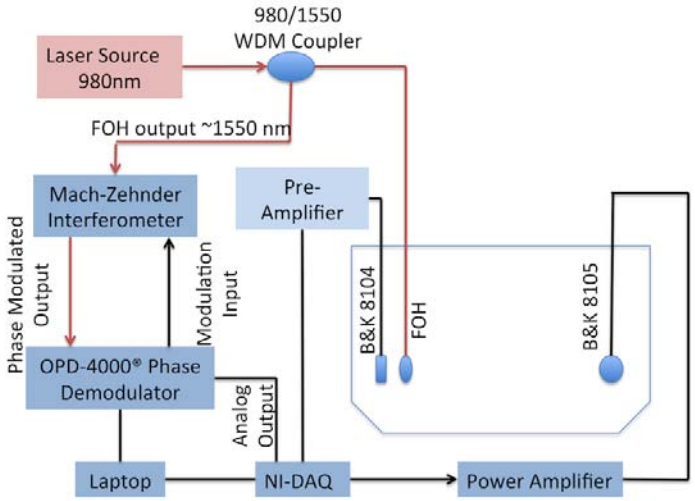

Figure 6.5: Lab measurement configuration: Schematic

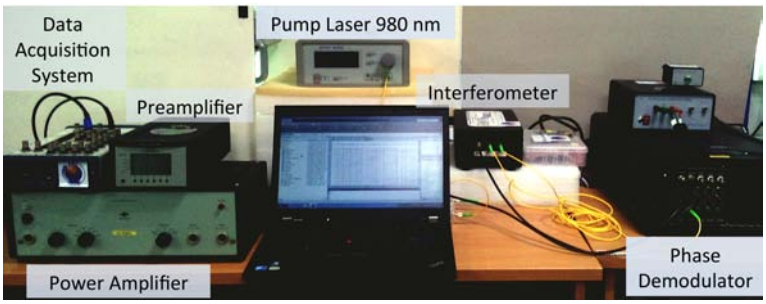

Figure 6.6: Lab measurement configuration: Instrumentation

The sensitivity of the FLH was measured by comparing the output of FLH system with the output from a reference hydrophone (B&K 8104). Nexus preamplifier was used to amplify the signals coming from the reference hydrophone. A preamplifier gain of 45 dB resulted in a voltage sensitivity of -160 dB ref 1V/μPa for the reference hydrophone which has

a flat frequency response with in ±2 dB in 1Hz-10kHz. All the transducers were placed at a depth of 1 m which corresponds to mid-depth point of the acoustic tank used in the measurement. The sensors were placed in the tank such that it will results in maximum time delay between direct and reflected arrivals of the transmitted signals at the FLH and reference hydrophone. NI-6251 data acquisition system from National Instruments was used for digitising the data and the whole measurement and analysis were carried out under Matlab®environment. The received signals were then band pass filtered around the transmission frequency before picking amplitude values for the estimation of the sensor sensitivity.

Figure 6.7 shows the comparison of the signal received by the reference hydrophone and FLH for a transmission at 3300Hz. At 3300 Hz the wavelength is 0.45 m. Thus two cycles at 3300Hz was used to avoid the interference with reflections from the wall. The red squares in figure 6.7 shows the amplitudes picked for estimation of sensitivity. This procedure was repeated 10 times at each test frequency.

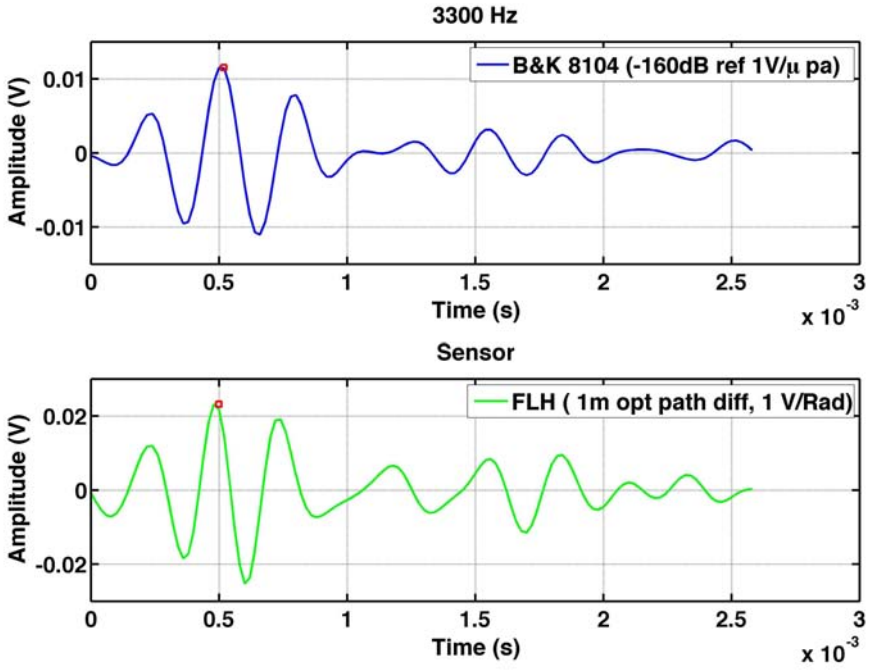

Figure 6.7: Band pass filtered output from reference hydrophone and FLH

Figure 6.8 shows the comparison between the experimental results with the simulation results obtained from simplified theoretical model. For the direct comparison, the strain response values obtained from theoretical model were converted into Radians/μPa units through the application of equations (3.1a) and (3.28). The error bars on the experimental results show the range of sensitivity values observed in a set of 10 measurements at each test frequency. The median value was used in creating the trend curve. For sensor config.A, measurements from three different sensors were given and sensitivity values were found to vary between the sensors. This variation could be due to small variations in diaphragm dimensions and inaccuracies in the moulding the diaphragm on to the sensor shell. The measurement repeatability improved at higher frequencies due to better SNR provided by the transmitter at those frequencies. Variations in the sensitivity across the measurements at low frequencies are attributed to the lower transmitter efficiency at low frequencies and also due to the smaller size of the tank in which measurements were carried out. The experimental results compared reasonably well with the analytical results. The prototype FLH-2 showed a slightly higher natural frequency and lower sensitivity compared to the theoretically predicted results. One possible source for this difference could be the small reduction in effective diameter of the diaphragm arising due to the epoxy moulding at the diaphragm chamber − diaphragm interface. The differences in material properties used in the analysis from the actual values also could have contributed to these small deviations from the predicted results.

Figure 6.9 shows similar results for config.B and it is marked as Meas 1, The results obtained using half sine pulse excitation in the frequency range 2-7kHz is also presented in the same figure for direct comparison. The coherence between the reference sensor and fibre laser hydrophone were

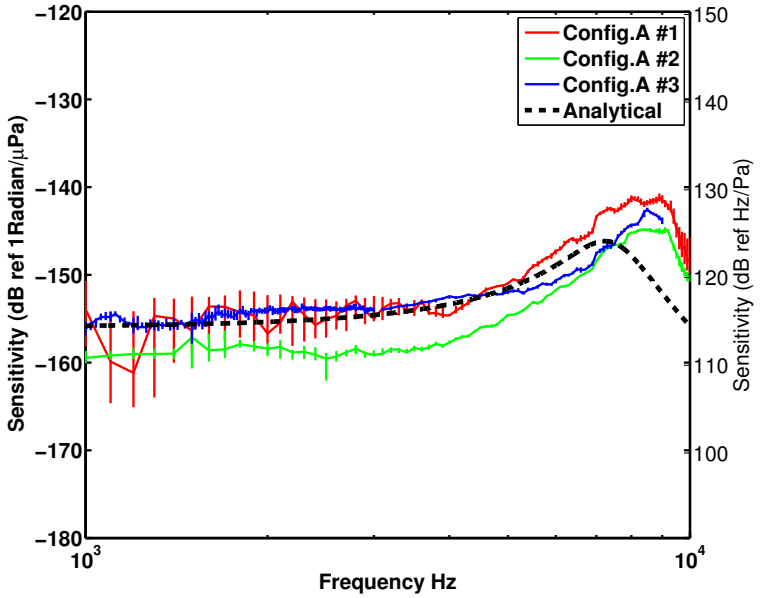

Figure 6.8: Comparison of measured and simulated hydrophone sensitivity for config.A

very low outside this measurement range. The half sine pulse measurements were carried out in an acoustic tank of size 50 $m \times 20\ m \times 18\ m$ and the sensors were placed at a depth of 5 meter. A good agreement can be observed between measured and predicted results.

Figure 6.10 shows the direct comparison among the sensitivity results for config.A obtained through analytical model, finite element analysis and experiments.

Figure 6.11 shows the comparison of performance of the fibre laser hydrophone with that of reference hydrophone (B&K 8104) with Nexus preamplifer set to have an effective sensitivity of -160 dB ref 1V/μPa. Both the FLH and B&K 8104 were placed at 1 meter distance from the source transmitting 3kHz test signal. The output of the FLH was scaled to align the peaks corresponding to the 3kHz test signal. It can be observed that the output from the fibre laser hydrophone closely follows the results obtained from reference hydrophone. While the effect of power supply frequency and its harmonics are predominant in reference hydrophone, its effect are

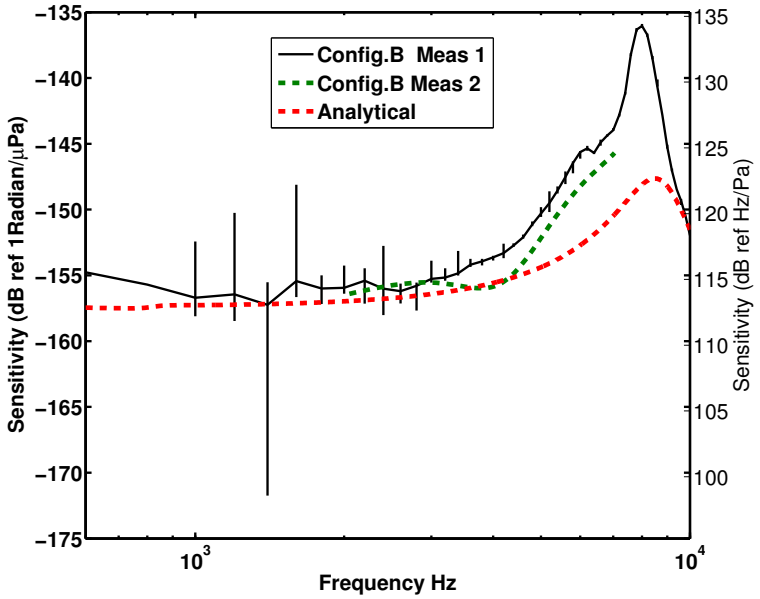

Figure 6.9: Comparison of measured and simulated hydrophone sensitivity for config.B; Meas 2 corresponds to measurement carried out using pulse excitation

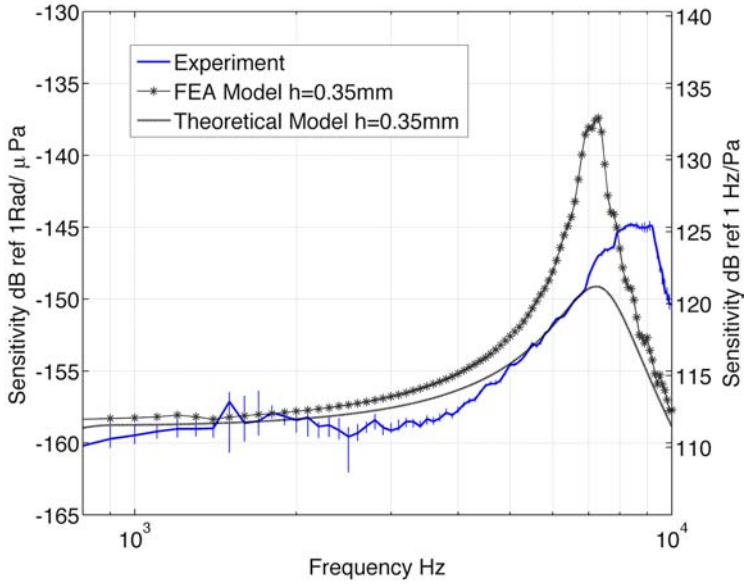

Figure 6.10: Comparison of sensitivity results from analytical model, FEA, and experiment for config.A

significantly lower in the fibre laser hydrophone measurements. The second and third harmonics of the test signal, although of very small magnitude, can be observed in FLH and reference hydrophone at 6 kHz and 9 kHz respectively. It can be observed that distortion signals at harmonics have higher amplitudes compared to the reference hydrophone. This arises due to higher sensitivity of fibre laser hydrophone at these frequencies. The small signal around 8kHz is of unknown source associated with tank measurement set-up.

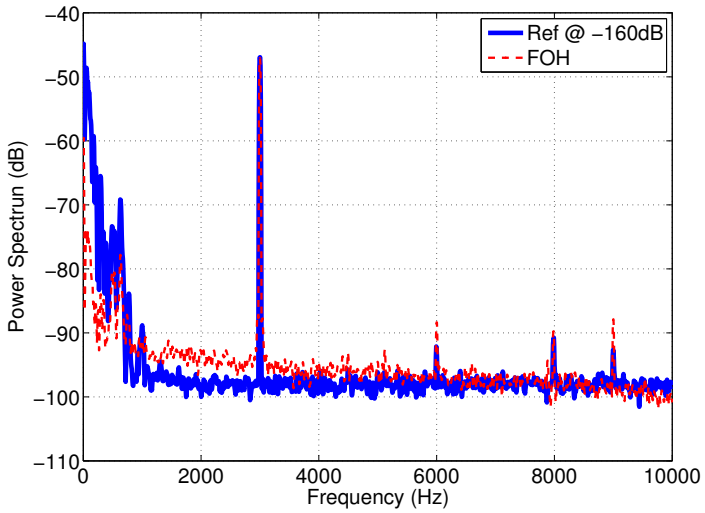

Figure 6.11: Performance comparison between fibre laser hydrophone and B&K 8104. Power spectrum of the outputs from both sensors for a continuous transmission at 3kHz is sown

Figure 6.12 shows the comparison of voltage sensitivity performance of the fibre laser hydrophone (1 m optical path difference in the interferometer and 1 V/Radian gain setting on the demodulator) with that of reference hydrophone (B&K 8104 with a preamplifier gain of 45dB) with Nexus preamplifer set to have an effective sensitivity of -160 dB ref 1V/μPa.

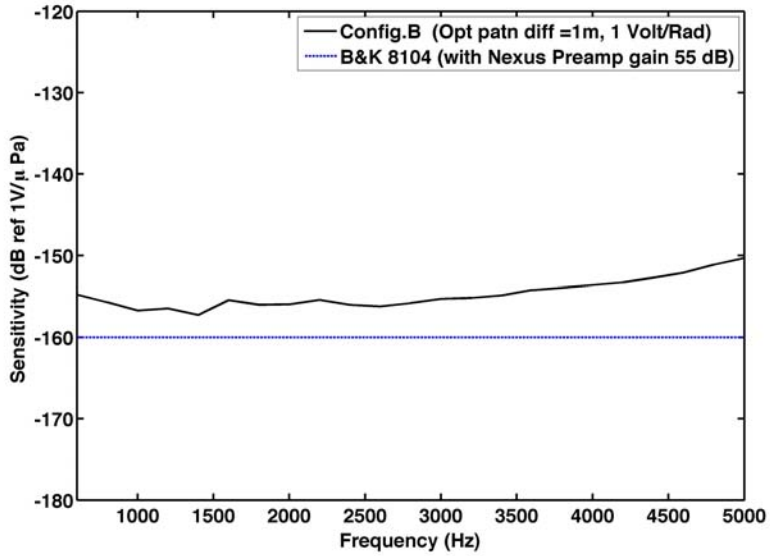

Figure 6.12: Performance comparison between fibre laser hydrophone and B&K 8104

6.2.3 Noise floor

The acoustic noise floor of the sensor system depends on four major parameters which are optical noise floor, optical path difference used in the interferometer, electronic noise floor of the demodulator, and mechanical sensitivity of fibre laser hydrophone packaging. The optical noise floor of the fibre laser is the most important among them as other contributing factors could be controlled to suit the measurement configuration. The optical noise floor is primarily decided by inherent frequent noise of the fibre laser [60]. This frequency noise depends on the properties of the materials and techniques used in the fabrication of fibre laser and is not affected by the packaging scheme used in the construction of the sensor [103].

The noise floor of the fibre laser hydrophones are usually represented in terms of noise equivalent pressure (NEP), which is the frequency noise scaled by the sensitivity of fibre laser hydrophone to express frequency noise level in terms of pressure spectrum level. This helps in direct comparison with ambient acoustic noise data [49]. As the equivalent pressure level

corresponding to the optical noise floor scales with mechanical sensitivity of sensor packaging, any improvements in mechanical sensitivity will lead to corresponding reduction in noise floor of the sensor in terms of equivalent pressure levels. Thus the NEP of the sensor packaging scheme proposed in this thesis mainly depends on the frequency noise.

The frequency noise of the fibre laser can be measured using a configuration similar to the one used for acoustic measurement. The fibre laser is isolated from all external excitations and an interferometer with large optical path difference is used to amplify the frequency noise from the fibre laser. The fibre laser was packaged in a water filled acrylic tube and this configuration has very low acoustic sensitivity. The acoustic sensitivity of a UV curable resin coated fibre laser packaged in a water filled acrylic tube is of the order of -200 dB ref 1Rad/μPa for an optical path difference of 1m (70dB ref 1Hz/Pa). Frequency variations produced in this sensor configuration due to normal sound pressure level of 40 dB ref 20μPa in air is at least 20 dB lower than the inherent frequency noises expected in DFB fibre lasers. An optical path difference of 50 m was used in the interferometer whereas 2 m optical path difference was sufficient to bring the optical noise floor above the electronic noise floor of the demodulator ($3\mu\text{Radians}/\sqrt{\text{Hz}}$) employed in the experiment. This ensures that fibre laser frequency noise is much higher than the electronic noise floor of the opto-electronics instrumentation.

Fibre lasers from two different batches were used in the construction of the sensors. The first batch obtained in year 2011 has relatively lower frequency noise compared to the latest batch procured in 2012. The NEP for the sensor configuration using fibre lasers from two different batches are shown in figure 6.13. Fibre lasers which gave lowest frequency noise levels were used for the comparison. Figure 6.13 also plots the NEP for

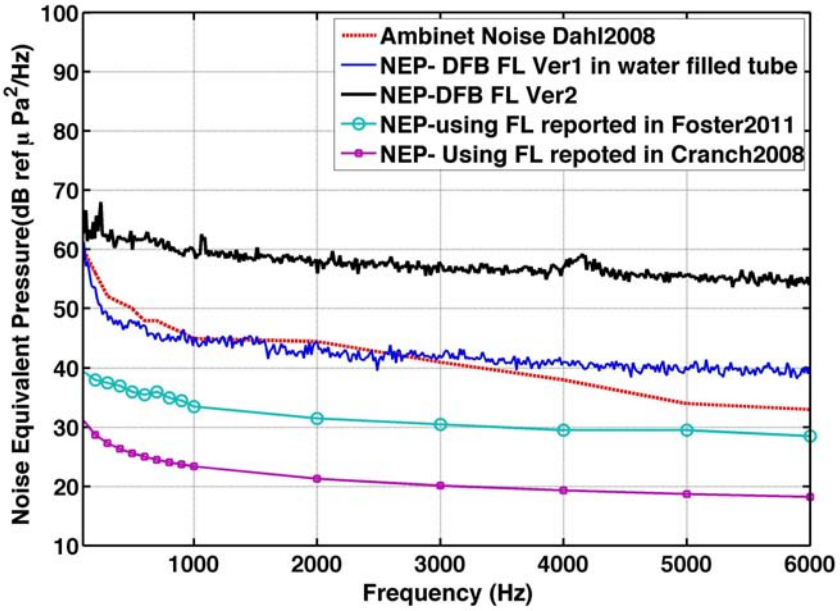

Figure 6.13: Comparison of noise equivalent pressure spectral density (NEP) with ambient noise spectral density for sea state zero

the proposed sensor configuration using fibre lasers with better frequency noises as reported in [49, 60]. The ambient noise spectrum for a sea state zero reported by Dahl et al. [59] is plotted in figure 6.13 for direct comparison. It can be observed that by using fibre lasers with better frequency noise than currently employed in sensor construction, the proposed sensor configuration can achieve better than sea state zero noise floor.

6.2.4 Acceleration sensitivity

The acceleration sensitivity of the fibre laser hydrophone was measured in air by vibration testing . The prototype sensor was mounted on a vibration shaker and subjected to random vibrations in frequency range 50Hz-10Khz. The acceleration sensitivity values were obtained by comparing fibre laser hydrophone output with the measurements from a calibrated reference accelerometer mounted on the vibration fixture. Figure 6.14 shows the experimental setup used for the vibration testing. A digital signal analyser generates the excitation signal which is amplified by a power amplifier

before it is applied to the vibration exciter. The signal outputs from FLH and reference accelerometer are fed back to the digital signal analyser for estimation of acceleration sensitivity.

The noise rejection figure [49], defined as the ratio of the pressure sensitivity to acceleration sensitivity, was also calculated by scaling the acceleration sensitivity values using the pressure sensitivity in the frequency range 0-5kHz. The sensor has an average noise rejection figure greater than 0 dB ref $1m/s^2/Pa$ in the frequency range of interest. Figure 6.15 shows the acceleration sensitivity and acceleration rejection figure for the prototype sensor for vibration excitation along and normal to the axis of the sensor. The prototype sensor's acceleration rejection figure is of the same order of magnitude as the results reported by Foster et al. [49] on micro-engineered silicon crystal fibre laser hydrophone.

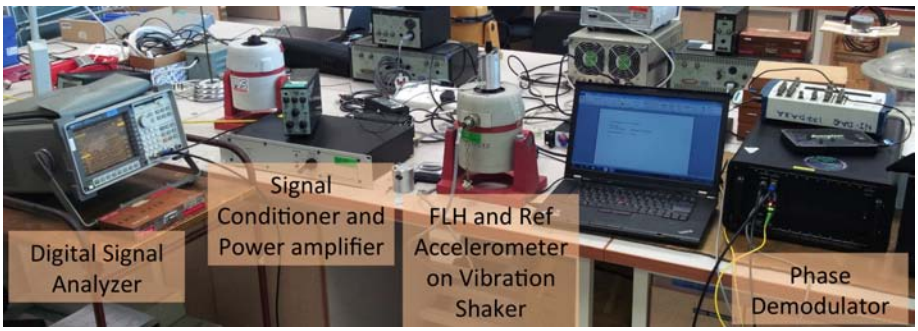

Figure 6.14: Experimental setup used in the measurement of Acceleration sensitivity along and normal to the axis of the sensor

6.2.5 Temperature sensitivity

As fibre laser output wavelength is sensitive to temperature changes, it is important to characterise the variation in sensor wavelength with temperature. The relation between the Bragg wavelength and parameter of the fibre Bragg reflectors written to create the fibre laser is given in equation (6.2) where n_{eff} is the effective refractive index and Λ_B is the grating

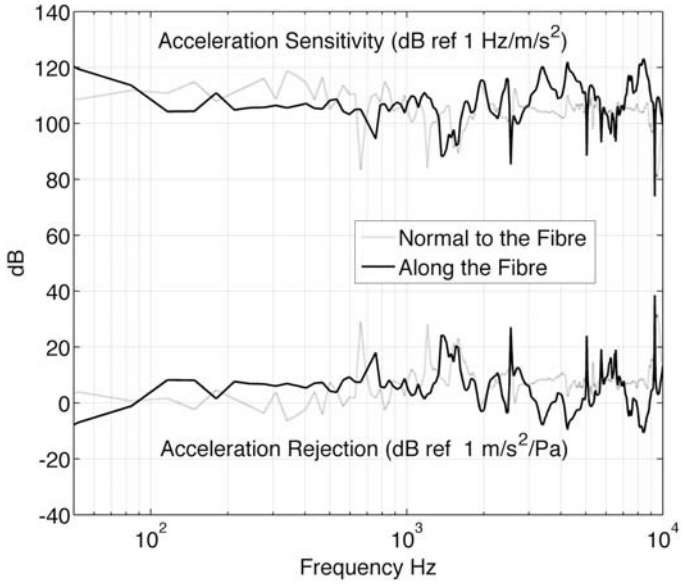

Figure 6.15: Acceleration sensitivity and acceleration rejection along and normal to the axis of the sensor

pitch. [104]

$$\lambda_B = 2n_{eff}\Lambda_B \tag{6.2}$$

Differentiating equation (6.2) with respect to temperature yields

$$\frac{1}{\lambda_B}\frac{\mathrm{d}\lambda_B}{\mathrm{d}T} = \frac{1}{\Lambda_B}\frac{\mathrm{d}\Lambda_B}{\mathrm{d}T} + \frac{1}{n_{eff}}\frac{\mathrm{d}n_{eff}}{\mathrm{d}T}. \tag{6.3}$$

In equation (6.3), first term corresponds to thermal expansion of silica fibre and second term is the thermo-optic coefficient. While the thermo optic coefficient for a normal fibre has a value in the range $3.5-7\times10^{-6}$ °C^{-1}, the magnitude of thermal expansion coefficient is only 5×10^{-7} °C^{-1} which is an order less than the thermo-optic effect(pp.83 ref [105]). Typical values of the temperature sensitivity of Bragg wavelength in literature is summarised is table 6.2.

In order to measure the temperature sensitivity of the pressure compensated diaphragm based fibre laser hydrophone to temperature variation,

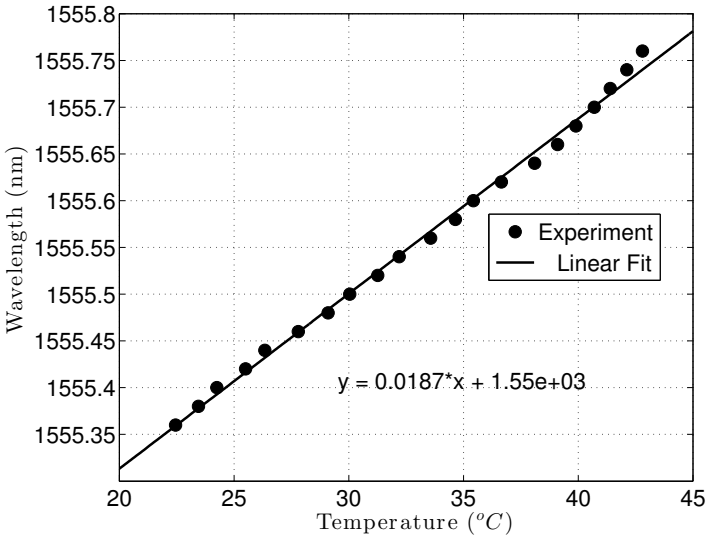

Figure 6.16: Variation of fibre laser wavelength with temperature

Table 6.2: Temperature sensitivity

Source	Wavelenth (nm)	Temp. Sensitivity ($nm^{\circ}\mathrm{C}^{-1}$)
Rao [106]	1550	0.013
Morey [107]	800	0.007
Launay [108]	1550	0.012

prototype sensor is immersed in a hot water bath and is allowed cool to room temperature from 45°C. The wavelength of the fibre laser output is then monitored using an optical spectrum analyser with spectral resolution of 0.02nm. Figure 6.16 shows the variation of fibre laser wavelength with temperature. As it could be seen from the figure that the temperature sensitivity of the sensor has a value of 0.0187 nm°C^{-1} and is higher than that of bare fibre lasers and Bragg gratings listed in table 6.2. This could be due to the fact that Aluminium used in fabricating the sensor shell has a thermal expansion coefficient of 2.3×10^{-5}°C^{-1} and this value is significantly higher than the value corresponding to silica glass. Nevertheless, the wavelength variation observed due to corresponding variation in temperature is too small to affect the performance of an individual sensor or the multiplexing characteristics of the sensor when used in an array.

6.3 Sensor Specifications

The detailed specifications of the final sensor configuration are summarised in table 6.3.

Table 6.3: Sensor specifications

Parameter	Value
Acoustic Sensitivity	-112 ±2 dB ref 1Hz/Pa -150 ±2 dB ref 1Rad/μPa, 2 m path difference in interferometer
Frequency range	20 Hz - 5kHz
Maximum safe operating depth	50 m
Acceleration rejection	Better than 0 dB ref $1m/s^2/Pa$
Temperature Sensitivity	0.0187 nm°C^{-1}
Sensor noise floor (Noise equivalent pressure)	$<$ 45 dB ref 1μPa[1] at 1kHz
Dynamic range	$>$100 dB
Sensor dimensions	
Overall length	70 mm
Overall diameter	16 mm
Diaphragm diameter	12 mm
Diaphragm Thickness	0.3 mm

6.4 Conclusion

The performance of the pressure compensation scheme for the laser hydrophone was validated through hydrostatic testing. The pressure compensated fibre laser hydrophone showed negligible variation in the wavelength with static pressure for operational depths up to 40 meters, which could be further improved by increasing the slider chamber volume of the proposed fibre laser hydrophone encapsulation. Temperature sensitivity mea-

[1]when used with a fibre laser with frequency noise $<$ 60 Hz/$\sqrt{Hz}$ and an electronic instrumentation where the electrical noise floor is of the order of 3μV/$\sqrt{Hz}$

surements for the sensor indicate that variation in fibre laser wavelengths are not significant enough to cause any issues with wavelength division multiplexing schemes for normal operating temperatures in the sea. The acceleration sensitivity measurements in air showed that the sensor has an acceleration rejection figure of 0 dB ref m/s^2Pa. The sensitivity values of the prototype sensors were experimentally obtained through acoustic pulse testing. The experimental results appear to be in good agreement with the predictions from the analytical model.

Chapter 7

Conclusions & Further Research

7.1 Conclusion

Fibre laser based sensing offers an attractive alternative to conventional piezo-ceramic based hydrophones for thin-line towed array applications. This thesis presented the major design considerations in the development of a fibre laser hydrophones and the challenges in achieving the performance objectives. A novel metal diaphragm based pressure compensated packaging scheme is proposed to achieve the performance objectives. A simplified analytical model for diaphragm based sensing was developed and validated through finite element analysis and experiments.

Distortion characteristics of widely cited demodulation schemes were studied in the context of fibre laser based sensing. In contrast to the analytical predictions, the distortion ratios of PGC-arctangent schemes were found to vary with frequency of the signal with higher distortion figure compared to analytical estimates even under ideal operating conditions. PGC-optiphase algorithm, in which quadrature components of the phase change signals were estimated directly from the interferometer output without the application of low-pass filter, was found to give better distortion

free performance over wide frequency and amplitude ranges.

Equations for the flow noise levels inside the array tube were obtained by modelling the towed array as an infinite fluid filled tube submerged in water. Improved estimates of flow noise levels for the actual array configuration were then obtained based on the finite element analysis of array sections. Though significant reduction in flow noise levels can be achieved through fluid filled array configuration, the flow noise isolation decreases with increase in tow speed. The flow noise arising due to turbulent wall pressure fluctuations for the analysed configuration was found to be less than the usual ambient noise levels in the sea for operating speeds below 2 m/s. It was also observed that the variation in flow noise levels corresponding to increase in length of array section in FEA model is only marginal for typical sensor spacings used in thin line arrays for underwater surveillance applications.

Experiments were carried out to validate the sensor's susceptibility to non-acoustic external excitations like static pressure, acceleration, and temperature variation. The pressure compensated fibre laser hydrophone showed negligible variation in the wavelength with static pressure for operational depths up to 40 meters, which could be further improved by increasing the slider chamber volume of the proposed fibre laser hydrophone encapsulation. The sensor has an acceleration rejection figure of 0 dB ref $1 m/s^2 Pa$ which is comparable to the best values reported in the literature. Though the temperature sensitivity figure of the present configuration is slightly higher compared to a bare fibre laser, variation in fibre laser wavelengths is not significant enough to cause any issues with wavelength division multiplexing schemes or sensor performance for normal operating temperatures in the sea. In summary, this thesis brought out the realisation of a high performance miniature fibre laser hydrophone for thin-line

towed array application.

7.2 Future work

Although, the current sensor configuration compensates for the static pressure, additional arrangements are required in conventional liquid filled array construction to account for the effective volume changes inside the array at higher depths. In general, fibre optic sensors are not prone to water leakage into the array due to the absence of wet-end electronics. Hence, a free flooded array construction and associated engineering may be an area of much practical interest. To extend the performance of the proposed configuration, one can consider the application of high performance materials in construction of active sensing portion of the sensor. Other innovative techniques and mechanisms that allow strain sensitivity enhancements without affecting sensor's frequency response characteristics can also be explored.

Inherent frequency noise is one of the major parameters that limit the performance of the fibre laser hydrophones. The frequency noise of the fibre lasers used in the current study is higher than the values reported in the literature. This high noise floor has essentially necessitated the sensor to be more compliant resulting in reduction in operational bandwidth of the sensor. The performance of the sensor could be further improved and a more compact sensor can be realised if a fibre laser with lower noise is employed in sensor construction. A low noise fibre laser will also open the possibility of using fill materials inside the sensor chambers. Preliminary simulation studies have shown that filling the sensor with liquids (with lower acoustic impedance than water) can result in a more compact sensor but at the cost of acoustic sensitivity. Liquid filled sensor construction can

also extend the safe operational depths to a few 1000 meters.

While hydrophones are capable of measuring the local pressure information of acoustic field, any additional information on the direction of the acoustic field is of significance in array signal processing. Fibre laser based acoustic vector sensor is a natural extension of the current work.

Computational complexity of frequency wavenumber estimate from FEA increases substantially when a sensor configuration requires 3D analysis for accurate response calculations. The mesh density required for the analysis directly depends on the wavenumber domain that needs to be modelled. Hence dividing the problem into different frequency bands as in conventional acoustic analysis would not lead to corresponding reduction in computational size of the problem. Thus the development of a computationally efficient analysis technique for flow noise estimation is another area for further research.

Flow noise studies presented in this thesis used an axisymmetric model to arrive at the flow noise estimates for fibre laser hydrophones. Most of the results on turbulent wall pressure spectra and models are based on flow over flat plates. The axisymmetric estimates are usually derived through integration over a wavenumber range around each feasible circumferential wave number associated with the cylindrical geometry. But better techniques are necessary, especially when the sensors are placed off the axis of the array. Analysis become more complicated when the cylinder is not perfectly aligned along the flow[1]. Development of better flow noise models for cylindrical boundary layer and validation of existing models for cylinders is still an open problem.

The work presented in thesis can be extended through experimental validation of flow noise estimates. Self noise in normal water tunnel fa-

[1]In towed arrays, this scenario can arise due to deviation from neutral buoyancy, array dynamics and cross flows.

cilities often preclude their application in flow noise measurements. One of the most common approach is to tow the sensor array in quiet lakes or reservoirs. The main challenge in flow noise testing is to realise a towing arrangement that can achieve the required tow speed without affecting the ambient noise floor of the lake.

Bibliography

[1] M. J. Hamilton, S. Kemna, and D. Hughes, "Antisubmarine warfare applications for autonomous underwater vehicles: the glint09 sea trial results," *Journal of Field Robotics*, vol. 27, no. 6, pp. 890–902, 2010.

[2] A. Maguer, R. Dymond, M. Mazzi, S. Biagini, S. Fioravanti, and P. Guerrini, "Slita: A new slim towed array for auv applications," in *Proceedings of Acoustics08*, pp. 142–146, 2008.

[3] V. Pallayil, M. Chitre, and P. Deshpande, "A digital thin line towed array for small autonomous underwater platforms," in *Oceans2007*, pp. 1–9, IEEE OES, 1-9 October 2007 2007.

[4] C. K. Kirkendall and A. Dandridge, "Overview of high performance fibre-optic sensing," *Journal of Physics D: Applied Physics*, vol. 37, no. 18, 2004.

[5] J. W. Berthold, "Historical review of microbend fiber-optic sensors," *Journal of Lightwave Technology*, vol. 13, no. 7, pp. 1193–1199, 1995.

[6] K. Grattan and T. Sun, "Fiber optic sensor technology: an overview," *Sensors and Actuators A: Physical*, vol. 82, no. 1-3, pp. 40–61, 2000.

[7] B. Lee, "Review of the present status of optical fiber sensors," *Optical Fiber Technology*, vol. 9, no. 2, pp. 57–79, 2003.

[8] A. D. Kersey, "Recent progress in interferometric fiber sensor technology," in *Proceedings of SPIE Vol.1367* (R. P. DePaula and E. Udd, eds.), pp. 2–12, 1991.

[9] C. R. Batchellor and C. Edge, "Some recent advances in fibre-optic sensors," *Electronics & Communication Engineering Journal*, vol. 2, no. 5, pp. 175–184, 1990.

[10] K. Annamdas and V. Annamdas, "Review on developments in fiber optical sensors and applications," in *Proc. SPIE vol.7677*, pp. 76770R–76770R12, 2010.

[11] J. N. Fields, C. K. Asawa, O. G. Ramer, and M. K. Barnoski, "Fiber optic pressure sensor," *The Journal of the Acoustical Society of America*, vol. 67, no. 3, pp. 816–818, 1980.

[12] N. Lagakos, W. Trott, T. Hickman, J. Cole, and J. Bucaro, "Microbend fiber-optic sensor as extended hydrophone," *Journal of Quantum Electronics*, vol. 18, no. 10, pp. 1633–1638, 1982.

[13] E. Udd, *Fiber optic sensors*. Wiley Online Library, 1991. Ch.9.

[14] A. Dandridge, "Fiber optic sensors based on the mach-zehnder and michelson interferometers," *Fiber Optic Sensors*, pp. 231–275, 1991.

[15] A. Kersey, M. Marrone, and M. Davis, "Polarisation-insensitive fibre optic michelson interferometer," *Electronics Letters*, vol. 27, no. 6, pp. 518–520, 1991.

[16] M. J. Marrone, A. D. Kersey, and A. D. Dandridge, "Polarization-independent array configurations based on michelson interferometer networks," in *Fibers' 92 (International Society for Optics and Photonics)*, pp. 196–200, 1993.

[17] J. H. Cole, R. L. Johnson, and P. G. Bhuta, "Fiber-optic detection of sound," *The Journal of the Acoustical Society of America*, vol. 62, no. 5, pp. 1136–1138, 1977.

[18] G. Hocker, "Fiber-optic sensing of pressure and temperature," *Applied optics*, vol. 18, no. 9, pp. 1445–1448, 1979.

[19] J. A. Bucaro, H. D. Dardy, and E. F. Carome, "Fiber-optic hydrophone," *The Journal of the Acoustical Society of America*, vol. 62, no. 5, pp. 1302–1304, 1977.

[20] J. Cole, C. Sunderman, A. Tveten, C. Kirkendall, and A. Dandridge, "Preliminary investigation of air-included polymer coatings for enhanced sensitivity of fiber-optic acoustic sensors," in *15th Optical Fiber Sensors Conference OFS2002*, pp. 317–320 vol.1, 2002.

[21] G. A. Cranch, P. J. Nash, and C. K. Kirkendall, "Large-scale remotely interrogated arrays of fiber-optic interferometric sensors for underwater acoustic applications," *Sensors Journal, IEEE*, vol. 3, no. 1, pp. 19–30, 2003.

[22] G. McDearmon, "Theoretical analysis of a push-pull fiber-optic hydrophone," *Journal of Lightwave Technology*, vol. 5, no. 5, pp. 647–652, 1987.

[23] J. A. Bucaro, B. H. Houston, and E. G. Williams, "Fiber-optic air-backed hydrophone transduction mechanisms," *The Journal of the Acoustical Society of America*, vol. 89, no. 1, pp. 451–453, 1991.

[24] N. Zeng, C. Shi, D. Wang, M. Zhang, and Y. Liao, "Diaphragm-type fiber-optic interferometric acoustic sensor," *Optical Engineering*, vol. 42, p. 2558, 2003.

[25] G. H. Ames and J. M. Maguire, "Miniaturized mandrel-based fiber optic hydrophone," *The Journal of the Acoustical Society of America*, vol. 121, no. 3, pp. 1392–1395, 2007.

[26] G. Cranch, G. Miller, and C. Kirkendall, "Fiber laser sensors: Enabling the next generation of miniaturized, wideband marine sensors," in *SPIE Defense, Security, and Sensing*, pp. 80280I–80280I, International Society for Optics and Photonics, 2011.

[27] S. Foster, A. Tikhomirova, M. Milnesa, J. van Velzena, and G. Hardyb, "A fibre laser hydrophone," in *17th International Conference on Optical Fibre Sensors*, vol. 5805, pp. 627–630, SPIE, 2005.

[28] S. Foster, A. Tikhomirov, M. Englund, H. Inglis, G. Edvell, and M. Milnes, "A 16 channel fibre laser sensor array," in *Optical Fibre Technology Australian Optical Society2006. Australian Conference on*, pp. 40–42, IEEE, 2006.

[29] D. Hill, P. Nash, S. Hawker, and I. Bennion, "Progress toward an ultra thin optical hydrophone array," 1998.

[30] K. Hill, Y. Fujii, D. Johnson, and B. Kawasaki, "Photosensitivity in optical fiber waveguides: Application to reflection filter fabrication," *Applied Physics Letters*, vol. 32, p. 647, 1978.

[31] http://en.wikipedia.org/wiki/Fiber_Bragg_grating. Last accessed on 05/04/2012.

[32] R. Kashyap, *Fiber bragg gratings*. Academic Pr, second ed., 1999.

[33] K. O. Hill and G. Meltz, "Fiber bragg grating technology fundamentals and overview," *Journal of Lightwave Technology*, vol. 15, no. 8, pp. 1263–1276, 1997.

[34] P. J. Lemaire, R. Atkins, V. Mizrahi, and W. Reed, "High pressure h 2 loading as a technique for achieving ultrahigh uv photosensitivity and thermal sensitivity in geo 2 doped optical fibres," *Electronics Letters*, vol. 29, no. 13, pp. 1191–1193, 1993.

[35] D. Hill, P. Nash, D. Jackson, D. Webb, S. O'Neill, I. Bennion, and L. Zhang, "Fiber laser hydrophone array," in *Proceedings of SPIE on Fiber Optic Sensor Technology and Applications*, vol. 3860, (Boston, USA), p. 55, 1999.

[36] K. Hill and G. Meltz, "Fiber bragg grating technology fundamentals and overview," *Journal of Lightwave Technology*, vol. 15, no. 8, pp. 1263–1276, 2002.

[37] J. Kringlebotn, J.-L. Archambault, L. Reekie, and D. Payne, "Er 3+ yb 3+ codoped fiber distributed-feedback laser," *Optics Letters*, vol. 19, no. 24, pp. 2101–2103, 1994.

[38] G. Ball, W. Morey, and P. Cheo, "Single- and multipoint fiber-laser sensors," *Photonics Technology Letters, IEEE*, vol. 5, no. 2, pp. 267–270, 1993.

[39] K. P. Koo and A. D. Kersey, "Bragg grating-based laser sensors systems with interferometric interrogation and wavelength division multiplexing," *Journal of Lightwave Technology*, vol. 13, no. 7, pp. 1243–1249, 1995.

[40] A. Cusano, S. D'Addio, A. Cutolo, M. Giordano, S. Campopiano, M. Balbi, and S. Balzarini, "Plastic coated fiber bragg gratings as high sensitivity hydrophones," 2006.

[41] Z. Sun, L. Min, X. Zhang, J. Ni, H. Qi, Y. Wang, C. Wang, J. Chang, and G. Peng, "High performance four-element dfb fiber laser hydrophone array system," in *Proc. SPIE Vol. 8651*, pp. 856107–856107–8, 2012.

[42] I. Bedwell and D. Jones, "Fiber laser sensor hydrophone performance," in *OCEANS 2010 IEEE-Sydney*, pp. 1–5, IEEE, 2010.

[43] L. Hansen and F. Kullander, "Modelling of hydrophone based on a dfb fiber laser," 2004.

[44] P. Bagnoli, N. Beverini, B. Bouhadef, E. Castorina, E. Falchini, R. Falciai, V. Flaminio, E. Maccioni, M. Morganti, F. Sorrentino, F. Stefani, and C. Trono, "Erbium-doped fiber lasers as deep-sea hydrophones," *Nuclear Instruments and Methods in Physics Research Section A: Accelerators, Spectrometers, Detectors and Associated Equipment*, vol. 567, no. 2, pp. 515 – 517, 2006.

[45] X. Zhang, G. Peng, C. Wang, Z. Sun, J. Ni, and Y. Wang, "Distributed feedback fiber laser strain sensor with high sensitivity in a wide frequency range," in *Photonics Asia*, pp. 85611I–85611I, International Society for Optics and Photonics, 2012.

[46] S. Goodman, A. Tikhomirov, and S. Foster, "Pressure compensated distributed feedback fibre laser hydrophone," 2008.

[47] I. K.-H. Leung, *Development of composite cavity fibre lasers for fibre laser hydrophone systems.* PhD thesis, The University of New South Wales, 2008.

[48] Y.-N. Tan, Y. Zhang, and B.-O. Guan, "Hydrostatic pressure insensitive dual polarization fiber grating laser hydrophone," *Sensors Journal, IEEE*, vol. 11, pp. 1169–1172, May 2011.

[49] S. Foster, A. Tikhomirov, and J. van Velzen, "Towards a high performance fiber laser hydrophone," *Journal of Lightwave Technology*, vol. 29, no. 9, pp. 1335–1342, 2011.

[50] R. Ma, W. Zhang, J. He, F. Li, and Y. Liu, "Ultra thin fiber laser vector hydrophone," in *Proc. SPIE-7753*, pp. 775337–775337–4, 2011.

[51] G. A. Cranch, G. A. Miller, and C. K. Kirkendall, "Low frequency acoustic response of a planar fiber laser cantilever in a fluid," in *Proc. of SPIE Vol. 7753* (W. J. Bock, J. Albert, and X. Bao, eds.), (Ottawa, Canada), pp. 775334–4, 2011.

[52] P. Jackson, S. Foster, and S. Goodman, "A fibre laser acoustic vector sensor," in *20th International Conference on Optical Fibre Sensors*, pp. 750329–750329, International Society for Optics and Photonics, 2009.

[53] W. Zhang, R. Ma, and F. Li, "High performance ultrathin fiber laser vector hydrophone," *Journal of Lightwave Technology*, vol. 30, no. 8, pp. 1196–1200, 2012.

[54] F. Zhang, W. Zhang, F. Li, and Y. Liu, "Dfb fiber laser hydrophone with an acoustic low-pass filter," *Photonics Technology Letters, IEEE*, no. 99, pp. 1–1, 2011.

[55] W. Zhang, Y. Liu, F. Li, and H. Xiao, "Fiber laser hydrophone based on double diaphragms: Theory and experiment," *Journal of lightwave technology*, vol. 26, no. 10, pp. 1349–1352, 2008.

[56] W. Zhang, F. Li, and Y. Liu, "Field test of an eight-element fiber laser hydrophone array," in *OFS2012 22nd International Conference on Optical Fiber Sensor*, pp. 8421AX–8421AX, International Society for Optics and Photonics, 2012.

[57] M. R. Layton, "Specification for fiber hydrophone system," tech. rep., DTIC Document, 1988.

[58] A. Bertholds and R. Dandliker, "Determination of the individual strain-optic coefficients in single-mode optical fibres," *Journal of Lightwave Technology*, vol. 6, no. 1, pp. 17–20, 1988.

[59] P. H. Dahl, J. H. Miller, D. H. Cato, and R. K. Andrew, "Underwater ambient noise," *Acoustics Today*, vol. 3, no. 1, pp. 23–33, 2007.

[60] G. A. Cranch, G. Flockhart, and C. K. Kirkendall, "Distributed feedback fiber laser strain sensors," *Sensors Journal, IEEE*, vol. 8, no. 7, pp. 1161–1172, 2008.

[61] Y. Léguillon, K. H. Tow, P. Besnard, A. Mugnier, D. Pureur, and M. Doisy, "First demonstration of a 12 dfb fiber laser array on a 100 ghz itu grid, for underwater acoustic sensing application," in *SPIE Photonics Europe*, pp. 84390J–84390J, International Society for Optics and Photonics, 2012.

[62] A. Dandridge, A. Tveten, and T. Giallorenzi, "Homodyne demodulation scheme for fiber optic sensors using phase generated carrier," *Journal of Quantum Electronics*, vol. 18, no. 10, pp. 1647–1653, 1982.

[63] A. B. Tveten, A. Yurek, M. N. Opsasnick, and A. D. Dandridge, "Demodulator optimization for the interrogation of fiber optic hydrophones in real-world environments," in *10th Optical Fibre Sensors Conference*, pp. 522–525, International Society for Optics and Photonics, 1994.

[64] H. Jun, W. Lin, L. Fang, and L. Yuliang, "An ameliorated phase generated carrier demodulation algorithm with low harmonic distortion and high stability," *Journal of Lightwave Technology*, vol. 28, no. 22, pp. 3258–3265, 2010.

[65] Y. Liu, L. Wang, C. Tian, M. Zhang, and Y. Liao, "Analysis and optimization of the pgc method in all digital demodulation systems," *Journal of lightwave technology*, vol. 26, no. 18, pp. 3225–3233, 2008.

[66] L. Kinsler, A. Frey, A. Coppens, and J. Sanders, *Fundamentals of acoustics*. Wiley-VCH, 1999. pp. 39-48.

[67] J. Snowdon, "Mechanical four-pole parameters and their application," *Journal of Sound and Vibration*, vol. 15, no. 3, pp. 307–323, 1971.

[68] F. Fahy, *Foundations of engineering acoustics*. Academic Press, 2000. pp. 154-155.

[69] F. Tarawneh and S. Muafag, "Friction forces in o-ring sealing," *American Journal of Applied Sciences*, vol. 2, no. 3, pp. 626–632, 2005.

[70] L. Kinsler, A. Frey, A. Coppens, and J. Sanders, *Fundamentals of acoustics*. Wiley-VCH, 1999. pp. 184-187.

[71] W. Young and R. Budynas, *Roark's formulas for stress and strain*, vol. 6. McGraw-Hill New York, 2002.

[72] L. Kinsler, A. Frey, A. Coppens, and J. Sanders, *Fundamentals of acoustics*. Wiley-VCH, 1999. pp. 107-109.

[73] T. G. Giallorenzi, J. A. Bucaro, A. Dandridge Jr, G. Sigel, J. H. Cole, S. C. Rashleigh, and R. G. Priest, "Optical fiber sensor technology," *Microwave Theory and Techniques, IEEE Transactions on*, vol. 30, no. 4, pp. 472–511, 1982.

[74] Y. Tong, H. Zeng, L. Li, and Y. Zhou, "Improved phase generated carrier demodulation algorithm for eliminating light intensity disturbance and phase modulation amplitude variation," *Applied optics*, vol. 51, no. 29, pp. 6962–6967, 2012.

[75] X. Yang, Z. Chena, J. H. Nga, V. Pallayil, and U. Kuttan Chandrika, "A pgc demodulation based on differential-cross-multiplying (dcm) and arctangent (atan) algorithm with low harmonic distortion and high stability," in *Proc. of SPIE Vol*, vol. 8421, pp. 84215J–1, 2012.

[76] I. Bush and A. Cekorich, "Demodulator and method useful for multiplexed optical sensors." US Patent 5903350, published on May 11, 1999. http://www.google.com/patents/US5903350.

[77] D. Chase, "Further modeling of turbulent wall pressure on cylinder and its scaling with diameter," Tech. Rep. Technial Memo 21, DTIC, 1981. http://www.dtic.mil/get-tr-doc/pdf?AD=ADA113820.

[78] O. R. Tutty, "Flow along a long thin cylinder," *Journal of Fluid Mechanics*, vol. 602, no. 1, pp. 1–37, 2008.

[79] A. Carpenter and D. Kewley, "Investigation of low wavenumber turbulent boundary layer pressure fluctuations on long flexible cylinders," in *Eighth Australasian Fluid Mechanics Conference*, vol. 28, p. 9A.1Ð9A.4, 28 November-2 December 1983 1983.

[80] A. Knight, "Flow noise calculations for extended hydrophones in fluid and solid filled towed arrays," *The Journal of the Acoustical Society of America*, vol. 100, p. 245, 1996.

[81] S. H. Francis, M. Slazak, and J. G. Berryman, "Response of elastic cylinders to convective flow noise - i. homogeneous, layered cylinders," *Journal of the Acoustical Society of America*, vol. 75, no. 1, pp. 166–172, 1984.

[82] A. Dowling, "Underwater flow noise," *Theoretical and computational fluid dynamics*, vol. 10, no. 1-4, pp. 135–153, 1998.

[83] G. Corcos, "The resolution of turbulent pressures at the wall of a boundary layer," *Journal of Sound and Vibration*, vol. 6, no. 1, pp. 59–70, 1967.

[84] M. Bull, "Wall-pressure fluctuations beneath turbulent boundary layers: some reflections on forty years of research," *Journal of Sound and Vibration*, vol. 190, no. 3, pp. 299–315, 1996.

[85] S. H. Ko and A. H. Nuttall, "Analytical evaluation of flush-mounted hydrophone array response to the corcos turbulent wall pressure spectrum," *The Journal of the Acoustical Society of America*, vol. 90, p. 579, 1991.

[86] S. H. Ko, "Performance of various shapes of hydrophones in the reduction of turbulent flow noise," *The Journal of the Acoustical Society of America*, vol. 93, p. 1293, 1993.

[87] Y. Hwang and G. Maidanik, "A wavenumber analysis of the coupling of a structural mode and flow turbulence," *Journal of Sound and Vibration*, vol. 142, no. 1, pp. 135–152, 1990.

[88] W. Graham, "A comparison of models for the wavenumber–frequency spectrum of turbulent boundary layer pressures," *Journal of Sound and Vibration*, vol. 206, no. 4, pp. 541–565, 1997.

[89] Y. F. Hwang, W. K. Bonness, and S. A. Hambric, "Comparison of semi-empirical models for turbulent boundary layer wall pressure spectra," *Journal of Sound and Vibration*, vol. 319, no. 1-2, pp. 199–217, 2009.

[90] W. L. Keith and K. M. Cipolla, "Features of the turbulent wall pressure field on a long towed cylinder," *Experiments in Fluids*, vol. 49, no. 1, pp. 203–211, 2010.

[91] M. Goody, "Empirical spectral model of surface pressure fluctuations," *AIAA journal*, vol. 42, no. 9, pp. 1788–1794, 2004.

[92] A. SmolÕyakov, "Calculation of the spectra of pseudosound wall-pressure fluctuations in turbulent boundary layers," *Acoustical Physics*, vol. 46, no. 3, pp. 342–347, 2000.

[93] D. Chase, "The character of the turbulent wall pressure spectrum at subconvective wavenumbers and a suggested comprehensive model," *Journal of Sound and Vibration*, vol. 112, no. 1, pp. 125–147, 1987.

[94] D. Chase, "Modeling the wavevector-frequency spectrum of turbulent boundary layer wall pressure," *Journal of Sound and Vibration*, vol. 21, no. 1, pp. 29–67, 1980.

[95] S. R. Snarski and R. M. Lueptow, "Wall pressure and coherent structures in a turbulent boundary layer on a cylinder in axial flow," *Journal of Fluid Mechanics*, vol. 286, pp. 137–171, 1995.

[96] A. Foley, W. Keith, and K. Cipolla, "Comparison of theoretical and experimental wall pressure wavenumber–frequency spectra for axisymmetric and flat-plate turbulent boundary layers," *Ocean Engineering*, vol. 38, no. 10, pp. 1123–1129, 2011.

[97] E. A. Skelton and J. H. James, *Theoretical acoustics of underwater structures*. Imperial College Press London, 1997.

[98] K. Cipolla and W. Keith, "Measurements of the wall pressure spectra on a full-scale experimental towed array," *Ocean Engineering*, vol. 35, no. 10, pp. 1052–1059, 2008.

[99] U. Kuttan Chandrika, V. Pallayil, M. Chitre, and S. Kuselan, "Estimated flow noise levels due to a thin line digital towed array," in *OCEANS, 2011 IEEE-Spain*, pp. 1–4, IEEE, 2011.

[100] V. Pallayil, S. Muttuthupara, M. Chitre, and K. Govind, "Characterization of a digital thin line towed array experimental assessment of vibration levels and tow shape," in *Underwater acoustic measurements*, pp. 21–26, 2009.

[101] K. M. Cipolla and W. L. Keith, "Momentum thickness measurements for thick axisymmetric turbulent boundary layers," *Journal of fluids engineering*, vol. 125, no. 3, pp. 569–575, 2003.

[102] M. S. Howe, *Acoustics of fluid-structure interactions*. Cambridge University Press, 1998.

[103] S. Foster, "Dynamical noise in single-mode distributed feedback fiber lasers," *Journal of Quantum Electronics*, vol. 40, no. 9, pp. 1283–1293, 2004.

[104] A. D. Kersey, "A review of recent developments in fiber optic sensor technology," *Optical Fiber Technology*, vol. 2, no. 3, pp. 291 – 317, 1996.

[105] R. Kashyap, *Fiber bragg gratings*. Academic Pr, second ed., 1999.

[106] Y.-J. Rao, "In-fibre bragg grating sensors," *Measurement science and technology*, vol. 8, no. 4, p. 355, 1997.

[107] W. Morey, G. Meltz, and W. Glenn, "Fiber optic bragg grating sensors," in *OE/FIBERS'89*, vol. 1169, pp. 98–107, 1989.

[108] F.-X. Launay, R. Lardat, R. Bouffaron, G. Roux, M. Doisy, and C. Bergogne, "Static pressure and temperature compensated wideband fiber laser hydrophone," in *Fifth European Workshop on Optical Fibre Sensors*, pp. 87940K–87940K, International Society for Optics and Photonics, 2013.

Appendices

Structural acoustics of a fluid loaded infinite cylindrical shell [97]

The array tube can be modeled as a cylindrical shell. The equations of motions for an isotropic cylinderical shell can be expressed as given in equation (1). Equation (1) is based on the Goldenveizer & Novozhilov (Arnold & Warburton) shell formulations under the assumption that rotary inertia and transverse shear effects are negligible. These equations can provide sufficient accuracies required for acoustic calculations.

$$\begin{pmatrix} \mathbb{L}_{11} & \mathbb{L}_{12} & \mathbb{L}_{13} \\ \mathbb{L}_{21} & \mathbb{L}_{22} & \mathbb{L}_{23} \\ \mathbb{L}_{31} & \mathbb{L}_{32} & \mathbb{L}_{33} \end{pmatrix} \begin{pmatrix} u_z(\phi, z) \\ u_\phi(\phi, z) \\ u_r(\phi, z) \end{pmatrix} = \begin{pmatrix} F_z(\phi, z) \\ F_\phi(\phi, z) \\ F_r(\phi, z) \end{pmatrix} \tag{1a}$$

where

$$\tag{1b}$$

$$\mathbb{L}_{11} = -E_1 \left(\frac{\partial^2}{\partial z^2} + \frac{1-\nu}{2a^2} \frac{\partial^2}{\partial \phi^2} \right) + \rho_s h \frac{\partial^2}{\partial t^2}, \tag{1c}$$

$$\mathbb{L}_{12} = -E_1 \frac{1+\nu}{2a} \frac{\partial^2}{\partial z \partial \phi}, \tag{1d}$$

$$\mathbb{L}_{13} = -E_1 \frac{\nu}{a} \frac{\partial}{\partial z}, \tag{1e}$$

$$\mathbb{L}_{21} = \mathbb{L}_{12}, \tag{1f}$$

$$\mathbb{L}_{22} = -E_1 \left(\frac{1-\nu}{2} \frac{\partial^2}{\partial z^2} + \frac{1}{a^2} \frac{\partial^2}{\partial \phi^2} + 2\beta^2 (1-\nu) \frac{\partial^2}{\partial z^2} + \frac{\beta^2}{a^2} \frac{\partial^2}{\partial \phi^2} \right) + \rho_s h \frac{\partial^2}{\partial t^2}, \tag{1g}$$

$$\mathbb{L}_{23} = -E_1 \left(\frac{1}{a^2} \frac{\partial}{\partial \phi} - \beta^2 (2-\nu) \frac{\partial^3}{\partial \phi \partial z^2} - \frac{\beta^2}{a^2} \frac{\partial^3}{\partial \phi^3} \right), \tag{1h}$$

$$\mathbb{L}_{31} = -\mathbb{L}_{13}, \tag{1i}$$

$$\mathbb{L}_{32} = -\mathbb{L}_{23}, \tag{1j}$$

$$\mathbb{L}_{33} = E_1 \left(\frac{1}{a^2} + \beta^2 a^2 \frac{\partial^4}{\partial z^4} + \frac{\beta^2}{a^2} \frac{\partial^4}{\partial \phi^4} + 2\beta^2 \frac{\partial^4}{\partial z^2 \partial \phi^2} \right) + \rho_s h \frac{\partial^2}{\partial t^2}, \tag{1k}$$

$$\beta^2 = \frac{h^2}{12a^2}, \tag{1l}$$

$$E_1 = \frac{Eh}{1-\nu^2}, \tag{1m}$$

where u represents the displacements and F represent the forces acting in the direction indicated by the subscripts in a cylindrical coordinate system, E is the Young's modulus of the cylinder and ν is the Poisson's ratio and ρ_s is the cylinder density. The equation of motion given in Eq. (1) can be simplified by using a Fourier transform and writing equations in spectral field quantities using relation given in Eq. (2).

$$\mathbb{F}(r, n, k_z) = \frac{1}{2\pi} \int_0^{2\pi} exp(-in\phi) \int_{-\infty}^{\infty} F(r, \phi, z) exp(-ik_z z) dz d\phi \tag{2}$$

Thus for time-harmonic motions, the equation Eq. (1) can be written as

$$\begin{pmatrix} \mathbf{S}_{11}(n,k_z) & \mathbf{S}_{12}(n,k_z) & \mathbf{S}_{13}(n,k_z) \\ \mathbf{S}_{21}(n,k_z) & \mathbf{S}_{22}(n,k_z) & \mathbf{S}_{23}(n,k_z) \\ \mathbf{S}_{31}(n,k_z) & \mathbf{S}_{32}(n,k_z) & \mathbf{S}_{33}(n,k_z) \end{pmatrix} \begin{pmatrix} \mathbb{u}_z(n,k_z) \\ \mathbb{u}_\phi(n,k_z) \\ \mathbb{u}_r(n,k_z) \end{pmatrix} = \begin{pmatrix} \mathbb{F}_z(n,k_z) \\ \mathbb{F}_\phi(n,k_z) \\ \mathbb{F}_r(n,k_z) \end{pmatrix} \tag{3a}$$

where

$$\tag{3b}$$

$$\mathbf{S}_{11}(n,k_z) = -E_1\left(k_z^2 + n^2\frac{1-\nu}{2a^2}\right) - \omega^2\rho_s h, \tag{3c}$$

$$\mathbf{S}_{12}(n,k_z) = \frac{-E_1(1+\nu)nk_z}{2a}, \tag{3d}$$

$$\mathbf{S}_{13}(n,k_z) = \frac{-E_1\nu i k_z}{a}, \tag{3e}$$

$$\mathbf{S}_{21}(n,k_z) = \mathbf{S}_{12}(n,k_z), \tag{3f}$$

$$\mathbf{S}_{22}(n,k_z) = E_1\left(\frac{(1-\nu)k_z^2}{2} + \frac{n^2}{a^2} + 2k_z^2\beta^2(1-\nu) + \frac{\beta^2 n^2}{a^2}\right) - \omega^2\rho_s h, \tag{3g}$$

$$\mathbf{S}_{23}(n,k_z) = -E_1\left(\frac{in}{a^2} + i\beta^2(2-\nu)k_z^2 n + \frac{i\beta^2 n^3}{a^2}\right) \tag{3h}$$

$$\mathbf{S}_{31}(n,k_z) = -\mathbf{S}_{13}(n,k_z), \tag{3i}$$

$$\mathbf{S}_{32}(n,k_z) = -\mathbf{S}_{23}(n,k_z), \tag{3j}$$

$$\mathbf{S}_{33}(n,k_z) = E_1\left(\frac{1}{a^2} + \beta^2 a^2 k_z^4 + \frac{\beta^2 n^4}{a^2} + 2\beta^2 k_z^2 n^2\right) - \omega^2\rho_s h, \tag{3k}$$

where $\mathbb{u}_z(n,k_z)$, $\mathbb{u}_r(n,k_z)$ and $\mathbb{u}_\phi(n,k_z)$ are the spectral displacements and $\mathbb{F}_z(n,k_z)$, $\mathbb{F}_\phi(n,k_z)$, and $\mathbb{F}_r(n,k_z)$ are the spectral excitations. For the problem at hand, it can be assumed that the external excitation is primarily radial in nature and arise from the normal pressure acting at internal and external surfaces of the cylinder. Thus the excitation in the

radial direction can be written as

$$\mathbb{F}_r(n, k_z) = P(n, k_z) - p_i(a, n, k_z) + p_e(a, n, k_z) \tag{4}$$

where $p_i,\ p_e$ are the internal pressure and external pressures acting on the shell surface. The pressure field inside the cylinder denoted by p_i should be finite at the centre of the cylinder. Hence the solution for internal pressure can have on Bessel functions of first kind. Thus, the solution of reduced wave equation in cylindrical co-ordinates yield

$$p_i(r, n, k_z) = A_n(k_z) J_{|n|}(\gamma_1 r), \tag{5a}$$

where

$$\gamma_1 = \sqrt{{k_1}^2 - k_z^2}, \tag{5b}$$

$$k_1 = \omega / c_i \tag{5c}$$

where c_i is the velocity of sound in the internal fluid. Furthermore, the pressure field should satisfy the boundary condition

$$\frac{\partial p_i(r, n, k_z)}{\partial r} = \rho_i \omega^2 \mathfrak{u}_r(n, k_z) \tag{6}$$

where ρ_i is the density of the internal fluid. Thus from equations (6) and (5) the interior pressure can be written as

$$p_i(r, n, k_z) = \rho_i \omega^2 \mathfrak{u}_r(n, k_z) \frac{J_{|n|}(\gamma_1 r)}{\gamma_1 {J_{|n|}}'(\gamma_1 a)} \tag{7}$$

The pressure field in the exterior fluid domain should satisfy radiation condition at infinity. Thus

$$p_e(r, n, k_z) = B_n(k_z) H_{|n|}(\gamma_2, r), \tag{8}$$

where $\gamma_2 = \sqrt{({k_2}^2 - k_z^2}$, $k_2 = \omega/c_e$ and c_e is the sound velocity in exterior fluid. Applying a boundary condition similar to one in Eq. (6), external pressure can be written as

$$p_e(r, n, k_z) = \rho_e \omega^2 \mathbb{u}_r(n, k_z) \frac{H_{|n|}(\gamma_2 r)}{\gamma_2 {H_{|n|}}'(\gamma_2 a)}. \tag{9}$$

Thus the equation (3) modified to include the effect of fluid loading can be expressed as

$$\left[\mathbf{S}\right] \left[\mathbb{u}\right] = \left[\mathbb{F}\right] \tag{10a}$$

where

$$\left[\mathbf{S}\right] = \begin{pmatrix} \mathbf{S}_{11}(n, k_z) & \mathbf{S}_{12}(n, k_z) & \mathbf{S}_{13}(n, k_z) \\ \mathbf{S}_{21}(n, k_z) & \mathbf{S}_{22}(n, k_z) & \mathbf{S}_{23}(n, k_z) \\ \mathbf{S}_{31}(n, k_z) & \mathbf{S}_{32}(n, k_z) & \mathbf{S}_{33}(n, k_z) + f_l \end{pmatrix}, \tag{10b}$$

$$\left[\mathbb{u}\right] = \begin{pmatrix} \mathbb{u}_z(n, k_z) \\ \mathbb{u}_\phi(n, k_z) \\ \mathbb{u}_r(n, k_z) \end{pmatrix}, \quad \left[\mathbb{F}\right] = \begin{pmatrix} 0 \\ 0 \\ P(n, k_z) \end{pmatrix}, \tag{10c}$$

$$f_l = \rho_e \omega^2 u_r(n, k_z) \frac{H_{|n|}(\gamma_2 r)}{\gamma_2 {H_{|n|}}'(\gamma_2 a)} - \rho_i \omega^2 u_r(n, k_z) \frac{J_{|n|}(\gamma_1 r)}{\gamma_1 {J_{|n|}}'(\gamma_1 a)}. \tag{10d}$$

List of my publications

[1] U. Kuttan Chandrika, V. Pallayil, C. Zhihao, and N. J. Hong, "Development of a high sensitivity dfb fibre laser hydrophone," in *International Symposium on Ocean Electronics (SYMPOL2011)*, pp. 103–108, IEEE, 2011.

[2] X. Yang, Z. Chena, J. H. Ng, V. Pallayil, and U. Kuttan Chandrika, "A pgc demodulation based on differential-cross-multiplying (dcm) and arctangent (atan) algorithm with low harmonic distortion and high stability," in *Proc. of SPIE*, vol. 8421, pp. 84215J–1, 2012.

[3] U. Kuttan Chandrika, V. Pallayil, K. M. Lim, and C. H. Chew, "Design considerations for a DFB fibre laser based high sensitivity broadband hydrophone," in *11th European Conference on Underwater Acoustics 2012*, pp. 591–596, 2012.

[4] U. Kuttan Chandrika and V. Pallayil, "Signal distortion due to low-pass filtering in phase generated carrier demodulation schemes for interferometric sensors," in *International Symposium on Ocean Electronics (SYMPOL2013)*, pp. 141–145, IEEE, 2013.

[5] U. Kuttan Chandrika, V. Pallayil, K. M. Lim, and C. H. Chew, "Pressure compensated fiber laser hydrophone: Modeling and experimentation," *The Journal of the Acoustical Society of America*, vol. 134, pp. 2710–2718, 2013.

[6] U. Kuttan Chandrika, V. Pallayil, K. M. Lim, and C. H. Chew, "Flow noise response of a diaphragm based fibre laser hydrophone array," *Ocean Engineering Journal.* (Under review).

Engineering drawings

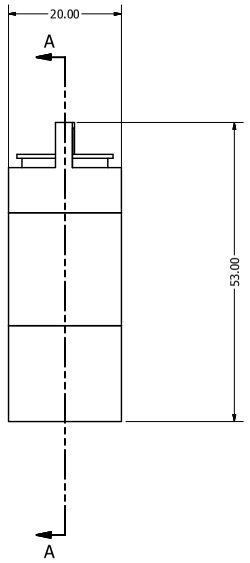

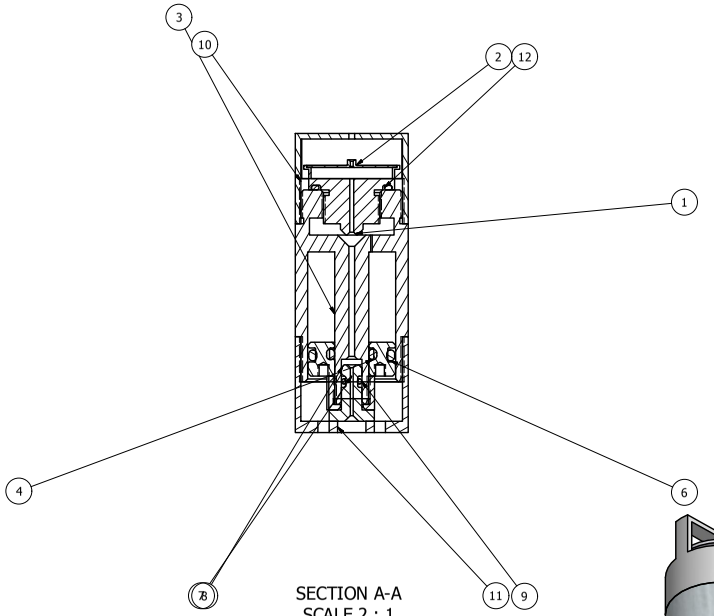

SECTION A-A
SCALE 2 : 1

PARTS LIST			
ITEM	QTY	PART NUMBER	DESCRIPTION
1	1	FOH_D_P_4011	
2	1	FOH_D_P_4021	
3	1	FOH_D_P_4031	
4	1	Oring-AS-568-01011	
6	1	Oring-AS-568-01311	
7	1	FOH_D_P_40811	
8	1	FOH_D_P_40711	
9	1	Oring-2X11	
10	1	FOH_D_P_40911	
11	1	FOH_D_P_41011	
12	1	Oring12x1	
18	1	FOH_D_P_40512	

Notes:

1. Material :
2. All dimensions are in mm
3. Pls remove sharp edges and burrs

General Tolerance

Size	1-6	>6-30	>30-120
Tolerance	±0.1	±0.2	±0.3

DRAWN KCU	6/26/2012	Acoustic Research Laboratory
CHECKED		TITLE: FOH Assembly
QA		
MFG		
APPROVED		SIZE C | DWG NO FOH-A-402 | REV
		SCALE | SHEET 1 OF 1

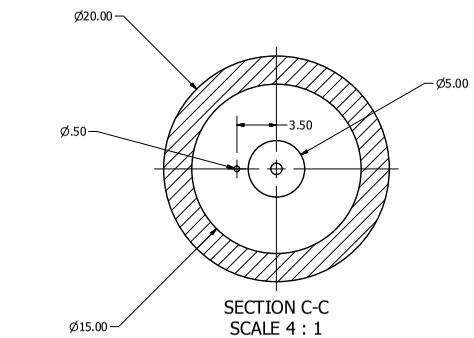

SECTION C-C
SCALE 4 : 1

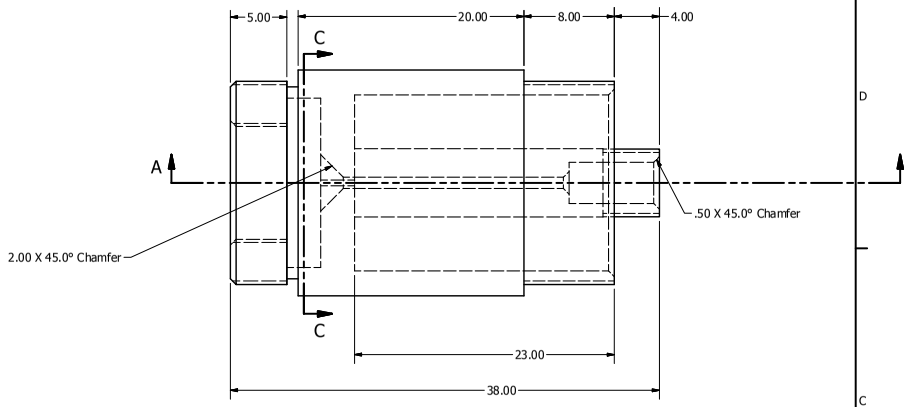

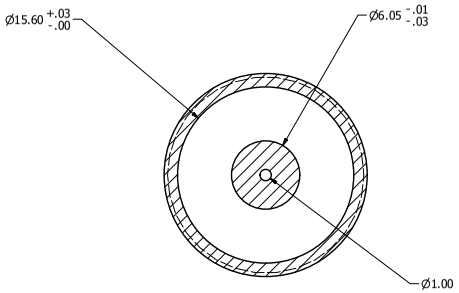

SECTION E-E
SCALE 4 : 1

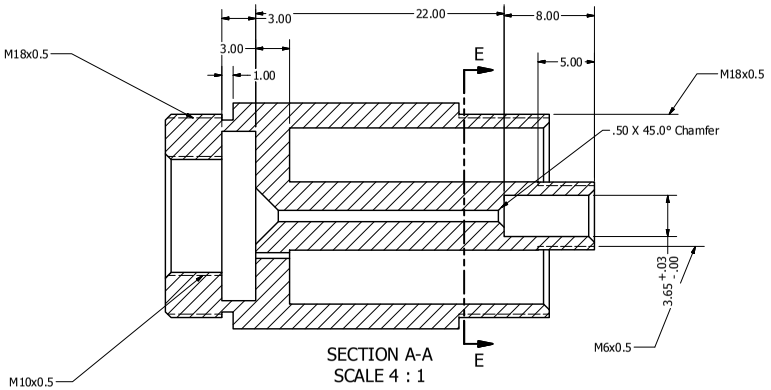

SECTION A-A
SCALE 4 : 1

Notes:

1. Material : Aluminum Black Anodised
2. All dimensions are in mm
3. Pls remove sharp edges and burrs

General Tolerance

Size	1-6	>6-30	>30-120
Tolerance	±0.1	±0.2	±0.3

DRAWN KCU	6/26/2012	Acoustic Research Laboratory
CHECKED		TITLE: Shell
QA		
MFG		
APPROVED		SIZE C | DWG NO FOH_D_P_4031 | REV
		SCALE | SHEET 1 OF 1

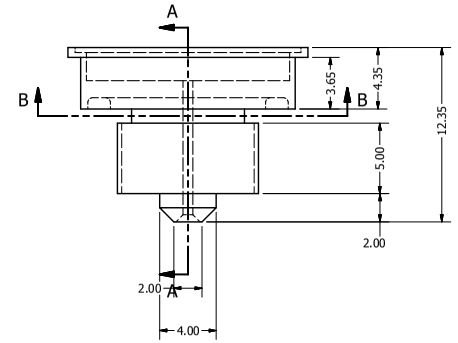

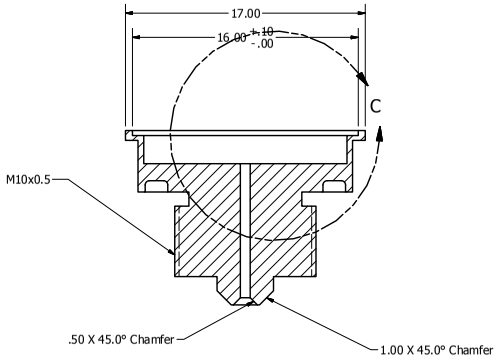

SECTION A-A
SCALE 5 : 1

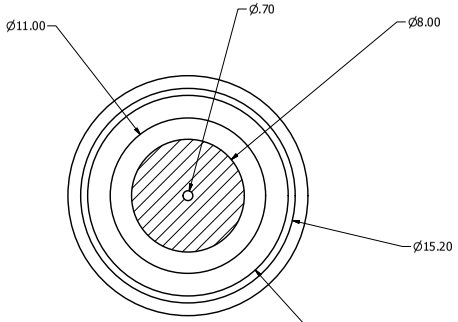

SECTION B-B
SCALE 5 : 1

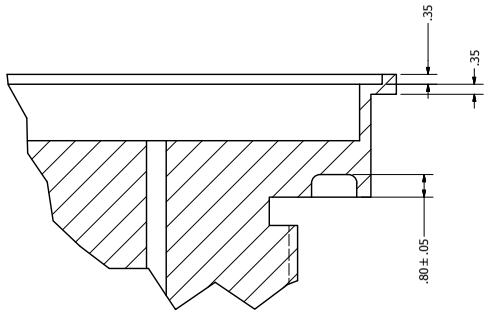

DETAIL C
SCALE 10 : 1

Notes:

1. Material : Aluminum Black anodised
2. All dimensions are in mm
3. Pls remove sharp edges and burrs

General Tolerance

Size	1-6	>6-30	>30-120
Tolerance	±0.1	±0.2	±0.3

DRAWN KCU	6/26/2012	Acoustic Research Laboratory	
CHECKED		TITLE Cup	
QA			
MFG			
APPROVED		SIZE C	DWG NO FOH_D_P_4011 REV
		SCALE	SHEET 1 OF 1

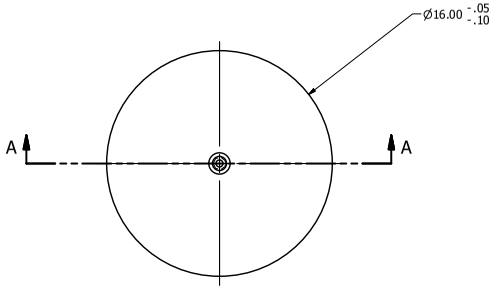

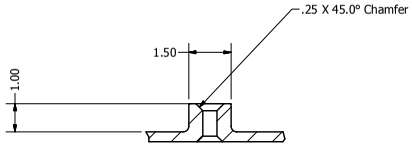

DETAIL B
SCALE 10 : 1

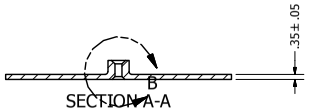

SECTION A-A
SCALE 5 : 1

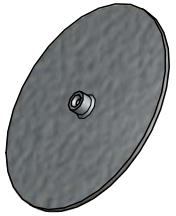

Notes:

1. Material: Aluminum Black Anodised
2. All dimensions are in mm
3. Pls remove sharp edges and burrs

General Tolerance

Size	1-6	>6-30	>30-120
Tolerance	±0.1	±0.2	±0.3

DRAWN KCU	6/27/2012	Acoustic Research Laboratory
CHECKED		TITLE: Diaphragm
QA		
MFG		
APPROVED		SIZE: C; DWG NO: FOH_D_P_4021; REV
		SCALE; SHEET 1 OF 1

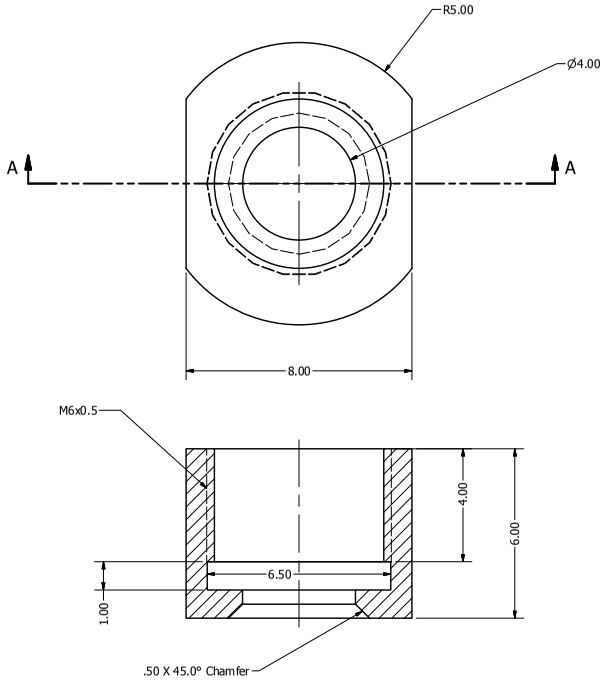

SECTION A-A
SCALE 10 : 1

Notes:

1. Material : Aluminum Black Anodised
2. All dimensions are in mm
3. Pls remove sharp edges and burrs

General Tolerance

Size	1-6	>6-30	>30-120
Tolerance	±0.1	±0.2	±0.3

DRAWN KCU	6/26/2012	Acoustic Research Laboratory
CHECKED		TITLE: Nut
QA		
MFG		
APPROVED		SIZE C | DWG NO FOH_D_P_40811 | REV
		SCALE | SHEET 1 OF 1

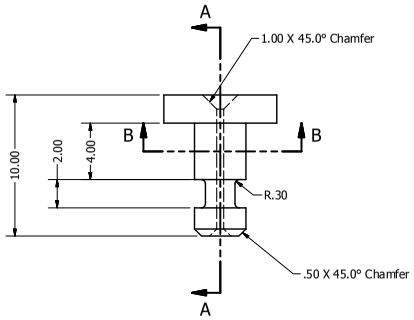

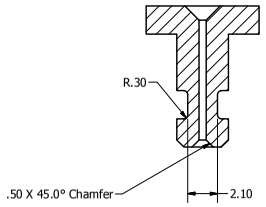

SECTION A-A
SCALE 5 : 1

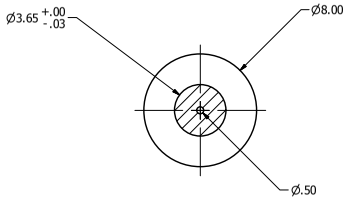

SECTION B-B
SCALE 5 : 1

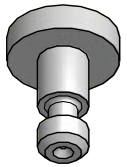

Notes:

1. Material : Aluminum , Black Anodised
2. All dimensions are in mm
3. Pls remove sharp edges and burrs

General Tolerance

Size	1-6	>6-30	>30-120
Tolerance	±0.1	±0.2	±0.3

DRAWN KCU	6/26/2012	Acoustic Research Laboratory
CHECKED		TITLE: Sleeve
QA		
MFG		
APPROVED		SIZE C | DWG NO FOH_D_P_40711 | REV
		SCALE | SHEET 1 OF 1

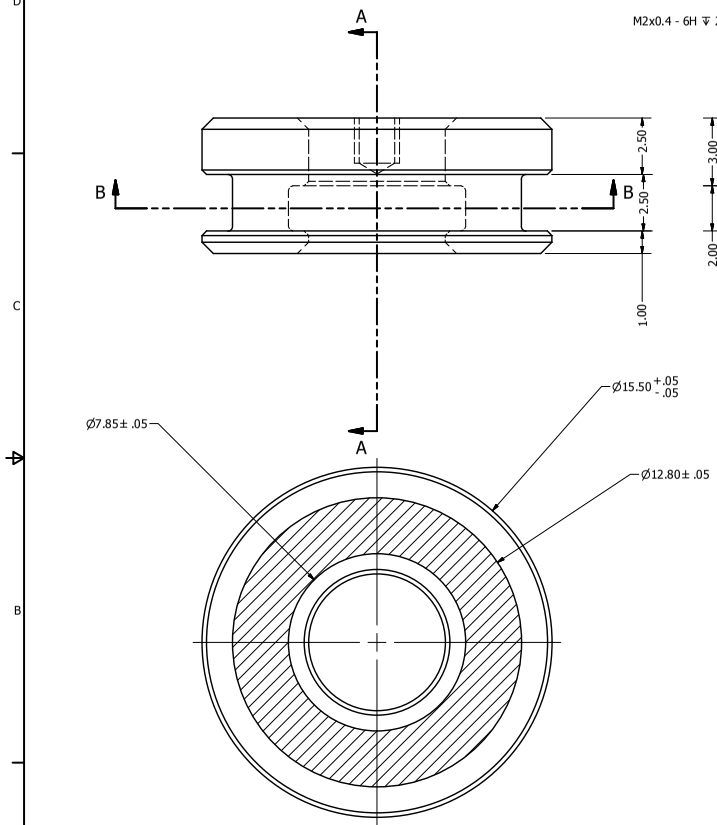

SECTION B-B
SCALE 8:1

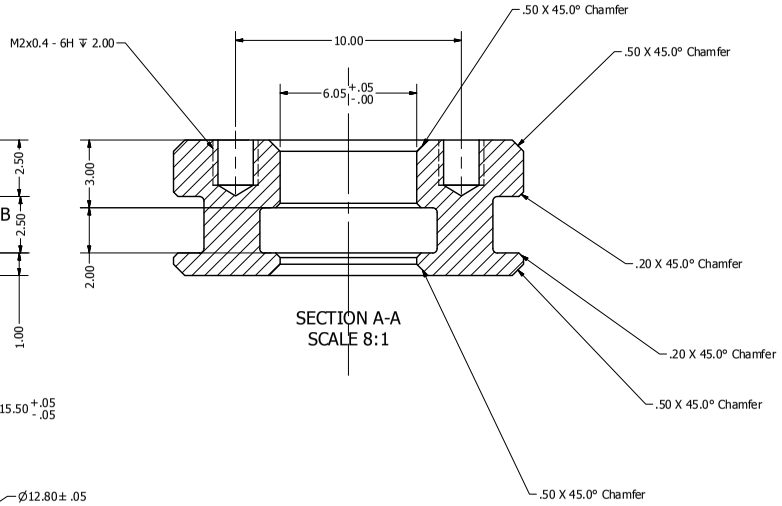

SECTION A-A
SCALE 8:1

Notes:

1. Material : Aluminum
2. All dimensions are in mm
3. Pls remove sharp edges and burrs

General Tolerance

Size	1-6	>6-30	>30-120
Tolerance	±0.1	±0.2	±0.3

DRAWN KCU	7/30/2012	Acoustic Research Laboratory
CHECKED		TITLE: Piston
QA		
MFG		
APPROVED		SIZE C | DWG NO FOH_D_P_40512 | REV
		SCALE | SHEET 1 OF 1

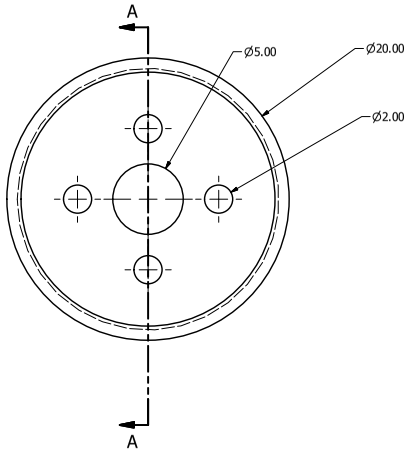

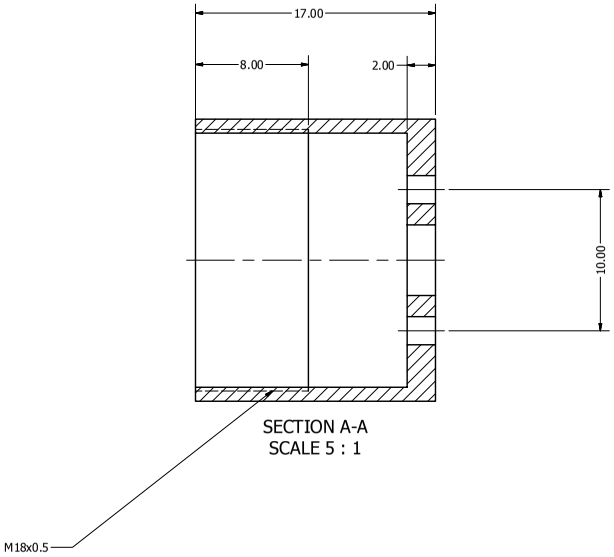

SECTION A-A
SCALE 5 : 1

Notes:

1. Material : Aluminum Black Anodised
2. All dimensions are in mm
3. Pls remove sharp edges and burrs

General Tolerance

Size	1-6	>6-30	>30-120
Tolerance	±0.1	±0.2	±0.3

DRAWN KCU	6/26/2012	Acoustic Research Laboratory
CHECKED		TITLE: Cap
QA		
MFG		
APPROVED		SIZE: C; DWG NO: FOH_D_P_41011; REV
		SCALE; SHEET 1 OF 1

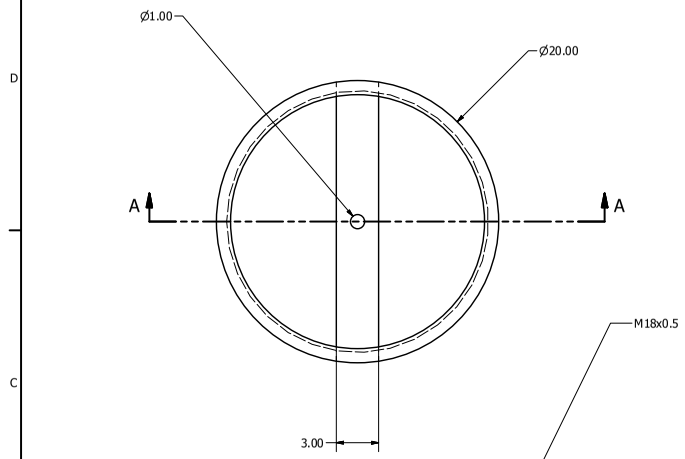

SECTION A-A
SCALE 5 : 1

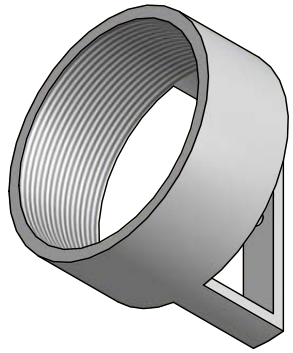

Notes:

1. Material : Aluminum Black anodised
2. All dimensions are in mm
3. Pls remove sharp edges and burrs

General Tolerance

Size	1-6	>6-30	>30-120
Tolerance	±0.1	±0.2	±0.3

DRAWN KCU	6/26/2012	Acoustic Research Laboratory
CHECKED		TITLE: Diaphragm Cap
QA		
MFG		
APPROVED		SIZE C | DWG NO FOH_D_P_40911 | REV
		SCALE | SHEET 1 OF 1